THE ASSEMBLY OF *p*-ARYL TRIAZOLE FOLDAMERS INTO DOUBLE AND OTHER SUPER-HELICAL STRUCTURES

J. M. OKERIO

2017

THE ASSEMBLY OF *p*-ARYL TRIAZOLE FOLDAMERS INTO DOUBLE AND OTHER SUPER-HELICAL STRUCTURES

By

J. M. Okerio

A dissertation submitted in fulfillment of the requirements for the PhD degree in chemistry to be awarded at the Nelson Mandela Metropolitan University

June 2017

Supervisor: Dr. N. Mama
Co-Supervisor: Prof. Bert Klumperman

DECLARATION

I, Jaspher Mosomi Okerio, Student No. s211278769, hereby declare that this dissertation for a PhD degree in Chemistry is my own work and that it has not previously been submitted for assessment or completion of any postgraduate qualification to another university or for any other qualification.

DEDICATION

Unto God, in whom all is possible

ABSTRACT

The assembly of poly(*para*-aryltriazoles) (pPATs), synthesized via Cu(I)-catalysed azide-alkyne cycloaddition, into highly ordered structures is investigated. Firstly, the assembly of the pPATs into double helical structures, as a function of solvent quality and side chain chirality, was studied. The solvents employed (DMF and water) induced changes in van der Waals forces and surface free energy thus influencing the order of the pPATs' random coils into double helical structures. The observed double helical structures, assembly that was analyzed using ultraviolet-visible (UV-Vis) specroscopy, circular dichroism (CD) spectroscopy, scanning transmission electron microscopy (STEM) and confocal fluorescence imaging microscopy upon addition of 0 – 80% water into the pPATs' random coils, exhibit stable morphologies stabilized by π-π stacking and hydrogen bonding at 80% water content. The pPATs exist as random coils at 10% water in DMF. At 40% water in DMF, the pPATs' strands were observed to exist in a side-by-side orientation. The adjacent strands, side by side, intertwine into double helices and eventually stack as the amount of water is increased to 80%. The obtained results present a facile strategy for the fabrication of polymeric double helical structures with stable morphologies. The average diameter of the resulting one-handed and opposite handed double helical structures is about 200 nm, a pitch of 170 nm and an overall length of several micrometres.

The assembly of the pPATs into ordered structures in the presence of a neutral organic template and anions was also assessed. Hydrophobic poly(γ-benzyl-L-glutamate) (PBLG) template was introduced at various concentrations and transition region of the pPATs (10% water in DMF). At this stage the PBLG template is CD inactive. The template modified the assembly mechanism to afford structures, which cannot be achieved in its absence. It disallows the organization of the pPATs into double helical structures. The pPATs strands thread around the template and stack into long tubules of up to 10 microns and irregular diameter. The irregular diameter is attributed to uneven threading of pPATs strands around the template at some sections.

The sensitivity and binding ability of the pPAT system to halide ions such as F^-, Cl^- and Br^-, which involves re-organization of the aryl-triazole bonds, is explored using NMR and UV-Vis and CD spectroscopies. Br^- which induces the highest shift of the triazole C-H proton signal in the NMR analysis also shows the highest dynamic quenching of the pPATs' UV-Vis and CD spectra. The UV-Vis

and CD signals are linearly dependent on the concentration of the anions. This confirms non-aggregation assembly in the presence of anions. Conclusively, the pPATs interact with the bromide anion in aqueous solution, which consequently prevents the aggregation of the foldamers.

Finally, using PATs with different amounts of chiral side chains, co-operativity among side chains that leads to transfer, propagation and amplification of chirality is confirmed. A non-linear dependence of the CD signal on the amount of chiral side chains was observed. Chiral amplification was observed as low as 1% of the chiral side chains. However, approximately 20% of the chiral side chains are needed to obtain half the intensity of the cotton effect exhibited by the homochiral pPAT.

ACKNOWLEDGEMENTS

I would like to acknowledge the following people and institutions that made it possible for me to complete this work;

- The almighty God for the gift of life.
- My promoter, Dr. N. Mama for her constant guidance, support and encouragement since I joined NMMU in 2011.
- My co-promoter, Prof. Bert Klumperman from the Department of Chemistry and Polymer Science at Stellenbosch University for his input, valued advice and support.
- Dr. R. Pfukwa from the Department of Chemistry and Polymer Science at Stellenbosch University for his valued assistance in designing and reviewing this work.
- Nelson Mandela Metropolitan University (NMMU)'s Research Office and the Department of Chemistry for funding and giving the opportunity and facilities to carry out this project.
- Prof. Cedric McClelland and Dr. Benita Barton for editing and reviewing this work
- Mr. H. Marchant, Ms Kina muller, Mr. H. Schalekamp, Dr. E. Hosten and Mr. E. Bashman for their technical assistance.
- Dr. Edwin Simiyu and Dr. Sam Bosire for their treasured friendship and advice.
- Fellow students and friends at Nelson Mandela Metropolitan University and Stellenbosch University for their encouragement.
- My mother, siblings, in-laws and wife Teresa Bosibori for their endless love and motivation to strive for my dream

CONTENTS

LIST OF FIGURES

LIST OF SCHEMES

SELECTED ABBREVIATIONS

CD	circular dichroism
CuAAC	copper(I) catalyzed azide alkyne cycloaddition
CuBr	copper(I) bromide
$CuSO_4$	copper(II)sulphate
Da	Dalton
DCC	*N,N'*-dicyclohexylcardodiimide
DHP	dihydropyran
DMF	dimethylformamide
DMAc	dimetyacetamide
DMAP	dimethylamino pyridine
DMSO	dimethylsulfoxide
EDTA	ethylenediaminetetraacetic acid
FT-IR	Fourier-transform infra-red
NaH	sodium hydride
NaN_3	sodium azide
$NaNO_2$	sodium nitrite
NMR	nuclear magnetic resonance
MeOH	methanol
PBLG	poly(γ-benzyl-L-glutamate)

p-TSA	*para*-toluene sulfonic acid
pPATs	poly(*para*-aryltriazoles)
PMDETA	*N,N,N',N'',N''*-pentamethyldiethylenetriamine
SEC	size exclusion chromatography
$SnCl_2$	tin (II) chloride
TEA	triethylamine
TBAF	tetrabutylammonium fluoride
TMSA	trimethylsilyl acetylene
THP	tetrahydropyran
$TMSN_3$	trimethylsilyl azide
$TBNO_2$	*tert*-butyl nitrite
TEM	transmission electron microscopy
THF	tetrahydrofuran
TLC	thin layer chromatography
UV-Vis	ultraviolet visible

CHAPTER 1: INTRODUCTION

1.1 Background of this study

Macromolecules that assemble into helical architectures are important structural motifs in nature [1, 2]. For example, DNA that assumes a helical conformation in which two or more linear structural units are bound together into a twisting morphology, efficiently preserves, replicates, and translates genetic information [1 – 3]. To craft the bio-helical architectures with exquisite precision, and functions, nature depends on a balanced interplay between the principles of intermolecular interactions. Such interactions include molecular recognition, co-operativity, preorganization, and precise control of non-covalent interactions to afford conformations, stabilities, sizes, lengths and shapes befitting their functions [4 – 7].

Inspired by the structural and functional elegance of bio-assemblies, helical structures and superstructures have received increasing attention in biomimetic and synthetic supramolecular systems [1-3, 12]. Numerous artificial helices, that have not only rivalled bio-helices in their function and application but also expanded the structural motifs and applications into areas not realized by nature, have been designed [8 – 11]. Many of these reported helical polymers and oligomers, however, fold into single helices and only a few systems exist for the double helical motifs and superstructures [1 – 3]. In particular, the chemistry of synthetic polymeric double helices is still in its infancy [2] due to challenges in designing, reliable determination of double helical structures and elucidation of the intermediate steps, pathways and processes involved during their assembly.

In this regard, the design of double helix assembly systems which can be visualized at the nanoscale is one of the approaches to these challenges that will enable exploration of processes and pathways involved during double helix assembly and therefore expand on and contribute to the synthesis of double helices and super structures with special qualities and specific applications. The visualization, achievable through labelling of the helices with florescent dyes, provides for the tracking and monitoring of the double helix assembly processes *via* fluorescence signals. This technique has been successfully utilized in studying and monitoring the aggregation interactions of

proteins. The proteins are initially labelled and/or tagged with dyes and their interactions and associations monitored by tracking the spatial distribution of the fluorescent signals [13-14].

Further, control over the factors that guide nature's assembly mechanisms in artificial systems is an appealing research area in chemistry and material science that promises to afford tailored hierarchical structures [17, 18]. Such factors, whose effect on assembly will be investigated in this work, include the use of templates, anions and chirality. Templates control size, length and stability of assemblies [19]. For example, in the assembly of the coat protein of tobacco mosaic virus (TMV) into a helical column, the viral RNA, which acts as a template around which the protein is wound, provides additional stability and controls the length of the helical columnar aggregates that otherwise would not be achieved in the non-templated assembly [19]. With regards to chirality, transfer and amplification of chirality from small chiral segments within an assembly system is achieved via co-operative interactions termed as 'sergeants and soldiers' and/or 'majority rule'. These interactions ought to be helpful in the designing of enantioselective new materials for chiral recognition, sensing, separation and asymmetric catalysis [20, 21].

1.2 Aim of the study

Double helical structures assembly forms the basis of this work. The assembly was based on labeled and chiral poly(*para*-aryltriazoles) (pPATs). The pPATs' random coils assemble into strands, ordered side by side, that intertwine to form double helices which eventually stack into long double helical columns of indeterminate length (**Figure 1**) as a result to solvent-induced changes in polarity, van der Waals forces and surface tension.

These helices are stabilized by hydrogen bonds and π-π interactions.

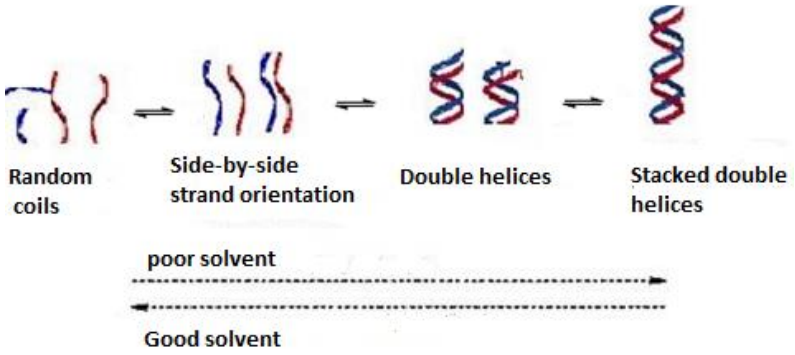

Figure 1: The designed double helix assembly system.

Additionally, the hierarchical organization of the pPATs in the presence of templates and anions was investigated. The pPATs' template and anion guided assembly processes was tracked by circular dichroism (CD), UV-Vis and STEM microscopies upon introduction of a rigid hydrophobic polypeptide template and compared with untemplated assembly structures and processes.

The targeted foldable and labelled chiral pPATs (**Figure 2**) were prepared in a series of reactions involving synthesis of monomers, the CuAAC mediated A-B step growth polyaddition of the monomers [15, 16] and post-polymer labelling with fluorescent dyes. The achiral pPAT **1** (**Figure 2**) was also synthesized purposely to compare the influence of chirality in the assembly processes.

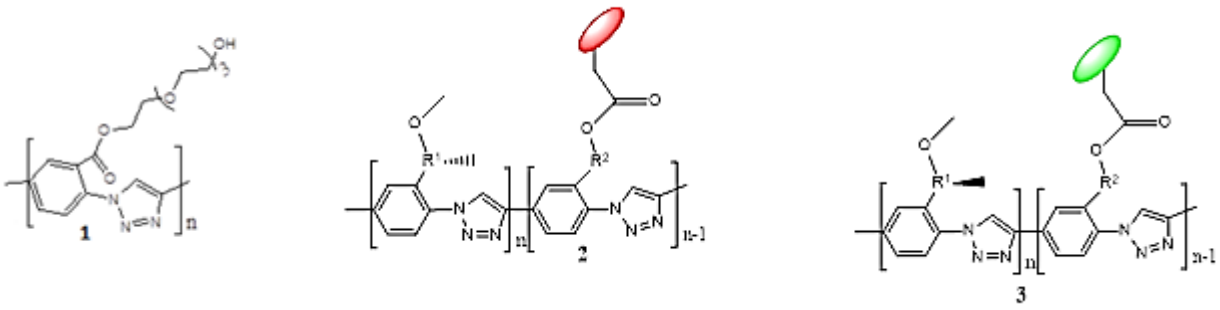

Figure 2: Target labelled pPATs.

To distinguish the handedness of the helices, monitor and track their individual folding and double helix assembly processes and interactions in suitable solvents *via* fluorescent signals, the (*R*)- and

(*S*)-pPATs were tagged with dyes of different and contrasting colors. Further evidence for the pPATs' helical folding processes and other assembly interactions as influenced by chirality transfer, through ''sergeants and soldiers'' experiments, were obtained and studied *via* circular dichroism (CD) and UV-Vis spectroscopies.

1.3. Organization of the thesis

This work is divided into six chapters. In Chapter 1, the background is discussed and the general aim briefly highlighted. Chapter 2 deals with a brief literature review. With examples from the literature, the design and factors that govern the folding processes of different types of polymer backbones into foldamers are briefly discussed with special emphasis given to double helices, which form the background for this work. The conformational influence of chirality in the helix folding and assembly processes is also given some attention. Cu(I)-catalyzed azide alkyne cycloaddition (CuAAC), which was utilized in the synthesis of poly(*para*-aryltriazoles) is also discussed in this chapter.

In chapter 3, novel π-conjugated polymeric backbones based on *para*-aryltriazoles, incorporating dyes of contrasting colors and chirality in the side chains, are presented and subsequently analyzed using NMR. The synthesis and characterization of the suitable *para*-alkyne and azide functionalized aryl monomers will be discussed in detail as well as their polymerization, *via* the Cu(I)-catalyzed 1,3-dipolar cycloaddition reaction, to afford the desired (pPATs) and subsequent incorporation of the dyes *via* post-polymer esterification reactions. The self-assembly of our labeled pPATs from random coils into double helices as a function of solvent quality and side chain chirality will be studied as well as compared *via* the spatial distribution of the fluorescent signals and elaborate CD and UV-Vis spectroscopies.

In Chapter 4, template and anion-guided assembly of our pPATs is investigated *via* elaborate UV-Vis and CD studies and the spatial distribution of the fluorescent signals. The stability, size and length of the template-controlled and uncontrolled structure formed in the absence of the template are

compared. The stability, size and length of both the template controlled and uncontrolled structures formed were compared.

In Chapter 5, an insight into the fundamentals of chirality transfer and amplification is presented with an examination of 'sergeants and soldiers' principle and 'majority rule' via elaborate UV-Vis and CD spectroscopic studies on pPATs containing different amounts of both chiral and achiral side chains. Importantly, we will report on the co-operativity between the small chiral side chains (sergeants) and majority achiral side chains (soldiers) that cause the achiral components to 'follow' the helicity of the small chiral components as result yielding bias in the folding handedness of the helices.

Finally, Chapter 6 provides a brief summary of this work highlighting the conclusions drawn from the experimental work, observation and analysis. Recommendations for future endeavors emanating from this work are also highlighted.

REFERENCES

1. J. X. Chen, J. W. Han and H. N. C. Wong, *Org. Lett*., **2015**, 17, 4296−4299.
2. Y. Furusho and E. Yashimaj*, Polym. Sci. Part A: Polym. Chem.*, **2009**, 47, 5195 – 5207.
3. X. Y. Ji, M. Q. Zhao, F. Wei, and X. Q. Feng, *Appl. Phys. Lett*., **2012**,100, 263104.
4. G. M. Whitesides and B. Grzybowski, *Science,* **2002**, 295, 2418-2421.
5. G. M. Whitesides, J.P. Mathias and C. T. Seto*, Science,* **1991**, 254, 1312-1319.
6. J.M. Lehn, *Science,* **2002**, 295, 2400-2403.
7. K. A. Dill, *Biochemistry*, **1990**, 29, 7133-7155.
8. M. Gingras, *Chem. Soc. Rev*., **2013**, 42, 968−1006.
9. Y.Tanaka, H. Katagiri, Y. Furusho and E. Yashima, *Angew. Chem. Int. Ed.*, **2005**, 44, 3867−3870.
10. T. Sugimoto, T. Suzuki, S. Shinkai and K. Sada, *J. Am. Chem. Soc*., **2007**, 129, 270−271.
11. M. Gingras, G. Félix and G. Peresutti, *Chem. Soc. Rev.*, **2013**, 42, 1007−1050.
12. A. E. Rowan and R. J. M. Nolte, *Angew. Chem*., **1998**, 110, 6571.
13. B. Wua, K. D. Piatkevicha, T. Lionnet, R. H. Singer and V. Verkhusha, *Current Opinion in Cell Biology,* **2011**, 3, 310–317.
14. K. D. Piatkevich, V. Verkhusha, *Current Opinion in Chemical Biology*, **2010**, 1, 23–29.
15. V. V. Rostovtsev, L. G. Green, V. V. Fokin and K. B. Sharpless, *Angew. Chem. Int. E*d., **2002**, 41, 2596-2599.
16. A. J. Qin, J. W. Y. Lam and B. Z. Tang, *Chem. Soc. Rev*., **2010**, 39, 2522.
17. H. Juwarker, J. Suk and K. Jeong, *Chem. Soc. Rev*., **2009**, 38, 3316–3325.
18. I. Huc and H. Jiang, *in Supramoleculr Chemistry; From Molecules to Nano Materials*, **2012**, John Wiley and Sons Ltd, Chichester, West Sussex.
19. M. Potschka, M. H. J. Koch, M. L. Adams and T. M. Schuster, *Biochemistry*, **1988**, 27, 8481.
20. L. J. Prins, P. Timmerman and D. N. Reinhoudt, *J. Am. Chem. Soc.,* **2001**, 123, 10153-10163.
21. I. Destoop, H. Xu, C. Oliveras-Gonza´lez, E. Ghijsens, D. B. Amabilino and S. De Feyter, *Chem. Commun.,* **2013**, 49, 7477-7479.

CHAPTER 2. ASSEMBLY OF FOLDAMERS AND DOUBLE HELICES; AN OVERVIEW

2.1 Introduction to foldamers

Foldamers are macromolecules that fold into definite and conformational ordered states in solution, thus mimicking biomacromolecules [1, 2]. The ordered states include;

- Helices
- Turns
- Sheets

The propensity of any oligomeric and/or polymeric strand to adopt a folded conformation (helix, turn or sheet) depends on a number of internal and external factors such as overall shape and rigidity of the strand, conformational restrictions, and the ability to establish attractive and repulsive intermolecular non-covalent interactions [3, 4]. The majority of foldamers possess intramolecular hydrogen bonds that guide their folding. In addition to hydrogen bonds, non-polar interactions such as van der Waals, solvophobic forces and π-π interactions can also be implemented in guiding and controlling the formation of the helical structures of synthetic foldamers [2-6].

Foldamer synthesis, therefore, involves the designing of appropriate modular building blocks/monomers that possess the necessary chemical and structural functionalities (information) to guide the polymerization and folding processes [3, 4]. Amides are a popular motif as their synthesis is generally facile and offers the benefits of both hydrogen bond acceptor and donor, a feature that nature has undoubtedly exploited in controlling the secondary and higher order structures of polypeptides. Nitrogen heterocycles such as pyridines, quinolones and triazoles are also an increasingly popular motif in functional foldamer design, due to their strong, directional dipoles [4]. The control of dipolar direction can result in helical cavities with ionic binding capabilities. Also, ethynylene linkers have been used to connect monomers in a variety of foldamer backbones due to their rigidity, solvophobicity and benign reactivity [9-14].

2.2 Classification of foldamers

Foldamers are broadly classified into two categories based on the nature of the backbones and/or building blocks [1, 2], namely; Peptidomimetic and Aryl strand foldamers.

2.2.1 Peptidomimetic foldamers

Closest to natural helices, peptidomimetic foldamers are derived from natural or synthetic amino acids and they remain the most studied class of foldamers. Examples include α-peptide and β-peptide helices [5]. α-Peptide helices such as **4** (**Figure 3**) are known to adopt the α-helix conformation while the β-peptide **5** (**Figure 3**) adopt several distinct helical conformations, depending on the substitution pattern at backbone Cα and Cβ atoms.

2.2.2 Aryl strand foldamers

Aryl strand foldamers, which are derived from rigid aromatic building blocks, consist of aromatic repeating units in the backbone [3, 4]. They have attracted increasing attention in recent years due to desirable optical/electronic properties and applications in host-guest chemistry. These properties, which not given by the individual building units, emerge in foldamers through electronic coupling or overlap of π-orbitals and organization of functional groups on the foldamer [3, 4, 7].

A wide range of aryl strand foldamers have been reported. The type and the stability of folded conformations depend on the size and shape of strands, linkage orientation, rotational restrictions, local intramolecular interactions and solvents [8]. Generally, they are classified into three categories according to the factors that govern their folding [8]. These factors include local conformational preferences, solvents and guest binding.

Conformational preference-based foldamers include a crescent and a hexagon-shaped helices that formed by three/four and more than six monomers, respectively, oriented at 120^0 [8]. Other examples include examples of aryl-aryl and aryl-amide foldamers designed using conformational preferences at the linkages between consecutive building blocks. The *para* substituted aromatics form well-defined rods such as **10** (**Figure 3**) [16] while assembling units that alternatively bend in

one direction and the direction opposite to it, result in zigzag shape **9** (**Figure 3**) [17]. When all units contribute to strand bending, a crescent or helix is formed as shown in **Figure 3** (**6**, **7**, **8** and **11**) [3, 4 and 7].

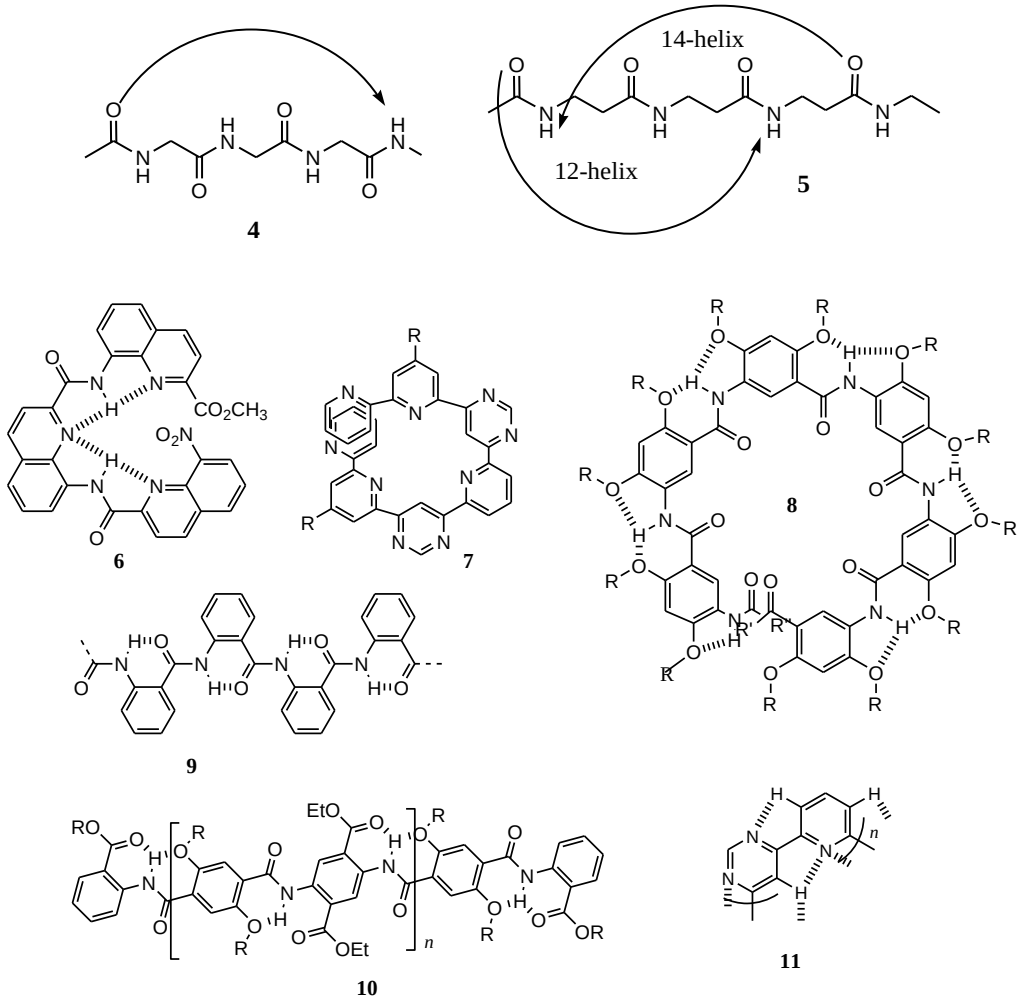

Figure 3: Illustration of hydrogen bonding in α-peptide and β-peptide helices **4** and **5**. The numbers 12 and 14 shown in β-peptide **5** correspond to the number of atoms participating in a ring created by intra-chain hydrogen bonds and molecular formula of aryl-aryl and aryl-amide foldamers (**6** – **11)** designed using conformational preferences.

Solvent induced foldamers have also been reported. In solvents, the dipoles of molecules tend to lead to them associating together to reach the most stable H-bonded status. An example is a series

of foldamers from *m*-phenylene-ethynylene (*m*PE) **12** shown in **Scheme 1**. The folding was dictated by solvophobic interactions. A random-coil state in chloroform is efficiently converted to a coiled, compact helical conformation, stabilized by π-π stacking between the aromatic units, in acetonitrile. Upon folding, a tubular, hydrophobic cavity is created into which hydrophobic small molecules of complementary size and shape were shown to bind reversibly. Also, foldamers that show conformational shifts have been reported. An example is the shift between transoid **13** and cisoid **14** (**Scheme 1**) [9-14].

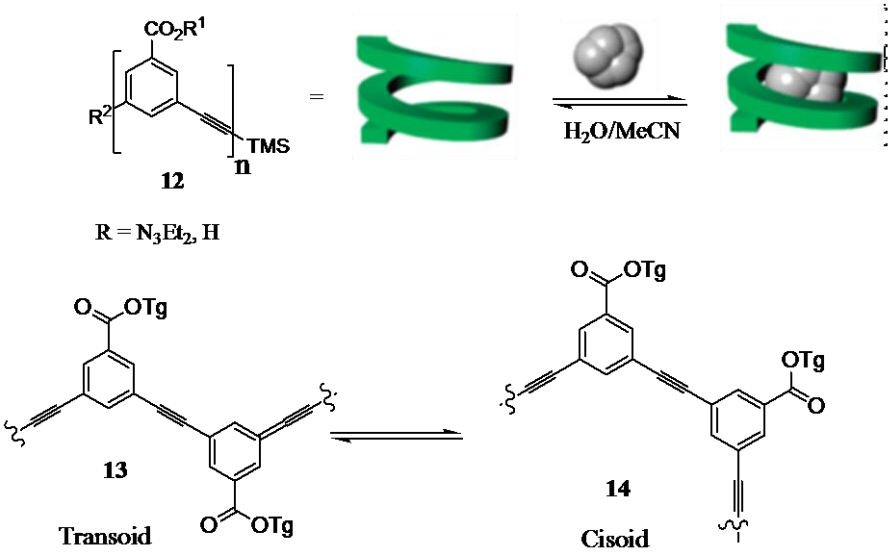

Scheme 1: mPE foldamers and conformational transition between transoid and cisoid conformations.

Hydrazide based foldamers **15**, **16** and **17** that form uniformly sized spherical vesicles on heating in methanol have also been reported [15]. Compounds **15** and **16** shown in **Figure 4** gelled in aliphatic hydrocarbon solvents presumably due to π-stacking as well as intertwining of the aliphatic side chains.

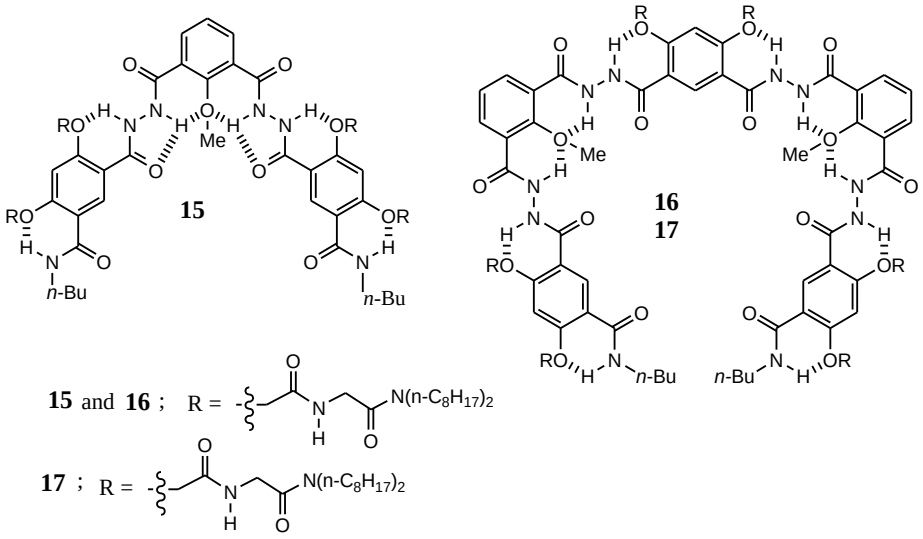

Figure 4: Foldamers that form gels and vesicles.

The design of foldamers based on guest binding involves the use of anions, cations and neutral organic molecules to induce the folding of flexible polymer strands. Examples of guest binded foldamers include oligoindoles with *S*-trans conformed linkages between the indole units reported by Jeong and coworkers [18]. Conversion to *S*-cis conformation was observed in the presence of chloride ions. Also, a water-soluble indolocarbazole foldamer **20** shown in **Scheme 2** that binds to halides in aqueous media has been reported by Suk and Jeong and co-workers [19]. This indolocarbazole folds into a helical conformation, with an internal cavity encircled by multiple neutral hydrogen bond donors.

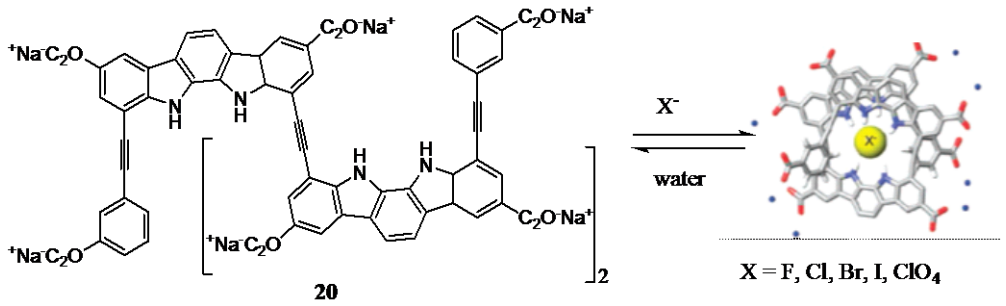

Scheme 2: Suk and Jeong's helix with an internal cavity.

Neutral organic molecules have also been used as templates to induce flexible oligomers to fold. Examples include oligo-(pyridine-ethylenes) possessing alkoxy side chains such as **21**. The folding of oligomer **21** into a helix **23** with preferred handedness was induced by a saccharide **22** as shown in **Scheme 3** [20].

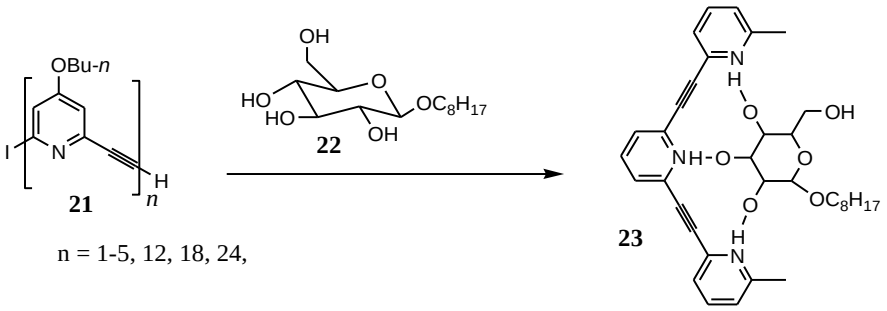

Scheme 3: Saccharide induced folding and binding of poly and oligo-(pyridine-ethylenes).

The use of neutral organic molecules to induce folding and stabilize the foldamers has been reported. An example is the binding of *m*PE foldamer **25** having various lengths (and thus tubular cavities of various lengths) to rod-like guests such as diphenyl-piperidine **24** as shown in **Scheme 4** [21].

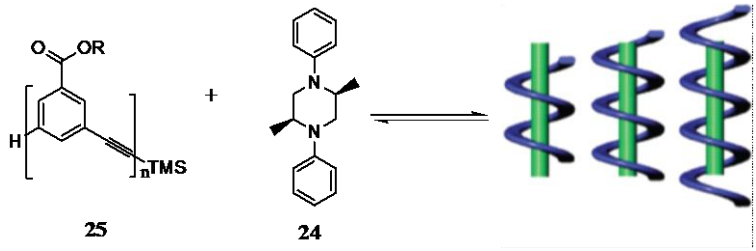

Scheme 4: Binding of mPE foldamers having various lengths to rod-like guests.

2.3 Characterization of foldamers

The analysis and characterization of foldamers is accomplished by circular dichroism (CD) spectroscopy, UV-Vis spectroscopy, fluorescence spectroscopy, nuclear magnetic resonance (NMR) spectroscopy, X-ray studies, TEM and SEM. These spectroscopic techniques have been used in the

analysis of secondary, tertiary and quaternary structures of proteins and peptides, both qualitatively and quantitatively. Circular dichroism (CD) measures the difference in the absorption of left-handed circularly polarized light (L-CPL) and right-handed circularly polarized light (R-CPL) that occurs when a molecule contains one or more chiral chromophores (light-absorbing groups) [22,23]. This technique is sensitive to environment, temperature, concentration, solvent and pH. It can also be used to observe how a secondary structure changes with environmental conditions or on interaction with other molecules. Structural, kinetic and thermodynamic information about macromolecules can also be derived from circular dichroism specroscopy. UV-Vis spectroscopy is used to detect the presence of helical conformations and is commonly used to establish the conditions, such as solvents, temperature and concentrations for the aggregation and organization of polymeric or oligomeric strands from random coils to helices/foldamers [22].

NMR spectroscopy provides detailed structural information about macromolecules at atomic resolution [22-24]. However, this detailed view of molecular structure results from a laborious examination of a number of conformational sensitive parameters and the application of distance geometry programs. Using peptides, it has been observed that protons involved in helical conformations produce up-field NMR shifts compared to non-bonded free protons [25]. X-ray crystallography can also be used to characterize foldamers [22]. However, crystallographic studies require high-quality single crystals which for many foldamers are not possible. Also, the relatively "static" structure in single crystals does not adequately represent the secondary structure conformation in a complex and dynamic environment. TEM and SEM are types of electron microscopic techniques. SEM is based on scattered electrons and focuses on the foldamer/helix surfaces and their composition. It mainly shows the morphology of foldamers. TEM is based on transmitted electrons and provides details about internal composition. Unlike SEM, TEM shows several characteristics of the foldamer/helix, such as morphology, crystallization, stress and magnetic domains.

2.4 Chirality and folding; conformational preferences

Polymer strands assume helical conformations as a result of a screw sense adopted during folding to produce a racemate of *M*- and *P*- helices. The introduction of optically active sites or chiral centres into the foldamer structures discriminates both helix types leading to diastereomeric pairs of helices, differing in energy [26, 27]. In nature, the exclusive choice of one enantiomer over the other, as building block for defined secondary structures and self-assemblies is evident. For example, control over the intrinsic helicity of DNA structure is governed by the peripheral chirality in the sugar–phosphate backbone [42].

Similarly, chiral centres incorporated in artificial foldamers control through conformational bias the folding and assembly processes. Optical sites can either be incorporated into the strand (backbone) [28-30], the side chains [31-33] or be induced by chiral guests via supramolecular interactions [34, 35]. When the optically active site is present in the side chain, chirality transfer to the backbone depends on the distance of the chiral centre to the folding backbone and the flexibility of the spacer in between [36], the degree of intramolecular backbone order [37], the packing mode of the side chains and the amount of chiral side chain incorporation. Increasing the distance between the side chain chiral centre and the backbone, diminishes chirality transfer to the backbone.

Also, the incorporation of small amounts of chiral side chains drives the assemblies to form domains with a particular handedness. This phenomenon referred to as 'Sergeants and Soldiers', involves small chiral units (sergeants) controlling the overall chirality and therefore (folding handedness) of achiral segments (soldiers) through cooperative interactions in the side chains [38, 39]. Examples of chirality controlled folding include a series of phenanthroline-derived oligoamides, such as **28** (**Scheme 5**), bearing a chiral (*R*)-phenethylamino end group from the carboxylic acid **26** and amine **27**. Chirality transfer from the end group afforded one-hand helical foldamers in solution [40]. On protonating the phenanthroline group at one of the two nitrogen atoms, an acid and base controllable switch in the phenanthroline dicarboxamide-based helical molecular strands was obtained.

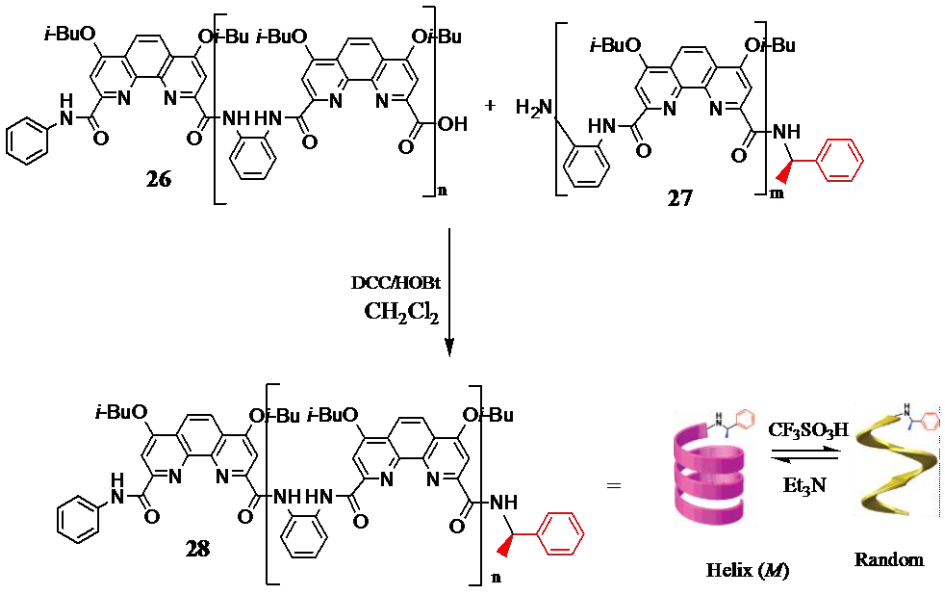

Scheme 5: Folding of chiral phenanthroline-derived oligoamides.

Also, guided by chirality, bifunctional ureido-*S*-triazine **29** bearing chiral penta(ethyleneoxide) side chains, assembles in water to helical columns via cooperative stacking of the hydrogen bonded pairs **30** (DADA array) as shown in **Scheme** 6 [41]. The chiral side chains attached to the ureido-*S*-triazine units bias the helicity of these columns as concluded from CD spectroscopy and ‘‘Sergeants and Soldiers’’ experiments.

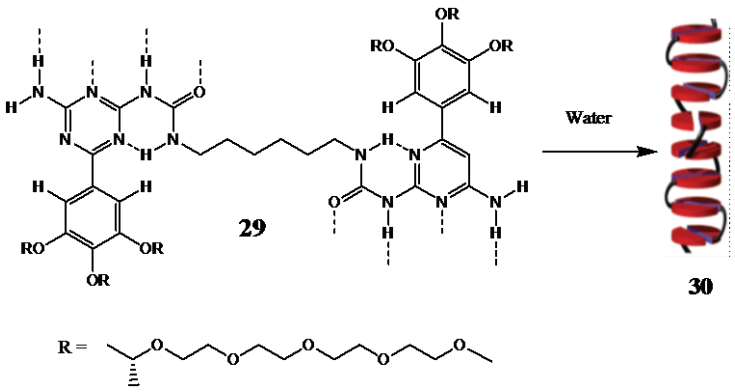

Scheme 6: Ureido-*S*-triazines bearing penta(ethyleneoxide) side chains that self-assemble in water.

2. 5 Introduction to double helices

Double helices are supramolecular duplexes of single strands. Their history dates back to the discovery of DNA's double helix in 1953 [97]. Extensive efforts to explore how synthetic oligomers and polymers can mimic natural DNA to self-assemble into artificial double-helix have led to the unravelling of the factors that govern the adoption of the folded conformations. These factors include the ability of oligomeric or polymeric materials to establish attractive and repulsive intermolecular non-covalent interactions such as hydrogen bonding, van der Waals forces, solvophobic interactions and π-π interactions to initiate, guide and control the assembly of helical structures [8, 43].

Synthetic polymers and oligomers that fold into helical conformations have been designed and synthesized, however, many of them are single helices. So far only a few structural motifs that form double helices have been reported. Examples include helicates (**31**) [44], aromatic oligoamides (**32**) [45] and double-helical oligomer (**35**) [46] that consists of two complementary molecular strands bound together through amidinium-carboxylate salt bridges (**Figure 5**).

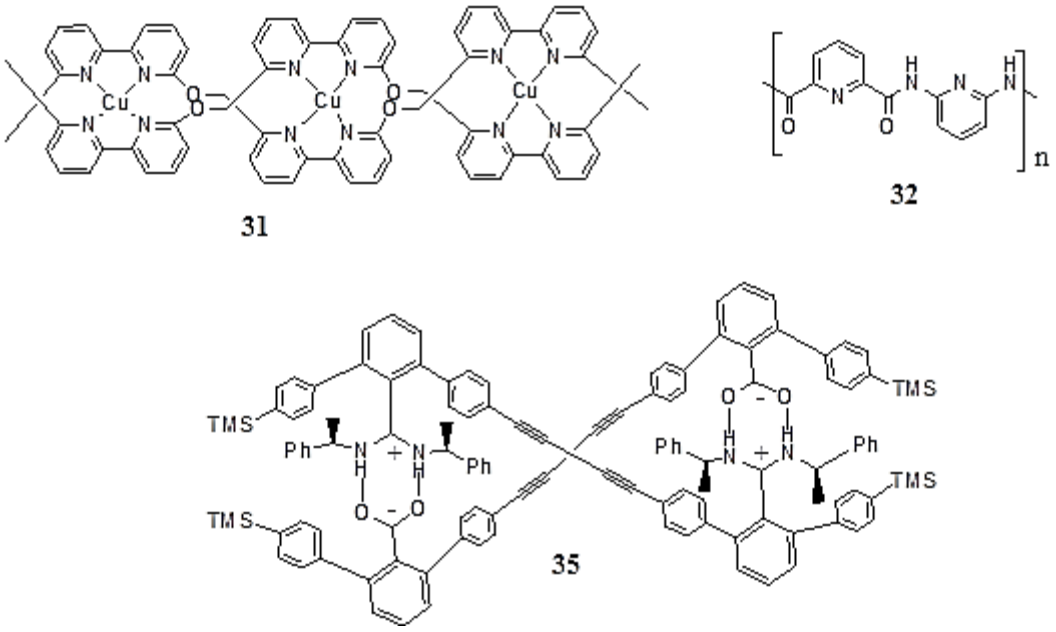

Figure 5: Structural motifs for double helices.

Considering that double helices are supramolecular duplexes of the single strands, succeeding in their design requires utilization of non-covalent weak interactions as a "glue" to intertwine the molecular strands. In the next section, double helices are classified by the non-covalent interactions used for binding molecular strands such as van der Waals, aromatic and hydrogen bonding interactions which sometimes may include metal coordination, salt bridges and solvophobic effects [47 – 50].

2. 5. 1 Types of double helices

2.5.1.1 Double helices through aromatic Interactions

These types of double helices are derived from the interactions of strands consisting of aromatic repeating units in the backbone. Their organization into double helices is mainly driven by π-π interactions. Examples include oligoresorcinols such as **36** (**Figure 6**), which form double helices in water [51]. Oligoamides that organise into double helices by inter-strand hydrogen bonds and π-π interactions have also been reported. Lehn and co-workers demonstrated that both single and

double helices of **37** can be formed and be crystallized from different media (**Figure 6**). The single helix crystallized from a polar solvent mixture (DMSO/CH_3CN) ratio, while the double helix crystallized from a less polar solvent mixture (nitrobenzene/heptane) ratio [52].

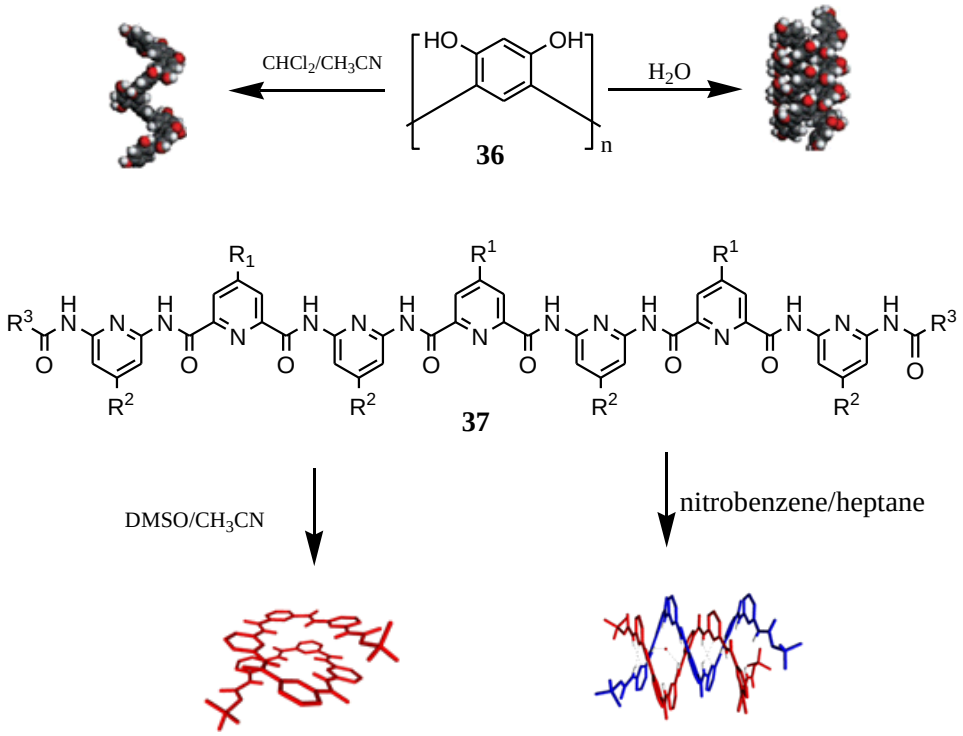

Figure 6: Double helices from oligoresorcinols.

Single and double helices from oligoamides **38** which are stabilized by local preferential conformations at arylamide linkers and intermolecular π-stacking interactions between aromatic groups (**Figure 7**) have been reported [53].

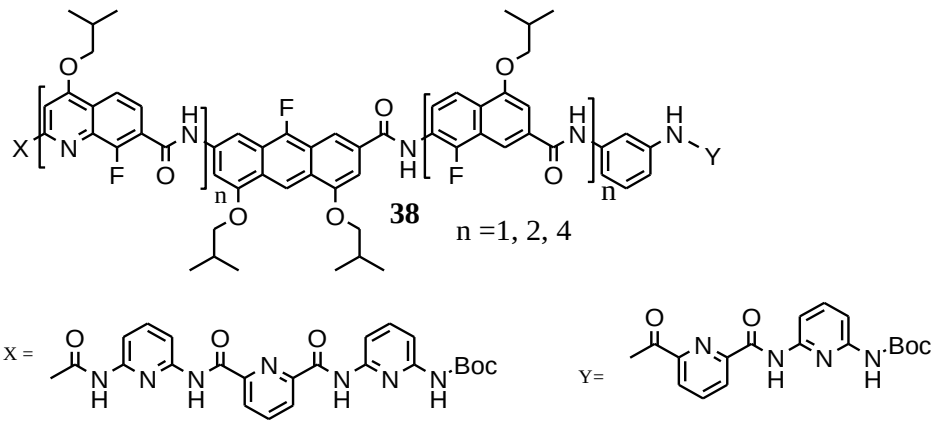

Figure 7: Examples of oligoamides that form single and double helices by local preferential conformations.

Yashima *et al.* also reported poly(*m*-phenylene) **39** bearing an achiral oligo(ethylene oxide) chain at the 5-position that adopts a single helical conformation in protic media and a double helix in water through aromatic interactions (**Figure 8**) [54]. It was concluded that these helices are stabilized by π-π interactions.

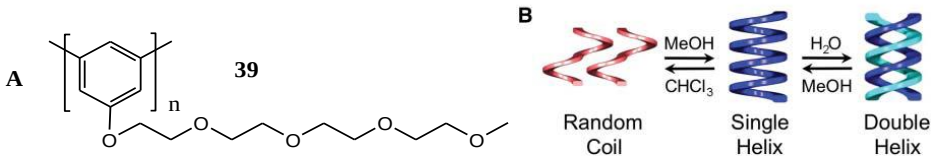

Figure 8: Single and double helix formation from poly(*m*-phenylene) bearing an achiral oligo(ethylene oxide) chain.

Oligoresorcinol nonamer **40**, a unique *π*-conjugated oligomer, self-assembles into double stranded helix through aromatic interactions in water [55, 56]. The double helix further unravels and entwines upon complexation with specific cyclic and linear oligosaccharides with a particular chain length or glucosidic linkage pattern, such as β- and *γ*-cyclodextrins (β- and *γ*-CyDs) and α-1,6-disomaltooligosaccharides,respectively, thus forming a twisted pseudorotaxane and a hetero duplex with a preferred-handed helical conformation (**Figure 9**). The double helices formed in

water exist as equimolar mixtures of the right- and left-handed helices. The introduction of an optically active group into the structure of **40** shifts the equilibrium to induce a bias in the twist sense, resulting in a distinct Cotton effect. In methanol, however, the oligoresorcinol showed no CD as expected because it exists in random-coil conformations.

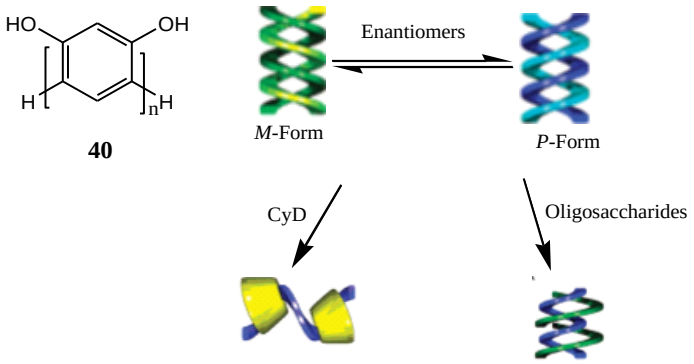

Figure 9: Schematic illustration of the unwinding of the double helix **40** and the formation of a hetero double helix with oligosaccharides.

2.5.1.2 Double helices through template binding

The design of helices based on template binding involves the use of anions, cations and neutral organic molecules to induce the folding of flexible polymer strands into helices.

Like in the macroscopic world, a chemical template organizes reaction partners and thus allows the chemist to control their reactivity to achieve the formation of a desired product or folding pattern. Examples of templated double helices include enantiomerically pure chiral bicyclic guanidinium salt **41** (**Figure 10**) that is organized into a double stranded helical structure by anionic sulfate template [57].

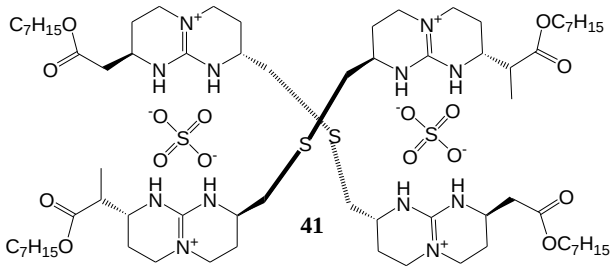

Figure 10: Sulfate templated double helix.

Also a double-stranded metallosupramolecular helical polymer, (*R*)- or (*S*)-poly-**43** (Scheme 7) was formed from **42** by a combination of the salt bridges and metal-ligands as templates [58].

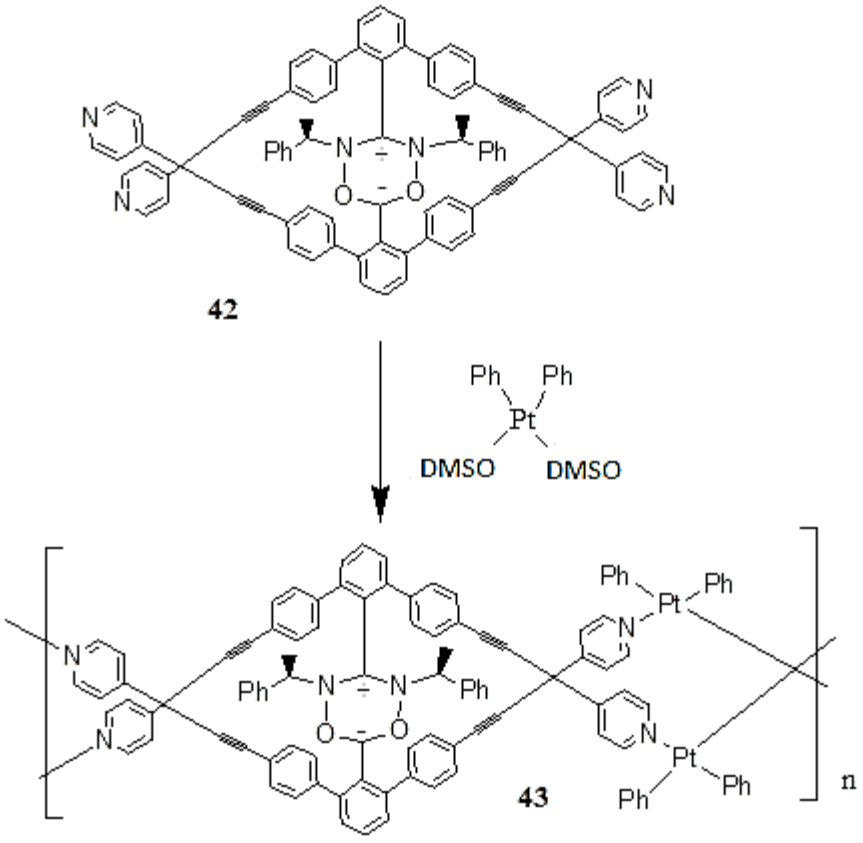

Scheme 7: Double-stranded metallosupramolecular helical polymer.

2.5.1.3. Double helices through salt bridges

Salt bridges comprises of two non-covalent interactions; hydrogen bonding and electrostatic interactions, which stabilize entropically unfavorable folded conformations. One example used for the construction of supramolecular architectures is amidinium-carboxylate salt bridges that have well-defined geometry with the ability to generate complementary pairs of supramolecular double helical complexes in a controlled manner with high association constants [59, 60]. Yashima and co-workers demonstrated that two complementary sequences can form double-helical structures via amidinium-carboxylate salt bridges [61] (**Scheme 8**). When **44** was mixed with **45** in chloroform, the duplex **46** containing two salt bridges was formed as shown in **Scheme 8.** Circular dichroism spectra revealed that the formation of the double helical complex resulted in an enhancement of the weak Cotton effects exhibited by *R*- or *S*-**44** in the region of 260 nm to 370 nm in chloroform.

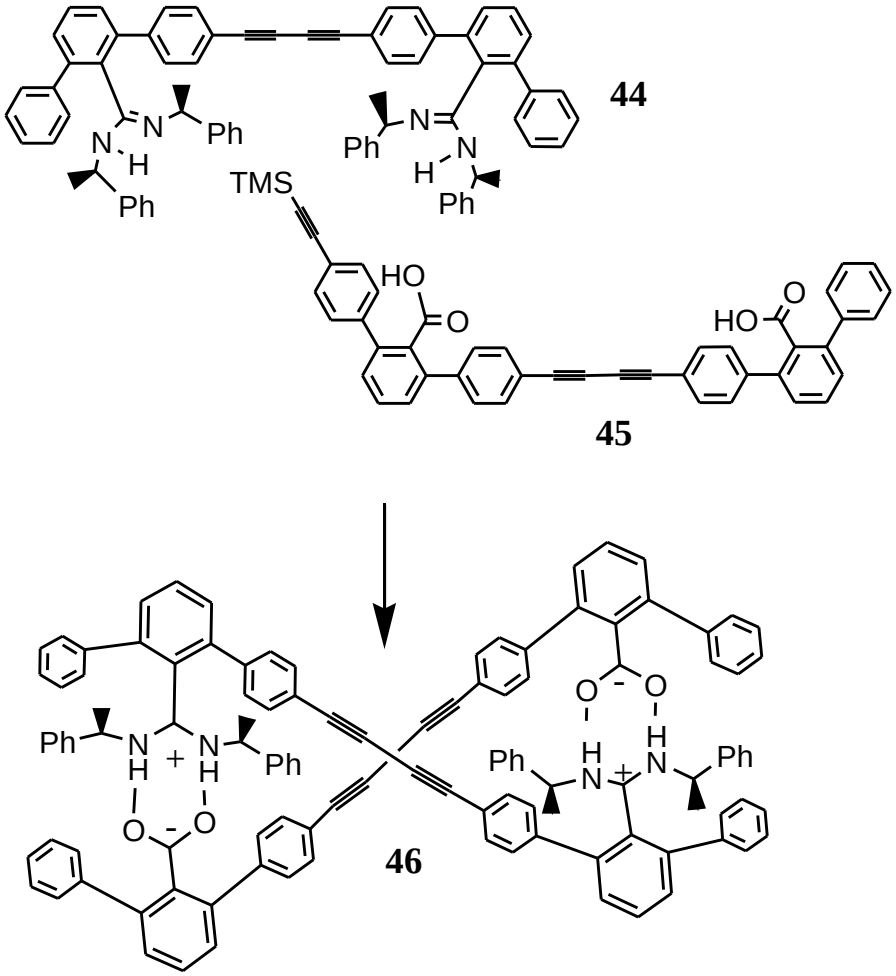

Scheme 8: Salt bridged double helix formation.

2.5.1.4 Double helices through van der Waals forces

Van der Waals forces are weak attractions and repulsions between atoms, molecules, and surfaces. Changes in van der Waals forces reduce surface energy in an assembly system and deform the single strands that then form a double helix depending on the competition between the surface energy and the elastic strain energy [62]. The changes in van der Waals forces can be caused by interfacial adhesion, solvents or temperature. An example is the perylene-tetracarboxylic dianhydride (PTCDA) double helix micro fibrils assembled from achiral helical columns through changes in the van der Waals forces [63]. Temperature-driven changes in the van der Waals forces and surface

free energy among adjacent micro fibrils forced the micro fibrils into layer-layer arrangement (close contact). This was followed by the same-handed rotation coil on one another to form a double helix and the release the internal stress and achieve a more stable double morphology and a balance between the altered van der Waals force and surface free energy.

2.6 Applications of helical polymers

Potential applications of helical polymers involve enantioselective catalysis [64, 65, and 66]. An example is a complementary double-stranded dimer of **47** composed of an achiral amidine strand and carboxylic acid strand bridged by achiral diphosphines that was enantioselectively prepared, through covalent or non-covalent bondings. By taking full advantage of the "helicity induction and memory" effect, the alkynyl units on **47** can accommodate metal ions such as Cu(I) in a tweezer-like manner (**Scheme 9**) [67].

Further, the double helical complex of **47** with Cu(I), **47**-Cu(I), catalyses the asymmetric cyclopropanation reaction of styrene **48** with ethyl diazoacetate **49**, thus producing anoptically active product **51** with 85% enantiometric excess (ee). These results suggest that the chiral space generated by the double-helical structure is effective and indispensable for the high enantioselectivity, thus providing a promising and conceptually new strategy in the broad field of supramolecular catalysis with a unique double-helical structure.

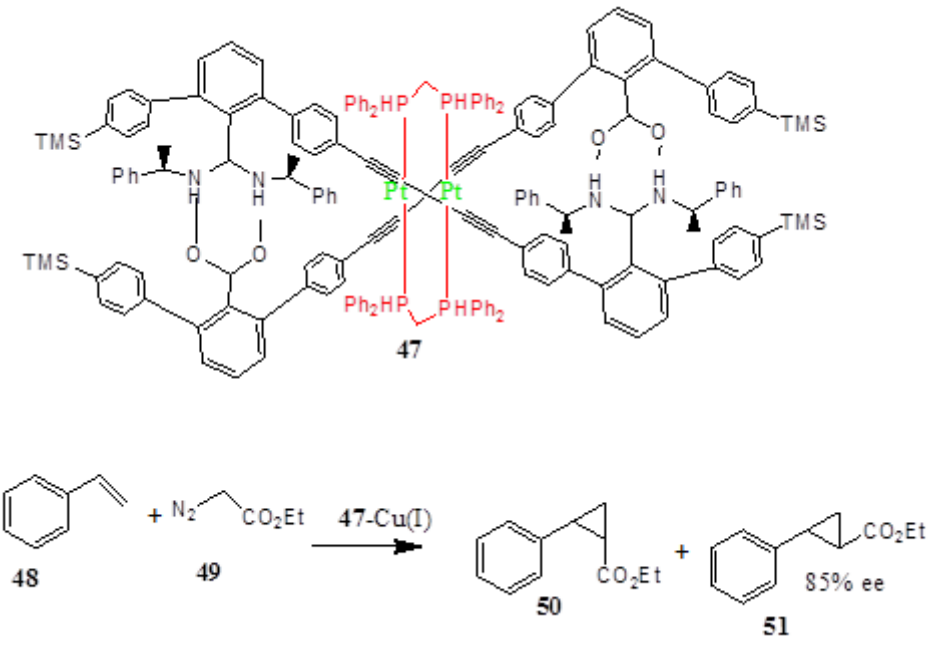

Scheme 9: Complementary double-stranded dimer of **47** and asymmetric cyclopropanation reaction of styrene **48** with ethyl diazoacetate **49.**

Helical polymers are also utilized as asymmetric catalysts, but successful examples are rare, except for the one-handed helical polymethacrylate **52 (Figure 11).** Polymethacrylate complexes with palladium form a catalyst for asymmetric allylic alkylations [68]. Also, a dynamic helical polyisocyanate **53** (**Figure 11**) forms an effective catalyst for asymmetrical hydrogenation when complexed with rhodium [68]. Also, rigid-rod helical polymers with a controlled helical sense have also been employed as novel scaffold or template to spatially organize various functional groups and or reactants, in a one-handed helical array along the polymer backbones through covalent or non-covalent bonds. The strategy has been applied to control the superstructure of conjugated polymers using anionic synthetic lipid assemblies as a template as shown in the **Figure 11**. The anionic template assemblies harbour the cationic intermediates produced by oxidative polymerization of the monomer, for example, pyrrole [69]. A SEM image of the resulting poly-(pyrrole) films showed fibrous structures with a left-handed helical motif, similar to the structure of the organic templates.

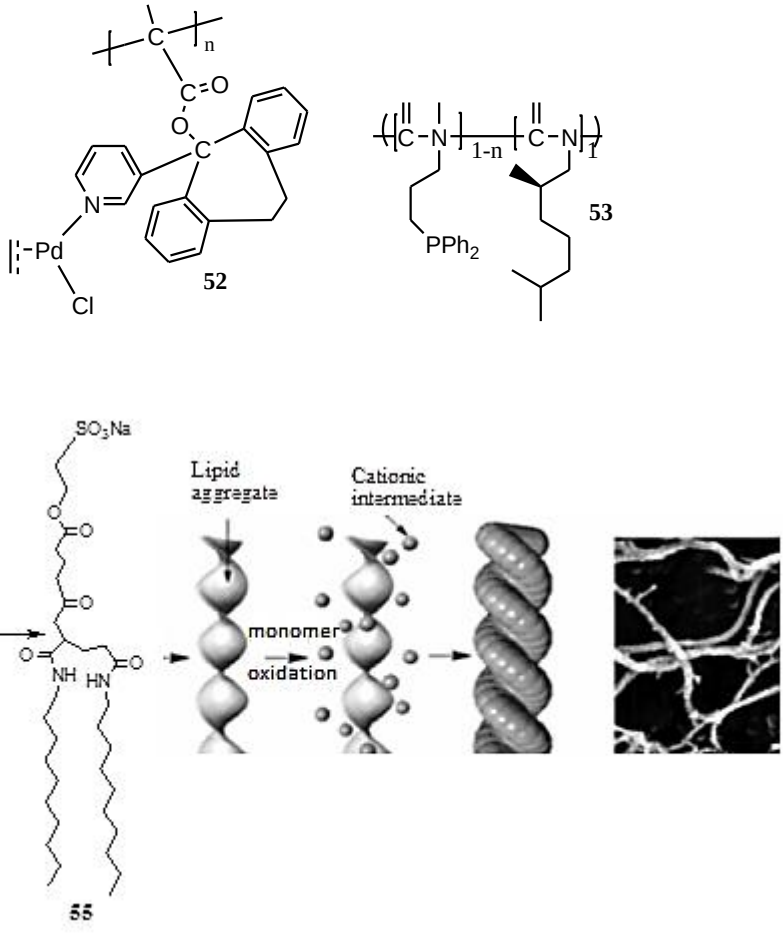

Figure 11. Helical polymers **52** and **53** are used as asymmetric catalysts, and SEM image of a poly-(pyrrole) composite film obtained by a templating method.

2.7 Cu(I)-catalyzed click polymerization

2.7.1 Introduction

"Click" chemistry was introduced in 2001 to describe chemical transformations that have high chemical yields, are regiospecific, generate inoffensive by-products and are insensitive to oxygen and water [78].

Reactions which conform to click chemistry criteria have been studied and their applications for polymerization are well documented [71-73]. Examples of these click reactions applied for polymer synthesis include the Cu(I)-catalyzed azide-alkyne cycloadditions, nitrile oxide-alkyne cycloaddition, and thiol-ene/thiol-yne click reactions [73].

The Cu(I)-catalyzed 1,3-dipolar cycloaddition reaction, which utilizes building blocks such as acetylenes and azides to form disubstituted triazole rings is the most extensively studied click reaction to date. This reaction (**Scheme 10**), which is considered the most reliable hetero Diels Alder addition [74], proceed regioselectively to yield disubstituted tetrazoles such as **56** [75, 76] and 1,2,3-triazoles [77-79] such as **57** with Cu(I) catalysis under different conditions. This reaction has been applied for the design and synthesis of advanced multifunctional polymer materials [70-72].

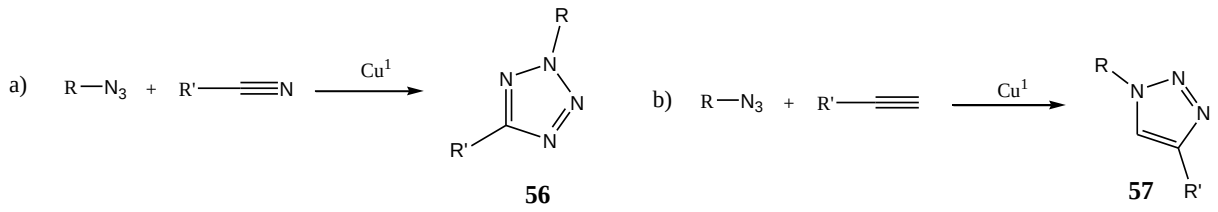

Scheme 10: Examples of a Cu(I)-catalyzed Huisgen 1,3-dipolar cycloaddition.

2.7.2. Cu(I)-catalysis and mechanism for the formation of 1,4-disubstituted triazole

The mechanism for the CuAAC which was first proposed by Sharpless *et. al*. [80] based on experimental observation and later modified by Finn *et. al.* [81, 82] has been determined from DFT calculations [83, 84]. The Cu(I) species is introduced as a preformed complex or generated *in situ* [70, 79, 85]. Coordinated by a ligand, the Cu(I) species forms a π-complex with the triple bond of the terminal alkyne. In a basic environment, the terminal acetylene hydrogen being the most acidic is deprotonated to yield a copper acetylide intermediate as shown in **Figure 12**. It has been suggested that the transition state involves two copper atoms. One copper atom is bonded to the acetylide while the other copper atom activates the azide.

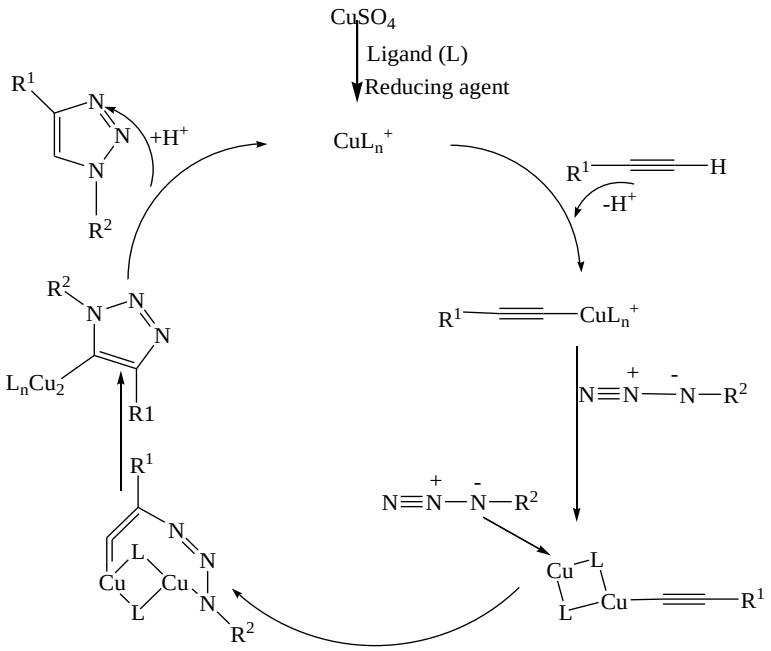

Figure 12: Postulated Cu(I) catalysis mechanism [70, 79, 85].

The ligands employed are labile and weakly coordinating hence the azide displaces one ligand to generate a copper-azide-acetylene complex. Cyclisation then takes place, followed by protonation. The product is then formed by dissociation.

The Cu(I) species lowers the pK_a of the alkyne C-H by up to 9.8 units when coordinated with acetylide [84]. In a non-catalyzed reaction the alkyne remains a poor electrophile, leading to slow reaction rates due high energy barriers.

2.7.3 Click polymerization

CuAAC click polymerization is the use of Cu(I)-catalyzed click reactions of azides and alkynes, thiols and alkenes or alkynes *etc.* using different Cu(I) catalysts, ligands and solvents for the synthesis of a wide range of functionalized polytriazoles. To afford different polytriazole architectures, the

strategy of using monomer combinations with different types and numbers of click cycloaddition functionalities such as azides (A) and terminal alkynes (B) is employed [92-94].

Examples of click polymers include hyper-branched PAT **65** from ethynylene diazide **64** (AB_2 type monomer) *via* a polyaddition strategy based on click chemistry step-growth polymerization [95] in a water/DMF mixture according to Scheme **11**. Scheme **11** also shows an example of 1,4-regioregular linear PAT **68**, prepared from diazide **66** (A_2) and diyne **67** (B_2) monomers through A_2+B_2 monomer combination strategy [93].

Hyper-branched polytriazole **69** prepared from diazine and triyne (A_2 +B_3 monomer combination) has been reported [73]. The growing polymer species in the aqueous reaction media agglomerated and eventually precipitated due to poor solubility. However, this challenge was successfully solved by minimizing the amount of water in the solvent mixture [94 – 96]**.**

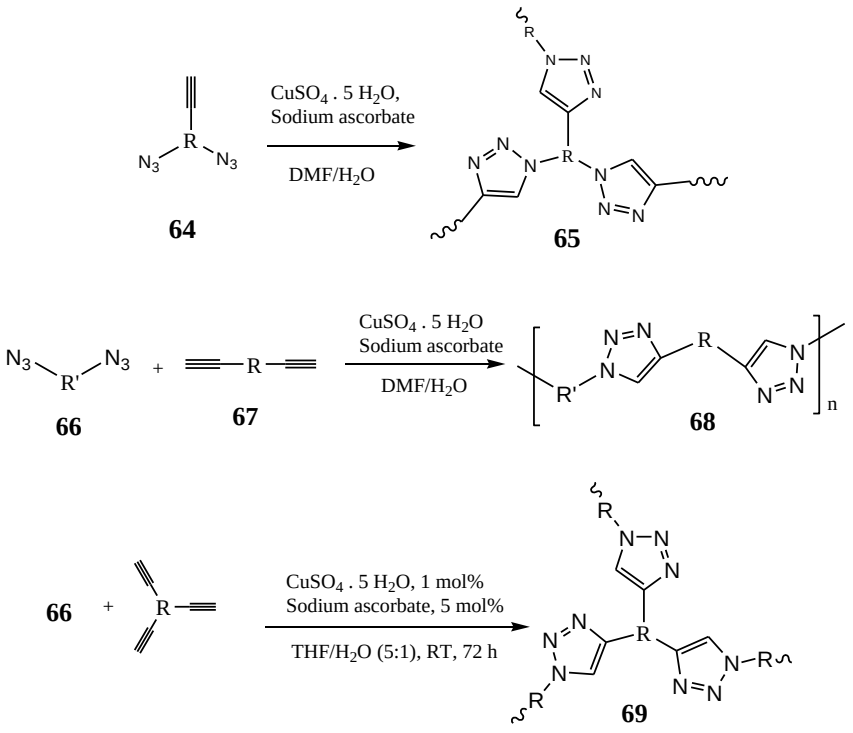

Scheme 11: Examples of CuAAC "click" polytriazoles.

2.7.4 Aryl triazole-based foldamers and helices

Utilization of aryl azides and acetylenes generates a backbone of embedded helicogenic motifs based on alternating triazole and aryl moieties [78, 81]. Rotation about a minimal number of connecting bonds leads to folding into a helical conformation that is enthalpically stabilized by π-π stacking and hydrogen bonding interactions. The planar trizole unit has favorable properties that make it well suited for supramolecular chemistry of foldamers such as binding to cations, anions and neutral guests. These properties are derived from the three electronegative sp^2 hybridized nitrogens which are nested on one side of the ring and the electropositive C^5-H group, which offers minor steric hindrance [86-88].

Meudtner and Hecht demonstrated the design and synthesis of novel class of triazole-based clickamers, *via* the click reaction [38]. The clickamers **58** and **59** (**Figure 13**), which contain two complete turns with a number of π–π stacking units, showed very insignificant folding behavior in acetonitrile. The population of the helical conformation was observed upon the addition of substantial amounts of water. The helicity upon addition of water is due to the intramolecular chirality transfer from the chiral side chains to the backbone, which is evidenced from temperature dependent circular dichroism (CD), as well as dynamic light-scattering (DLS) and UV-Vis absorption spectroscopy studies.

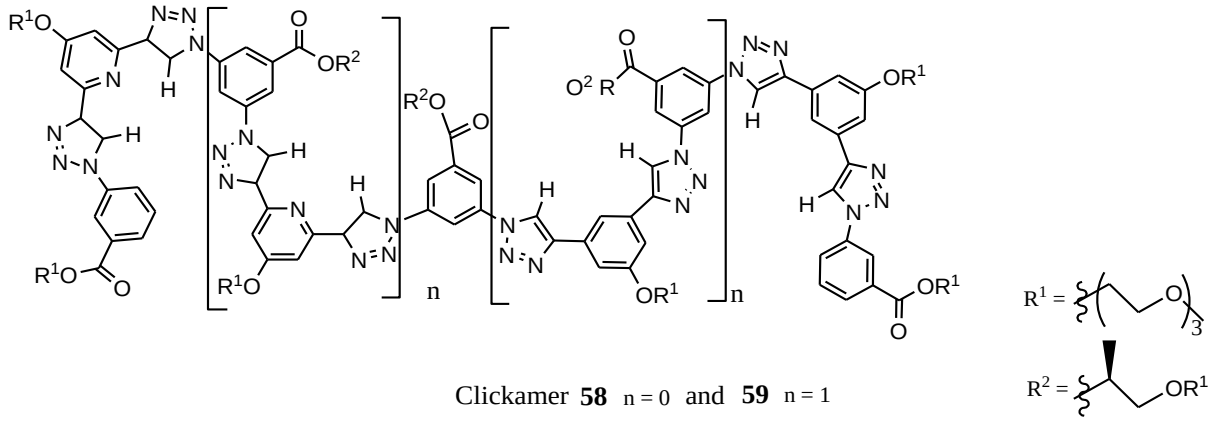

Figure 13: Triazole-based foldable clickamers.

Another interesting example is the 2,6-bis(1,2,3-triazol-4-yl)pyridine (BTP) subunits of poly[(1,2,3-triazol-4-yl-1,3-pyridine)-alt-(1,2,3-triazol-1-yl-1,3-phenylene)] **60** that have a preference to assume an anti–anti conformation enabling the extended hetero aromatic polymer strands to adopt a helical conformation as shown in **Scheme 12** [89]. Addition of various transition metal ions leads to coordinative cross-linking and therefore efficient gelation of the polymer solutions.

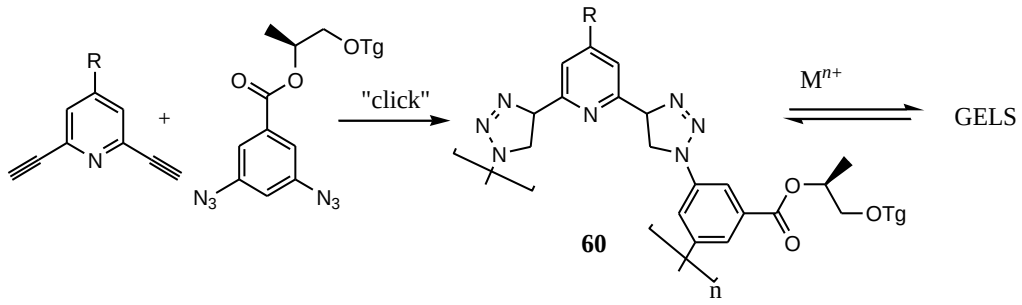

Scheme 12: Synthesis of poly [(1,2,3-triazol-4-yl-1,3-pyridine)-alt-(1,2,3-triazol-1-yl 1,3-phen-lene)] foldamers and gels.

Light-induced triazole-based foldamer **61**, shown in **Scheme 13**, containing a photo responsive azo-benzene in between the two phenyl-triazole oligomer units which adopts *trans*- or *cis*- with respect to the azo-linkage has been reported [90]. The *cis*-isomer **63** predominates upon irradiation with UV light; however, it binds to anions more strongly than the *trans*-conformer. This is due to its scissor-like conformation, which results in assembling all the binding sites ideally for the recognition of ions. The *trans*-conformer **62** predominantly exists in the presence of visible light, and in comparison with *cis*-conformer, it binds weakly to various anions, due to the extended conformation of the azo-benzene core.

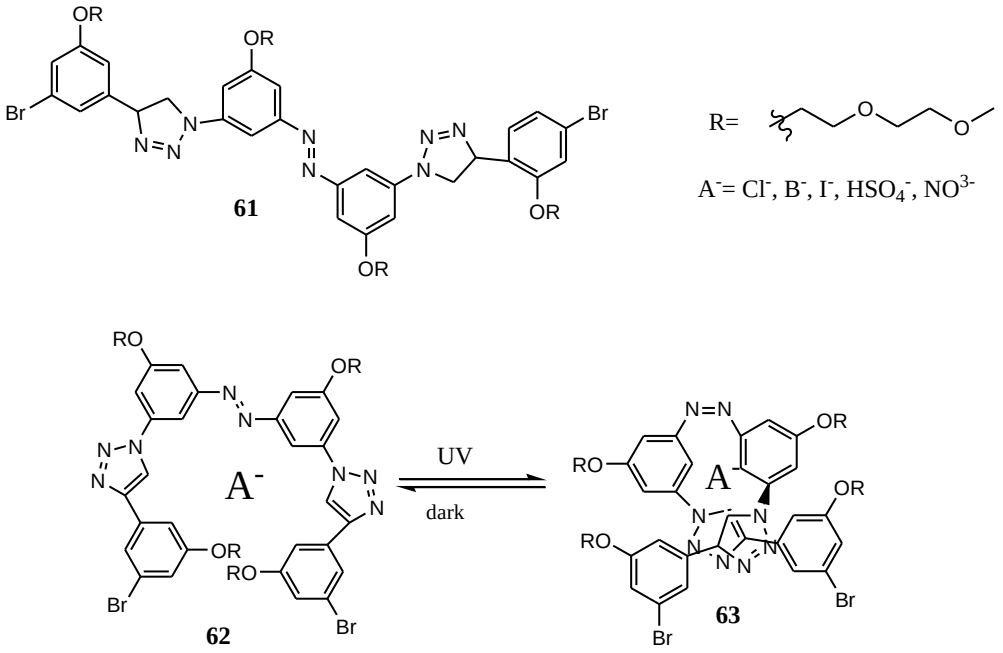

Scheme 13: Photo switchable triazole receptor.

2.7.4 Challenges of click polymerization

Exciting and remarkable progress has been made in recent years in the exploration of metal mediated click polymerization systems. This has led to the development of better and effective organo-soluble catalysts of Cu(I) and other metals for the synthesis of linear and hyper-branched polytriazoles with regioregular molecular structures and advanced functional properties [73]. However, there are few challenges such as the toxicity and interference of copper catalysts on PAT properties and the underutilization of other click reactions besides the azide–alkyne cycloaddition that still need attention.

The polymers obtained from the metal-catalyzed click polymerizations may be difficult to purify due to incomplete removal of the metal catalyst residues from the polymeric products owing to the ability of these triazoles to bind and form complexes with metal ions [98]. Of particular importance is that the metallic residues are generally detrimental to the electronic and optical properties of

polymers [99]. Light emissions of conjugated polymers, for example, can be quenched by metallic traps [99]. Furthermore, the transition-metal catalysts are expensive and cytotoxic, which then becomes more problematic when the polymerizations are conducted in biological systems or when the polymers are used for biological applications [91]. Minimal use of metallic catalysts and development of efficient metal-free polymerization systems are thus highly desired. To foster click polymerization into a versatile tool for the construction of new macromolecules with well-defined structures and multifaceted functionalities, new polymerization routes based on other clickable reactions should be developed [91]. Hence, the exploration on the use of other clickable reactions for polymer synthesis, besides the highly documented and successful Cu(I)-catalyzed azide alkyne cycloaddition, remains a challenge to polymer scientists in their quest to realize the full potential of the click polymerizations.

REFERENCES

1. S. Hecht, I. Huc, *Foldamers: Structure Properties and Applications*; Wiley-VCH: Weinheim, Germany, **2007**.
2 D. J. Hill, M. J. Mio, R. B. Prince, T. S. Hughes and J. S. Moore, *Chem. Rev.,* **2001**, 101, 3893.
3 D. M. Basani, J. M. Lehn, G. Baum and D. Fenske, *Angew. Chem. Int. Ed*. Engl.,**1997**, 36, 1845.
4 B. Gong, H. Zeng and J. Zhu, *Proc. Natl.*, **2002**, 99, 11583.
5 J. A. Patch and A. E. Barron, *Current Opinion in Chemical Biology,* **2002**, 6:872–877.
6 E. G. Emberly, N. S. Wingreen and C. Tang, *Proc. Natl.,* **2002**, 99, 11163-11168.
7 H. Jiang, J. M. Leger and I. Huc, *J. Am. Chem. Soc*., **2003**, 125, 3448.
8 I. Huc and H. Jiang, *In Supramoleculr Chemistry; From Molecules to Nano Materials*, **2012**, John Wiley and Sons Ltd, Chichester, West Sussex.
9 J. C. Nelson, J. G. Saven, J. S. Moore and P. G. Wolynes, *Science*, **1997**, 277, 1793.
10 R. B. Prince, S. A. Barnes and J. S. Moore*, J. Am*. *Chem. Soc*., **2000**, 122, 2758.
11 M. T. Stone and J. S. Moore, *Org. Lett*., **2004**, 6, 469.
12 A. Tanatani, M. J. Mio and J. S. Moore, *J. Am. Chem. Soc*., **2001**, 123, 1792.
13 A. Tanatani, T. S. Hughes and J. S. Moore, *Angew. Chem., Int. Ed*., **2002**, 41, 325.
14 K. Goto and J. S. Moore, *Org. Lett*., **2005**, 7, 1683.
15 W. Cai, G. T. Wang, Y. X. Xu, X. K. Jiang and Z. T. Li, *J. Am. Chem. Soc*., **2008**, 130, 6936.
16 Z. Q. Wu, X. K. Jiang, S. Z. Zhu and Z. T. Li, *Organ. Lett.*, **2004**, 6, 229.
17 Y. Hamuro, S. J. Geib and A. D. Hamilton, *J. Am. Chem. Soc*., **1996**, 118, 7529.
18 K. J. Chang, B. N. Kang, M. H. Lee and K. S. Jeong, *J. Am. Chem. Soc*., **2005**, 127, 12214.
19 J. M. Suk and K. S. Jeong, *J. Am. Chem. Soc*., **2008**, 130, 11868.
20 M. Inouye, M. waki, and H. Abe, *J. Am. Chem. Soc*., **2001**, 123, 1792.
21 A. Tanatani, M. J. Mio and J. S. Moore, *J. Am. Chem. Soc*., **2004**, 126, 2022.
22 J. T. Pelton and L. R. McLean, *Analyt. Biochem*., **2000**, 277**,** 167-176.
23 A. Violette, M. C. Averlant-Petit, V. Semetey, C. Hemmerlin, R. Casimir, R. Graff, M. Marraud, J. P. Briand, D. Rognan and G. Guichard, *J. Am. Chem. Soc*., **2005**, 127, 2156-2164.
24 K. Wuthrich, *J. Bio. Chem.*, **1990**, 265, 22059-22062.

25 L. Szilagyi and O. Jardetzky, *J. Magn. Reson*., **1989**, 83,441.

26 T. Nakano and Y. Okamoto, *Chem. Rev.*, **2001**, 101, 4013-4038.

27 Y. Okamoto and T. Nakano, *Chem. Rev*., **1994**, 94, 349-372.

28 H. Y.Hu, J.-F. Xiang, Y. Yang and C.-F. Chen, *Org. Lett*., **2008**, 10, 69–72.

29 P. K., Boruah, R. Gonad, P. R. Rajamohanan, H.-J. Hofmann and G. J. Sanjayan, *J. Org. Chem.,* **2007**, 72, 5077–5084.

30 Z. Zhong and Y. Zhao, *Org. Lett*., **2007**, 9, 2891–2894.

31 R. M. Meudtner and S. Hecht, *Angew. Chem*. Int. Ed., **2008**, 47, 4926–4930.

32 H. Masu, M. Sakai, K. Kishikawa, M. Yamamoto, K. Yamaguchi and S. Kohmoto, *J.Org. Chem.,* **2005**, 70, 1423–1431.

33 A. Khan, C. Kaiser and S. Hecht, *Angew. Chem., Int. Ed*., **2006**, 45, 1878–1881.

34 H. Abe, H. Machiguchi, S. Matsumoto and M. Inouye*, J. Org. Chem*., **2008**, 73, 4650–4661.

35 H. Goto and J. S. Moore, *Org. Lett.,* **2007**, 7, 1671–1673.

36 D. B. Amabilino, J.-L. Serrano, T. Sierra and J. Veciana, *J. Polym. Sci., Part A: Polym.Chem*., **2006**, 44, 3161-3174.

37 B. M. W. Langeveld-Voss, R. A. J. Janssen and E. W. Meijer, *J. Mol. Struct*., **2000**, 521, 285-301.

38 L. J. Prins, P. Timmerman and D. N. Reinhoudt, *J. Am. Chem. Soc., **2001,** 123, 10153-10163.*

39 I. Destoop, H. Xu, C. Oliveras-Gonza´lez, E. Ghijsens, D. B. Amabilino and S. De Feyter, *Chem. Commun.,* **2013**, 49, 7477—7479.

40 H. Y. Hu, J. F. Xiang, Y. Yang and C. F. Chen, *Org. Lett*., **2008**, 10, 1275-1278.

41 L. Brunsveld, J. A. J. M. Vekemans, J. H. K. K. Hirschberg, R. P. Sijbesma, and E. W. Meijer, *PNAS*, **2002,** 99, 8, 4977–4982.

42 K. A. Dill, *Biochemistry,* **1990**, 29, 7133-7155.

43 H. Juwarker, J.-M. Suk and K.-S. Jeong, *Chem. Soc. Rev*., **2009**, 38, 3316–3325

44 44 J.-M. Lehn, *Supramolecular Chemistry: Concepts and Perspectives;* VCH: Weinheim, Germany, **1995**.

45 I. Huc, *Eur. J. Org. Chem*., **2004**, 17–29.

46 Y. Tanaka, H. Katagiri, Y. Furusho and E. Yashima, *Angew. Chem., Int. Ed*. **2005**, 44, 3867–3870.

47 M. Gingras, *Chem. Soc. Rev*., **2013**, 42, 968−1006.

48 Y. Tanaka, H. Katagiri and Y. Furusho, *Angew. Chem., Int. Ed*. **2002**, 44, 3867–3870.

49 T. Sugimoto,T. Suzuki, S. Shinkai and K. Sada, *J. Am. Chem. Soc*., **2007**, 129, 270−271.

50 M. Gingras, G. Félix and G. Peresutti, *Chem. Soc. Rev***., 2013**, 42, 1007−1050.

51 H. Goto, H. Katagiri, Y. Furusho and E. Yashima, *J. Am. Chem. Soc.,* **2006**, *128*, 7176.

52 (a) V. Berl, I. Huc, R. G. Khoury, M. J. Krische, J. M. Lehn, *Nat.,* **2000**, *407*,720. (b) V. Berl, I. Huc, R. G. Khoury, M. J. Krische and J. -M. Lehn, *Chem. Eur. J,* **2001**, *7*, 2810.

53 Q. Gan, Y. Ferrand, C. Bao, B. Kauffmann, A. Grelard, H. Jiang and I. Huc, *Science,* **2011**, *331*, 117.

54 T. Ben, Y. Furusho, Hi. Goto, K. Miwac and E. Yashima, *Org. Biomol. Chem*., **2009**, 7, 2509– 2512.

55 H. Goto, H. Katagiri, Y. Furusho and E. Yashima, *J. Am. Chem. Soc. ,***2006**, *128*, 7176–7178.

56 H. Goto, Y. Furusho, K. Miwa and E. Yashima, *J Am Chem Soc*, **2009**, 131, 4710–4719.

57 J. Sanchez-Quesada, C. Seel, P. Prados and J. de Mendoza, *J. Am. Chem. Soc.,* **1996**, 118, 277.

58 Y. Furusho and E. Yashimaj, *Polym. Sci. Part A: Polym. Chem*., **2009**, 47, 5195 – 5207.

59 (a) A. Kraft, L. Peters and H. R. Powell, *Tetrahed.,* **2002**, *58*, 3499. (b) J. Otsuki, K. Iwasaki, Y. Nakano, M. Itou, Y. Araki and O. Ito, *Chem. Eur. J.,* **2004**, *10*, 3461. (c) F. Corbellini, L .di Constanzo, M. Creges-Calama, S. Geremia and D. N. Reinhoudt, *J. Am. Chem. Soc.,* **2003**, *125*, 994.

60 (a) H. Goto, H. Katagiri, Y. Furusho and E. Yashima, *J. Am. Chem. Soc.,* **2006**, *128*, 7176. (b) H. Goto, Y. Furusho and E. Yashima, *J. Am. Chem. Soc.,* **2007**, *129*, 109. (c) H. Goto, Y. Furusho and E. Yashima, *J. Am. Chem. Soc.,* **2007**, *129*, 9168. (d) H. Goto, Y. Furusho, K. Miwa and E. Yashima, *J. Am. Chem. Soc.,* **2009**, *131*, 4710.

61 Y. Tanaka, H. Katagiri, Y. Furusho and E. Yashima*, Angew. Chem. Int. Ed.,* **2005**, *44*, 3867.

62 X. Ji, M. Zhao, F. Wei and X. Feng, *Appl. Phys. Lett.,* **2012**, 100, 263104.

63 X. Jia, S. Lou, H. Yuan, R. Yuan, S. Tian, C. Niu, X. Licand and S. Zhou, *J. Mater. Chem. C*, **2015**, 3, 79.

64 T. Nakano and Y. Okamoto, *Chem. Rev.,* **2001**, *101*, 4013–4038.

65 K. Maeda and E. Yashima, *Top. Curr. Chem.,* **2006**, *265*, 47–88.

66 (a) R. J. M. Nolte, *Chem. Soc. Rev.,* **1994**, 23, 11–19. (b) D. B. Amabilino, J.-L. Serrano, T. Sierra and J. Veciana, *J. Polym. Sci., Part A: Polym. Chem*., **2006**, 44, 3161–3174.

67 T. Hasegawa, Y. Furusho, H. Katagiri and E. Yashima, *Angew. Chem*., Int. Ed. ***2007*****,** 46, 5885–5888.

68 M. Reggelin, S. Doerr, M. Klussmann, M. Schultz and M. Holbach, *Proc. Natl***., 2004**, 101, 5461– 5466.

69 T. Hatano, A. H. Bae, M. akeuchi, N. Fujita, K. Kaneko, H. Ihara, M. Takafuji and S. Shinkai, *Angew. Chem., Int. Ed*. **2004**, 43, 465-469.

70 V. V. Rostovtsev, L. G. Green, V. V. Fokin and K. B. Sharpless, *Angew. Chem. Int. Ed*., **2002**, 41, 2596-2599.

71 J. E. Hein and V. V. Fokin, *Chem. Soc. Rev*., **2010**, 39, 1302.

72 P. L. Golas and K. Matyjaszewski, *Chem. Soc. Rev*., **2010,** 39, 1338.

73 A. J. Qin, J. W. Y. Lam and B. Z. Tang, *Chem. Soc. Rev*., **2010**, 39, 2522.

74 G. W. Goodall and W. Hayes, *Chem. Soc. Rev*., **2006**, 35, 280.

75 Z. P. Demko and K. B. Sharpless, *J. Org. Chem*., **2001**, 66, 7945.

76 Z. P. Demko and K. B. Sharpless, *Angew. Chem. Int. Ed*., **2002**, 41, 2110.

77 J. Scheel, H. Komber and B. I. Voit, *Macromol. Rapid Commun*., **2004**, 25, 1175.

78 W. H. Binder and C. Kluger, *Macromolecules*, **2004**, 37, 9321.

79 C. W. Tornoe, C. Christensen and M. Meldal, *J. Org. Chem*., **2002**, 67, 3057.

80 V. O. Rodionov, V. V. Fokin and M. G. Finn, *Angew. Chem. Int. Ed.,* **2005**, 44, 2210.

81 S. Punna, J. Kuzelka, Q. Wang and M. G. Finn, *Angew. Chem. Int.Ed*., **2005**, 44, 2215.

82 G. Molteni and A. Ponti, *Chem. Eur. J*., **2003**, 9, 2770.

83 F. Himo, T. Lovell, R. Hilgraf, V. V. Rostovtsev, L. Noodleman, K. B. Sharpless and V. Fokin, *J. Am. Chem. Soc*., **2005**, 127, 210.

84 P. Appukkuttan, W. Dehaen, V. V. Fokin and E. van der Eycken, *Org. Lett*. **2004**, 6, 4223-4225.

85 A. J. Scheel, H. Komber and B. Voit, *Macromol. Rapid Commun*., **2004**, 25, 1175.

86 S. Kawano, S. Tamaru, N. Fujita and S. Shinkai, *Chem. Eur. J*., **2004,** 10, 343.

87 D. S. Goodsell, *Bionanotechnology,* Wiley-Liss, Hoboken, New Jersey, **2004.**

88 S. Anderson, H. L. Anderson and J. K. M. Sanders, *Acc. Chem. Res*., **1993**, 26, 469-475.

89 A. Imhof and D. J. Pine, *Nature,* **1997**, 389, 948-951.

90 Y. N. Xia, B. Gates, Y. D. Yin and Y. Lu, *Adv. Mater*., **2000**, 12, 693-713.

91 K. A. Dill, *Biochem.*, **1990**, 29, 7133-7155.

92 Y. Tang, C. K. W. Jim, Y. Liu, L. Ye, A. Qin, J. W. Y. Lam, C. Zhao and B. Z. Tang, *ACS Appl. Mater. Interfaces*, **2010**, 2, 566.

93 S. Hartwig and S. Hecht, *Macromolecules*, **2010**, 43, 242.

94 J. D. Xie, L. H. Hu, W. F. Shi, X. X. Deng, Z. Q. Cao and Q. S. Shen, *J. Polym. Sci., Part B: Polym. Phy*s., **2008**, 46, 1140.

95 Z. A. Li, G. Yu, P. Hu, C. Ye, Y. Q. Liu, J. G. Qin and Z. Li, *Macromolecules***, 2009**, 42, 1589.

96 A. Qin, J. W. Y. Lam, C. K. W. Jim, L. Zhang, J. Yan, M. Heaussler, J. Liu, Y. Dong, D. Liang, E. Chen, G. Jia and B. Z. Tang, *Macromolecules*, **2008**, 41, 3808.

97 (a) D. Haldar and C. Schmuck, *Chem. Soc. Rev.,* **2009**, 38*,* 363. (b) M. M. Green, J. W. Park, T. Sato, A. Teramoto, S. Lifson and R. L. B. Selinger, J. V. Selinger, *Angew. Chem. Int. Ed.,* **1999**, 38, 3138. (c) D. J. Hill, M. J. Mio, R. B. Prince, T.S. Hughes and J. S. Moore, *Chem. Rev.,* **2001**, 101, 3893. (d) T. Nakano and Y. Okamoto, *Chem. Rev.* **2001**, 101, 4013. (e) E. Yashima, K. Maeda and T. Nishimura, *Chem. Eur. J.,* **2004**, 10, 42. (f) E. Yashima, K. Meada, H. Lida, Y. Furusho and K. Nagai, *Chem. Rev.,* **2009**, 109, 6102.

98 D. Li, J. Tian, W. Gu, X. Liu and S. Yang, *J. Inorg. Biochem*., **2010**, 104, 171 – 179.

99 Z. Liu, Z. Yang, T. Li, B. Wang, Y. Li, D. Qin, M. Wang and M. Yan, *Dalt. Trans*., **2011**, 37, 9329 – 9620.

CHAPTER 3. DOUBLE HELIX SELF-ASSEMBLY FROM LABELED AND CHIRAL POLY (*p*-ARYL TRIAZOLES)

3.1 Introduction

The design and synthesis of macromolecules that assemble into stable, structurally well-defined higher order aggregates has been an active area of research for many years owing to their wide range of applications as biosensors, electronic and conductive materials, drug delivery agents, and use in anion and cation recognition and separation [1 – 4]. Specifically, self-assembly studies originated from investigations on the tobacco mosaic virus (TMV) and the enzyme ribonuclease. It was observed that TMV is composed of 2400 nucleotides in a single strand of RNA, encased in a protein sheath 3000 Å long and 180 Å in diameter. The protein sheath is formed from 2130 identical protein building blocks. The protein subunits define the shape of the helix and the RNA defines the helix length [5]. Furthermore, the assembly process was found to exhibit the concentration, time and pH dependency characteristics of a chemical reaction.

While other biological structures may need additional factors to facilitate or direct the assembly processes, the studies on the TMV assembly revealed the virtues of self-assembly such as control, error checking and efficiency [5]. Many assembly systems of higher order structures have been designed following these revelations from nature. As of now, a significant amount of information on design and synthesis of aryl macromolecules that assemble into foldamers, such as helices, and the insights of the forces and dynamics that drive self-organization is available in the literature, as discussed in Chapter 2.

Generally, polymeric strands assume helical conformations as a result of a screw sense adopted during folding [6, 7]. Several strategies such as local conformational preferences, solvophobic effects, cation/anion and guest binding have been utilized to impart a screw sense (Chapter 2). However, for solvophobic-induced organization, which will be utilized in this work, a solvent induced transition from a random, disordered conformation in “good” solvents (which effectively solvates the macromolecules) to an ordered, putative helical conformation in “poor” solvents

(which poorly solvates the macromolecules) is observed (**Figure 14**). These interactions are normally stabilized by non-covalent interactions such as hydrogen bonding and π-π stacking [8 – 10].

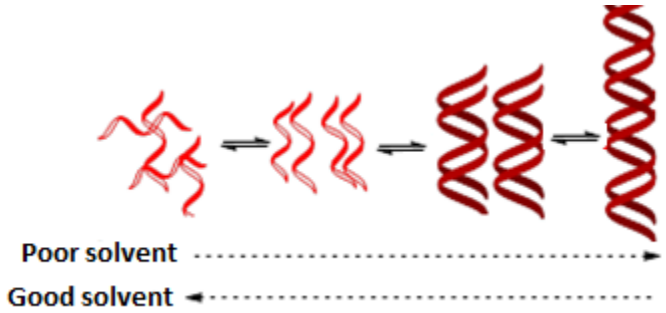

Figure 14: Schematic representation of double helix assembly upon changes in solvents.

With regards to conformational bias, optically active centres (chirality) on the polymeric backbone or side chains can impart a bias in the twist sense of the helical structure, giving rise to diastereomeric pairs of helices that differ in energy, and not a racemate of helices in a 1:1 ratio that is observed in the folding of achiral (macro) molecules as shown in **Figure 15** [11, 12]. However, when the optically active site is present in the side chain, chirality transfer to the foldamer backbone depends on the chiral centre's distance to the folding backbone and, consequently, increasing the distance between the side chain chiral centre and the backbone diminishes chirality transfer to the backbone [13].

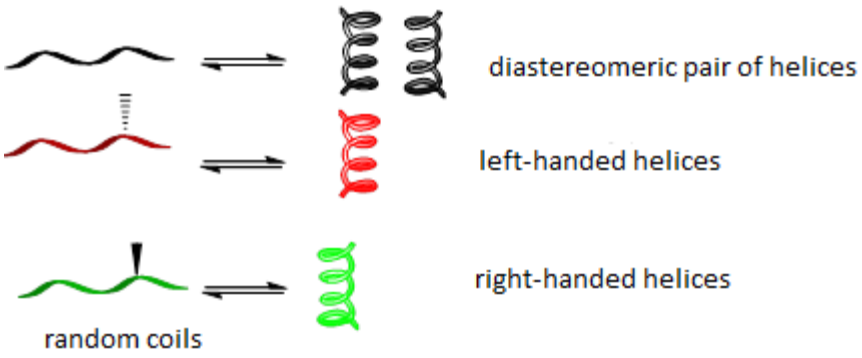

Figure 15: Bias in the twist sense.

There is no doubt that the principles of intermolecular interactions demonstrated in nature are inspiring the construction of hierarchical non-biological structures, particularly with aromatic repeating units due to their promising applications ranging from nano electronics, drug delivery systems, anion and cation binding, and biomaterials designed for cell scaffolding [1 – 4]. However, to design these assemblies for such attractive applications, detailed information concerning the conformational intermediates and pathways involved in the assembly is necessary.

In an effort to unravel the self-assembly pathways and processes and feasibly bridge the interaction gap between starting and final steps during hierarchical growth, we have designed poly(*p*-aryl-triazole)s (pPATs) that self-assemble from random coils, as a function of solvent quality and chirality of the building block, into conformational double helical foldamers in this chapter. The assembly from random coils into double helices, as a function of solvent quality and side chain chirality, is followed *via* elaborate UV-Vis and CD spectroscopic studies, and the spatial distribution of the fluorescent signals enabled experimental capture of the assembly's intermediate steps and structures.

The candidate pPATs (**Figure 16**), decorated with either (*R*)- or (*S*)-chiral side chains, are prepared in a series of reactions that involve the synthesis of azide and terminal alkyne functionalized monomers and polymerization of the monomers via the copper(I)-catalysed azide alkyne cycloaddition (CuAAC) mediated A-B step growth polyaddition. Further, the (*R*)- and (*S*)-pPATs **2** and **3** were expected to assemble into left- and right-handed helices. To visually differentiate the (*R*)- and (S)-pPATs (**2** and **3**) and investigate their individual folding and assembly processes and interactions the pPATs were tagged with different dyes of contrasting colours as shown in **Figure 16**.

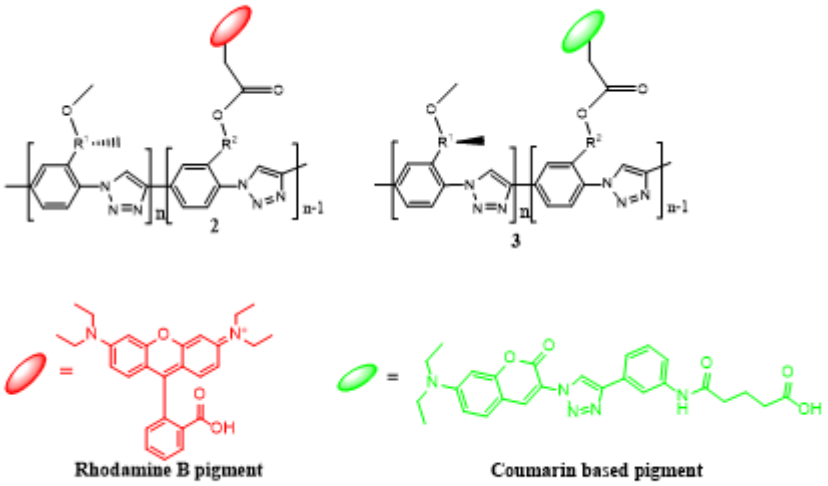

Figure 16: Targeted click-labeled pPATs for assembly studies.

3.2 Monomers synthesis

To obtain the targeted pPAT foldamers **2** and **3** (**Figure 16**) *via* CuAAC based step growth polymerization and subsequent post-polymerization labeling, three novel azide and terminal acetylene functionalized aryl monomers **70**, **71** and **72** (shown in **Figure 17**) were designed and synthesized.

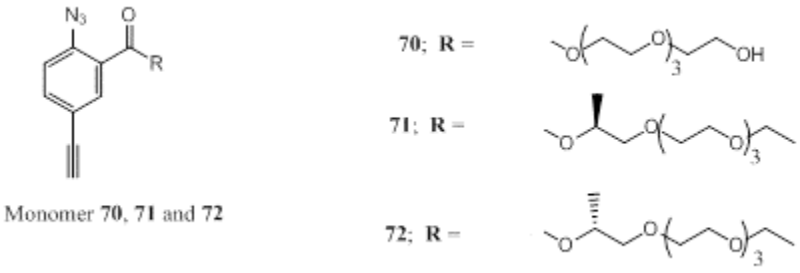

Figure 17: Proposed monomers for the synthesis of foldamers **2** and **3.**

3.2.1 Synthesis of chiral monomers 71 and 72

The azide-alkyne functionalized (*R*)- and (*S*)-aryl monomers **71** and **72** were synthesized in three steps. In the first step, the hydrophilic polyethylene glycol side chains **79** and **84** were prepared. These side chains were incorporated into the structures of the monomers to improve the solubility of the otherwise insoluble π-conjugated pPAT foldamers. The side chains also carry opposite chiralities intended to control, through conformational bias, the folding and the assembly processes at a later stage.

The required (*S*)-side chain **79** was prepared according to **Scheme 14**. Acid-catalyzed THP alcohol protection of the starting (*S*)-methyl lactate **73** afforded the THP-protected (*S*)-ester **74** which was reduced by $LiAlH_4$, under an inert atmosphere, to afford the THP-mono-protected alcohol **75** carrying a chiral centre. Nucleophilic substitution between the chiral alcohol **75** and tosylate **76** using NaH suspension in mineral oil, followed by the acid-catalyzed alcohol deprotection, afforded the required (*S*)-side chain **79**. The structure of this side chain was confirmed by ^1H NMR spectroscopy (Appendices; **Figure A1**) and mass spectrometry.

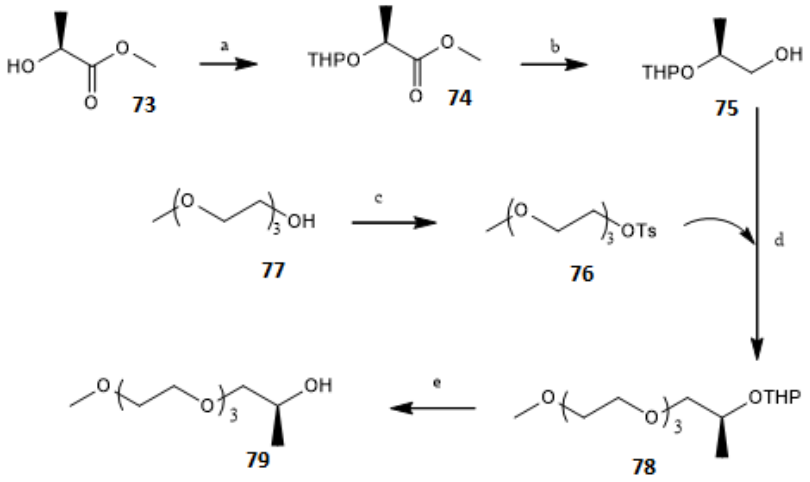

Scheme 14: Synthesis of (*S*)-chiral side chain a) DHP, H^+, neat; b) $LiAlH_4$, diethyl ether; c) *p*-TosCl, TEA, CH_2Cl_2; d) NaH, THF; e) *p*-TSA, MeOH.

Using the commercially available (*R*)-methyl lactate **80**, the required (*R*)-side chain **84** was prepared in the same manner as the (*S*)-side chain **79** according to **Scheme 15**.

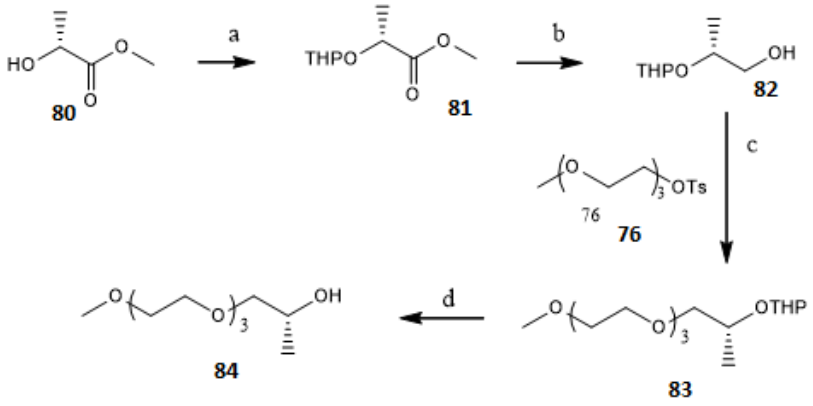

Scheme 15: Synthesis of (R)-chiral side chain a) DHP, H^+, neat; b) $LiAlH_4$, diethyl ether; c) NaH, THF; d) *p*-TSA, MeOH.

In the second step, the chiral side chains **79** and **84** were introduced to the azide-functionalized aryl acid **86** via esterification. The aryl azide **86** had earlier been prepared from azidation of the corresponding aryl amine **85** in an aqueous HCl and characterized by NMR spectroscopy (Appendices; **Figure A2**). Subsequently, the aryl acid **86** was coupled to the alcohols **79** and **84** under DMAP/DCC catalysis to afford esters **87** and **88,** respectively (**Scheme 16**). The structures of the aryl esters **87** and **88** were confirmed by NMR spectroscopy. For illustration, **Figure A3** in the Appendices shows the assignment of proton signals in the ^1H NMR spectrum of **88**.

The terminal alkyne positioned *para* to the azide was then introduced via its TMS-protected form. Palladium-catalyzed Sonogashira cross-coupling of the aryl iodides **87** and **88** with TMS-acetylene afforded the TMS-protected acetylene aryl azides **89** and **90**, respectively. Using a standard palladium-catalyzed Sonogashira cross-coupling procedure in this step, the reaction mixture was degassed to avoid oxidising of the palladium catalyst from oxidation state 0 (the active catalyst) to +2 (which impedes the reaction).

During this procedure, as expected, some of the aryl azides **89** and **90** were reduced to the corresponding amines **91** and **92** by the triphenylphosphine contained in the palladium catalyst. However, the amines were converted back to their corresponding azides using $TBNO_2$ and $TMSN_3$ (**Scheme 16**). The azides **89** and **90** were characterized by NMR and mass spectrometry. To illustrate, **Figure A4** (Appendices) shows the assignment of the proton signals on the ^1H NMR spectrum of TMS aryl azide **90**.

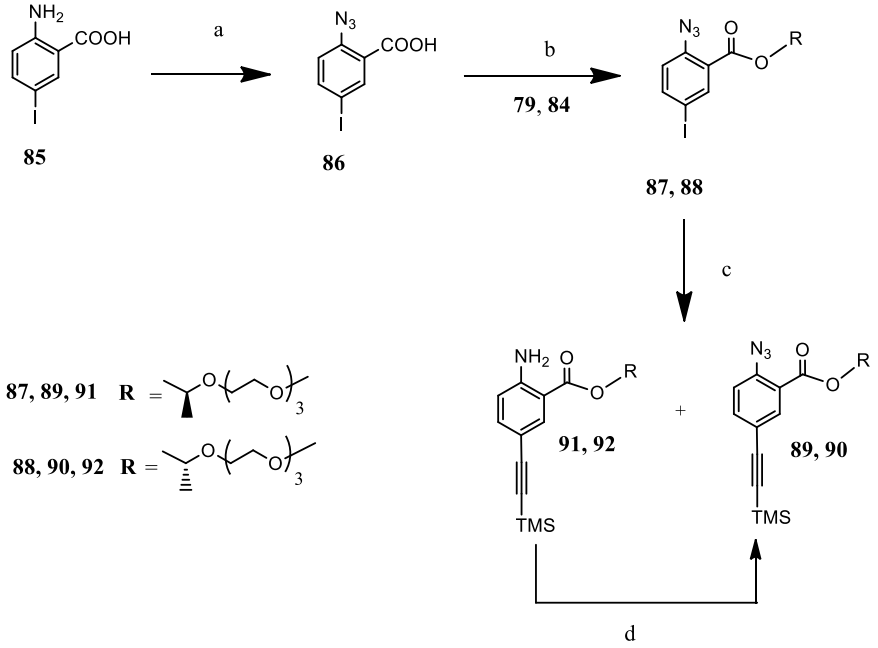

Scheme 16: Synthesis of TMS-protected aryl acetylene a) HCl, $NaNO_2$, NaN_3, 0 – 5^0 C; b) DMAP, DCC; c) TMSA, TEA, $PdPPh_3$; d) $TBNO_2$, $TMSN_3$.

Desilylation of the TMS-protected acetylenes of aryl azides **89** and **90** in the last step afforded the chiral monomers **71** and **72** as shown in **Scheme 17**. Desilylation protocols include the use of carbonates and fluorides. Carbonates are used under mild conditions in the presence of water, but longer reaction times and sometimes slightly elevated temperatures are required. However carbonates, being basic, can induce partial saponification among ester-rich substrates. Desilylation with fluorides is extremely fast and leads to complete conversion within a few minutes [14]. Since

our TMS-acetylene protected compounds contain esters, carbonate mediated desilylation was ruled out. Consequently, using TBAF in this reaction, fluoride-catalysed desilylation of aryl azides **89** and **90** afforded the required monomers **71** and **72**.

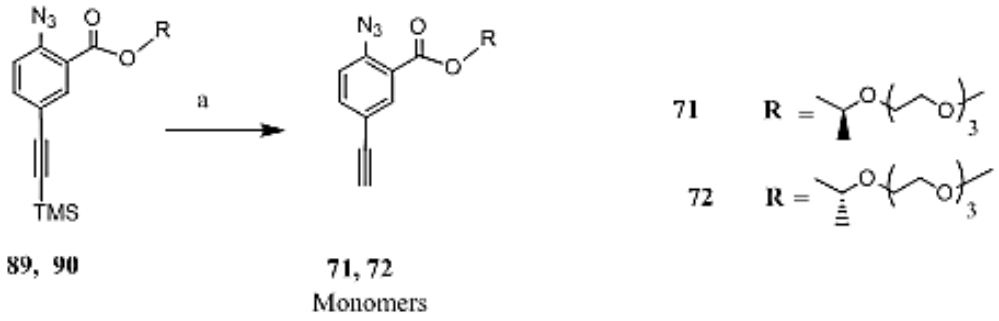

Scheme 17: Synthesis of monomers a) TBAF, THF, 0 – 5^0 C.

The chiral monomers **71** and **72** were characterized by NMR and mass spectrometry. Both monomers showed similar NMR and FTIR spectra. To illustrate, **Figure 18** shows the assignment of proton signals in the ^{1}H NMR spectrum of the (*S*)-chiral monomer **71**. Notably, the signal for the methyl group at the chiral centre is observed at 1.3 ppm as a doublet while the signal corresponding to the terminal methyl protons is observed at 3.37 ppm.

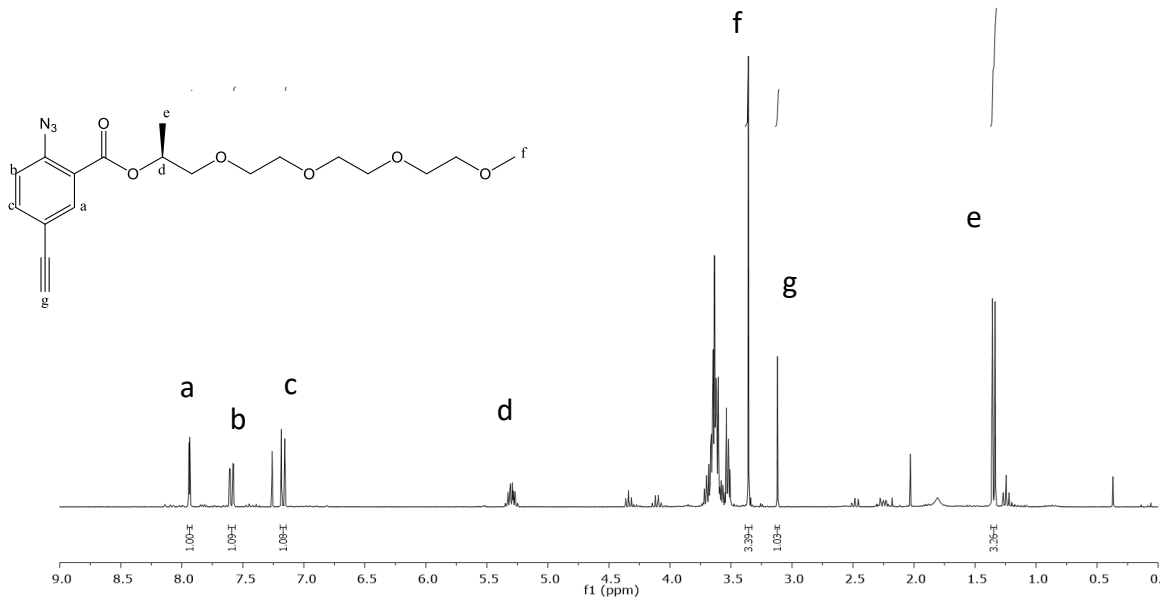

Figure 18: ^{1}H NMR spectrum of the chiral monomer **71.**

3.2.2 Synthesis of achiral monomer 70

Monomer **70** contains a terminal hydroxyl group (a) on its achiral side chain as shown in **Figure 19**. The idea behind the synthesis of monomer **70** was to use it in the functionalization of pPATs with hydroxyl groups. Copolymerizing monomer **70** with chiral monomers **71** and **72** to yield chiral pPATs with similar amounts of terminal hydroxyl groups as the amount of monomer **70** was the main idea behind this design. The hydroxyl groups would later be utilized for coupling the dyes to the pPATs during post polymerization labeling of the pPATs *via* DCC/DMAP-mediated esterification.

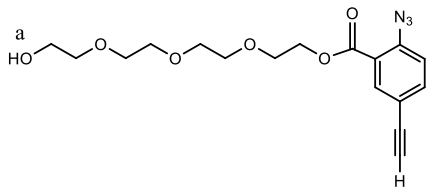

Figure 19: Monomer **70**.

The monomer was prepared from the commercially available tetraethylene glycol **93** (**Scheme 18**). Acid-catalyzed mono-protection of tetraethylene glycol afforded the mono-protected glycol **94**. Compared to THP, excess of tetraethylene glycol (> 2.5 equivalents) was used in this reaction to achieve mono-protection to 90%, which was determined by NMR and mass spectrometry. **Figure A5** (Appendices) shows the ^{1}H NMR spectrum for **94**.

Aryl acid **86** was then coupled to the THP-mono-protected glycol alcohol **94** via DCC coupling to afford aryl ester **95** followed by palladium-catalyzed cross-coupling of the aryl iodide with TMS-acetylene, under inert reaction conditions, to afford a mixture of TMS acetylene protected aryl azide **96** and amine **97**. The aryl ester **95**, TMS aryl azide **96** and the TMS aryl amine **97** were characterized by NMR and mass spectrometry. **Figures A6**, **A7** and **A8** in the Appendices show the assignment of proton signals on the ^{1}H NMR spectra for **95**, **96** and **97**, respectively.

The amine **97**, a by-product from the reduction of the azide group by triphenylphosphine during the palladium-catalyzed cross-coupling protocol, was successfully converted back to the corresponding azide **96** as shown in **Scheme 18**.

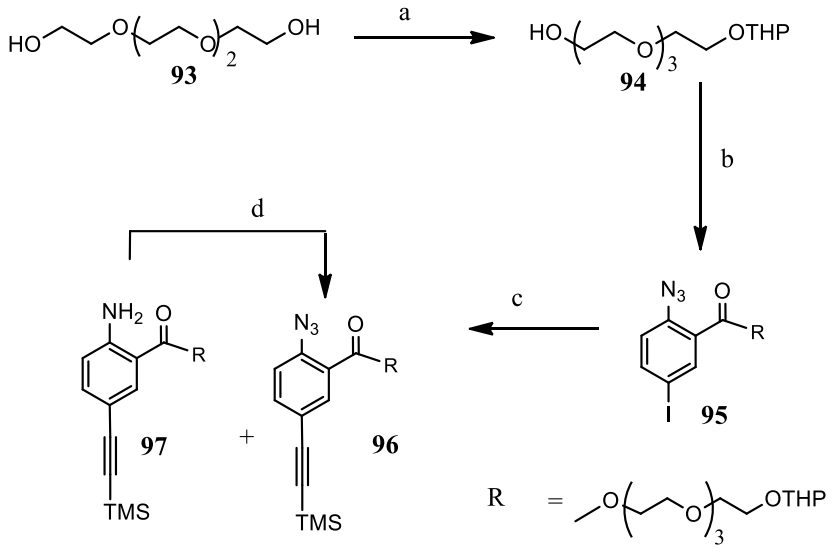

Scheme 18: Synthesis of the achiral TMS-protected acetylene aryl compound **97**; a) DHP, H^+, neat; b) DMAP, DCC; c) TMSA, TEA, $PdPPh_3$; d) $TBNO_2$, $TMSN_3$.

In the last step (Scheme **19**), acid-catalyzed THP deprotection of the side chain of aryl **96** to afford the TMS-protected aryl alcohol **98** (^{1}H NMR spectra shown in **Figure A9** in the Appendices) followed by TBAF-mediated desilylation afforded the required achiral monomer **70** in good yield.

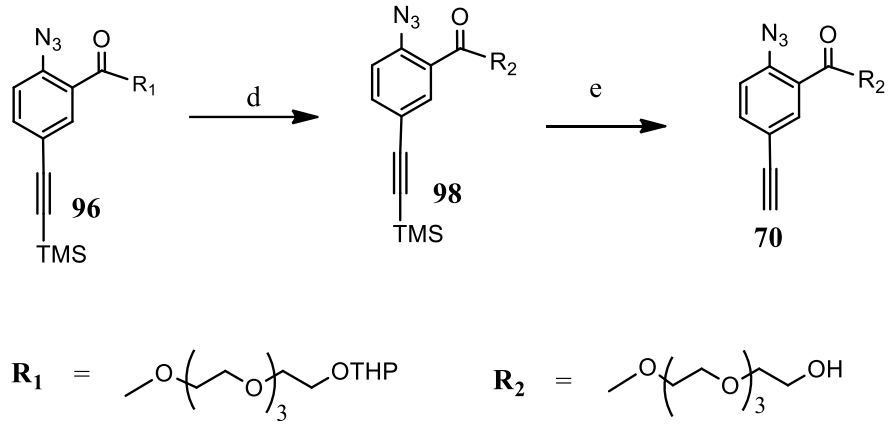

Scheme 19: Synthesis of achiral monomer **70**; d) PTSA, MeOH, r.t.; e) TBAF, THF, 0 – 5^0 C.

The achiral monomer **70** was characterized by NMR, FTIR and mass spectrometry. **Figure 20** below illustrates the assignment of proton signals in the ^{1}H NMR spectrum of monomer **70**. The terminal alkyne proton is observed at 3.02 ppm while the terminal hydroxyl group of the side chain is observed at 2.55 ppm.

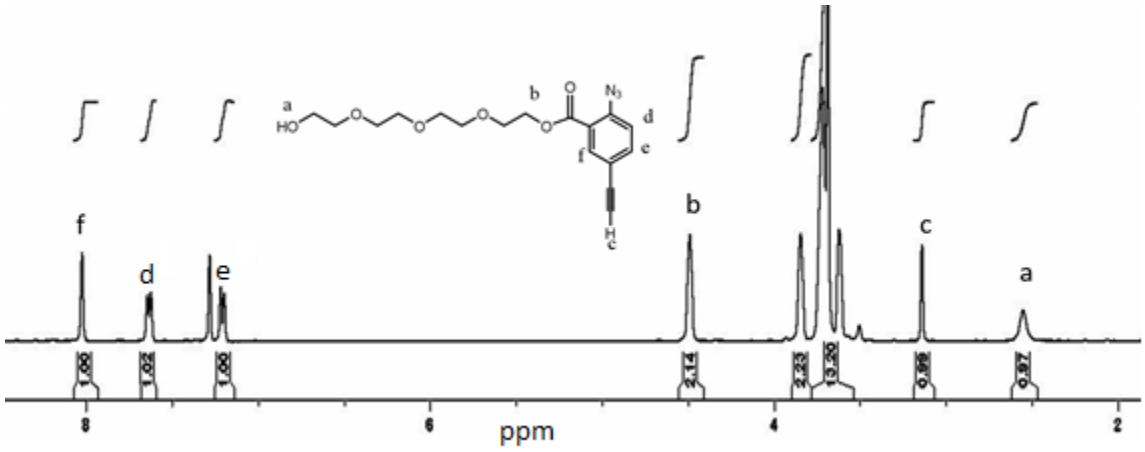

Figure 20: ^{1}H NMR for achiral monomer **70** in $CDCl_3$.

The FT-IR spectrum of the monomer **70** also shows the azide, aromatic C=C and –OH stretching frequencies at 2125 cm^{-1}, 1730 cm^{-1} and 3211 – 3699 cm^{-1} respectively, as shown in Figure **21**.

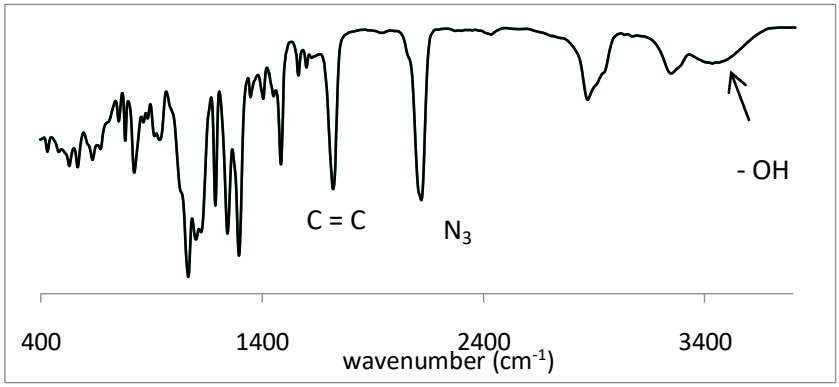

Figure 21: FT-IR spectrum for achiral monomer **70**.

3.3 Poly (aryl triazoles) synthesis: Step-growth click polymerization

The CuAAC mediated A-B step growth polyaddition (click reaction) has recently been utilized in the preparation of a wide range of functional polytriazoles due to its high conversion rate and mild reaction conditions [15, 16]. This reaction was utilized in this section to prepare three pPATs **99** and **100**, with embedded 'aryl-triazole' backbones, directly from the co-polymerization of the (*S*)- or (*R*)-chiral monomers **71** and **72**, respectively, with small amounts of achiral monomer **70** as shown in **Scheme 20**. The achiral monomer **70** affords pendant hydroxyl groups that were used for coupling the dyes to the polymers in the next stage during post-polymerization labeling as mentioned earlier.

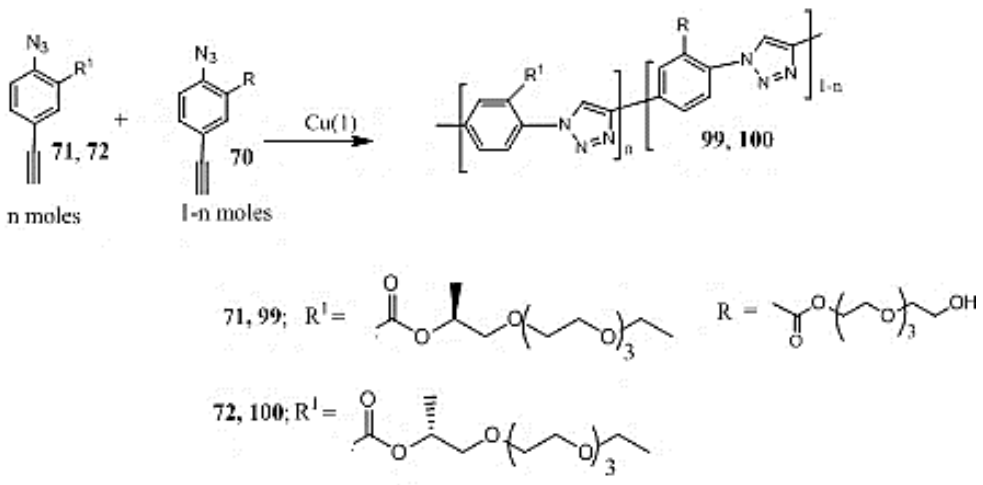

Scheme 20: Synthesized poly (*para*-aryltriazoles).

The utilized click procedure involved degassing of the reagents since the presence of oxygen could oxidize the catalytically important Cu(I) to Cu(II) with detrimental effect. After the reaction, the crude polymer was precipitated in aqueous EDTA solution, stirred and centrifuged at least four times to remove the Cu(I) species [21].

The pPATs were further purified by dialysis using dialysis tubing with molecular weight cut-off of 10 kDa for 24 h. Eliminating the short chains, this process afforded polymers of high molecular weight (above 20,000 Da) and large polydispersities (*Đ*) characteristic of polyaddition polymers as shown in **Table 1**.

Table 1: SEC results for the synthesis of pPATs

Entry	PAT	Initial % achiral monomer (feeding)	Final % achiral monomer (NMR)	M_n	M_w	*Đ*
1	**99**	0.5	0.4%	20991	82408	3.9
2	**100**	10	9%	18324	81016	4.4

The structures of the synthesized pPATs were confirmed by ^{1}H NMR and IR spectrometry. The pPATs exhibit similar NMR spectra. As an illustration, **Figure 22** shows the assignment of proton signals in the ^{1}H NMR spectrum for chiral pPAT **100** in $CDCl_3$. As expected, polymeric protons, compared to the monomers shown in **Figures 18** and **20**, are shifted downfield due to the deshielding effect of the triazole ring which is absent in the monomers. The characteristic triazole ring C-H proton ('c' in the Figure) is the most downfield shifted and is observed at 8.63 ppm. Close to the ester functionalities, the proton signal of the -CH_2 group (of the achiral side chain) appears at 4.48 ppm (signal 'a' in **Figure 22**) while the shift of the chiral center proton (from the chiral monomer) is observed at 5.26 ppm (signal 'b' in **Figure 22**). Integration of these two signals was used to calculate and confirm the amount of each of the two monomers **70** and **71** in the pPATs. These two signals 'a' and 'b' integrate in a 0.45:2.45 ratio which translates to 9% of the achiral monomer (**Figure 22**). The chiral side chain methyl protons' signal ('f' in the Figure **22**) is observed at 1.26 ppm. The ratio of the two monomers calculated for these integrals correlated with the monomers feeding mole ratio as shown in **Table 1.**

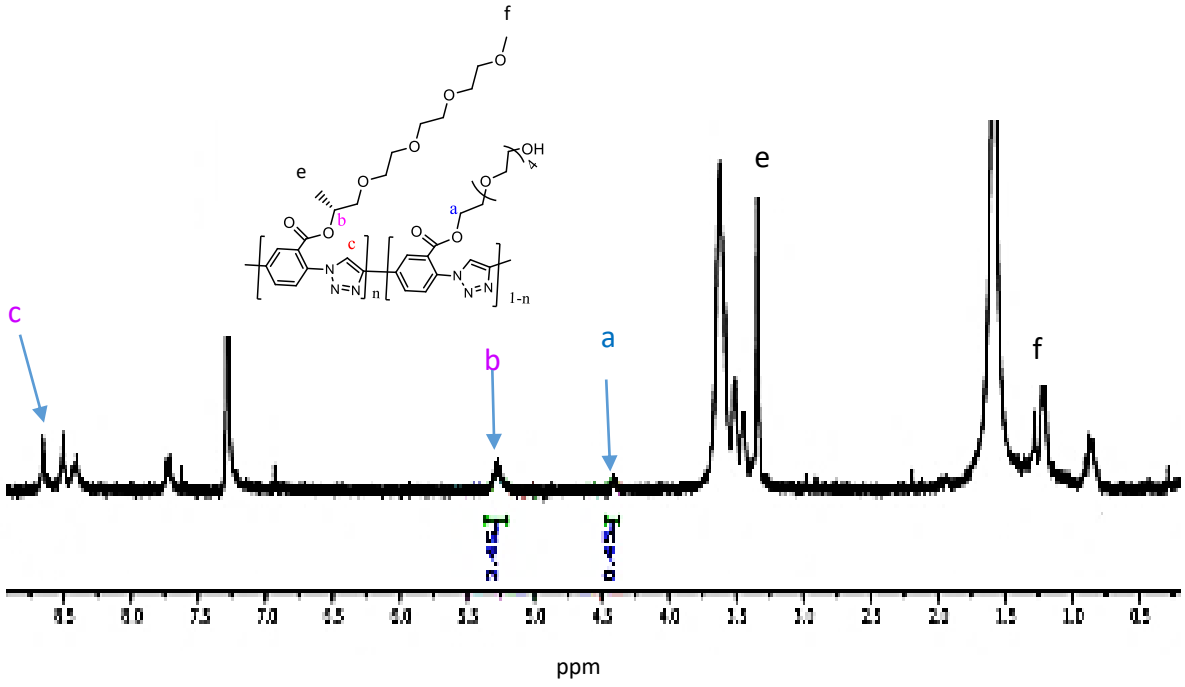

Figure 22: ^{1}H NMR spectrum for the chiral co-pPAT **100** containing 9% of the achiral monomer (**70**) in $CDCl_3$.

Although the sequence of the co-monomers in the chains of pPATs **99** and **100** could not be verified in this study, the ratio of the monomers in the pPAT chains determined from the integrals of the proton signals at 4.48 ppm (two protons) and 5.26 ppm (one proton) corresponding to the achiral and chiral monomers, respectively, in the ^{1}H NMR spectra of the pPATs is shown in **Table 1**.

Like NMR, the FT-IR spectra for the chiral pPATs were found to be similar. They both show the disappearance of the monomeric azide stretch frequency at 2100 cm^{-1} due to the formation of the triazole ring in the polymer. To illustrate, **Figure 23** shows the FT-IR overlay for the chiral pPAT **100** and its chiral monomer **71**.

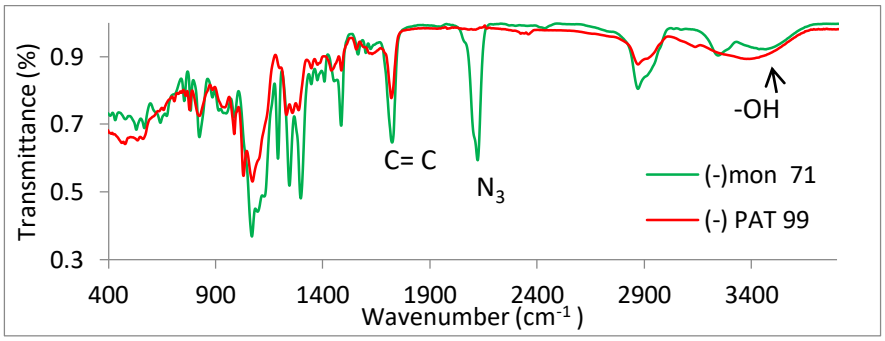

Figure 23: FT-IR overlay for the chiral pPAT **100** and its chiral monomer **71.**

3.4 Post-polymerization functionalization reactions: Labeling the polymers

3.4.1 Introduction

The development of efficient post-polymerization functionalization methodologies to install polymers with functional units is of major interest in macromolecular chemistry, particularly when the desired functionality is not compatible with either or both the polymerization conditions and monomer synthesis conditions [17, 18]. However, polymer modifications depend on efficient synthetic protocols that guarantee a nearly quantitative conversion of the polymer end or side groups with little or no formation of side products. Also, mild reaction conditions are desirable to avoid degradation of the polymer while the rate of conversion should be relatively high [18].

Visualization and tracking of our pPATs' helical folding process and/or interactions with a template under a confocal fluorescence microscope and electron microscope was one of the major aims of this work. To achieve this, it was necessary that the chiral polymers incorporate different and contrasting-colour fluorescent dyes in their structures. The fluorescent dyes used were the red rhodamine-based dye **101** and the green coumarin-based dye **102** for the (*S*)- and (*R*)-pPATs, respectively (**Figure 24**).

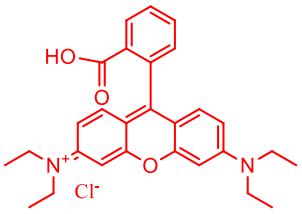

101

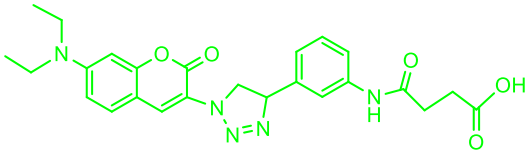

102

Figure 24: Rhodamine **101** and coumarin **102** dyes utilized in labeling the pPATs.

Incorporation of the rhodamine-based dye **101** in the monomer structures before they are polymerized was not possible. Since the dye is not compatible with the TBAF-catalysed desilylation step required for the monomers' synthesis protocol to afford the terminal acetylene. Desilylation of the TMS-protected and dye-functional monomer precursor **103** in the last step in our initial approach, synthesized according to **Scheme 22** with TBAF to afford the rhodamine-functionalized monomer **104**, failed due to a possible rearrangement of TMS-bearing ammonium salts upon introduction of TBAF [19]. A mixture of by-products that could not be identified was obtained.

The ^{1}H NMR spectra for aryl azide **98** (prepared according to **Scheme 19**) and dye-functional monomer precursor **103** are shown in **Figures A9** and **A10**, respectively, in the Appendices.

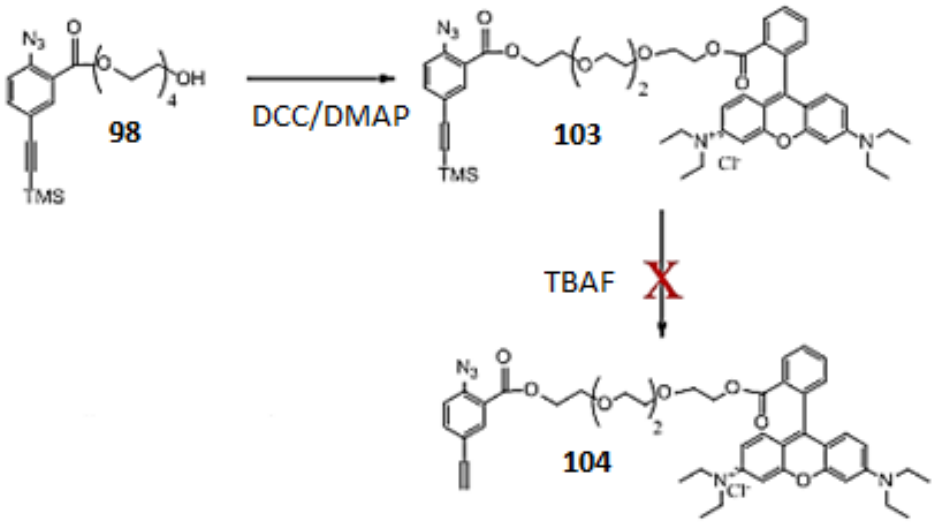

Scheme 22: Failed synthesis of monomer **104**.

Also, it was anticipated that the incorporation of the coumarin dye during monomer synthesis would yield a bulky molecule that would be challenging to purify. Following the incompatibility of the rhodamine dyes with the TBAF-catalyzed desilylation and the purification challenges for the coumarin dye functionalized monomer, post-polymerization labeling was done to functionalize the pPATs with dyes. In this way, we were able to label our pPATs with the desired coumarin- and rhodamine-based dyes while avoiding both the use of TBAF in a system containing the rhodamine dye and the purification challenges with the coumarin dye. Consequently, in our post polymerization labeling protocol, pPATs **99** and **100** incorporating –OH groups were first synthesized. The dyes were then introduced via DCC mediated coupling of the polymeric –OH groups and dyes' carboxylic acid groups.

3.4.2 Synthesis of the coumarin dye

While the rhodamine B dye **101** was acquired commercially, the coumarin dye **102** was synthesized from 4-diethylaminosalicylaldehyde **105** in three steps according to **Scheme 23** [20]. In the first

step, nitrocoumarin **107** was prepared from the condensation of 4-diethylamino salicylaldehyde **105** and ethyl nitroacetate **106** in butanol and acetic acid. Nitrocoumarin **107** was then reduced to amino coumarin **108** using $SnCl_2$ in HCl. In the second step, the azide group was introduced via the diazonium salt of the amino coumarin **108** to afford the azido coumarin derivative **109**. In the third and last step, CuAAC of the azido functionalized coumarin **109** and the terminal-acetylene-functionalized 4-(3-ethynylphenylcarbamoyl)-butyric acid **112** afforded the desired coumarin dye **102** [20].

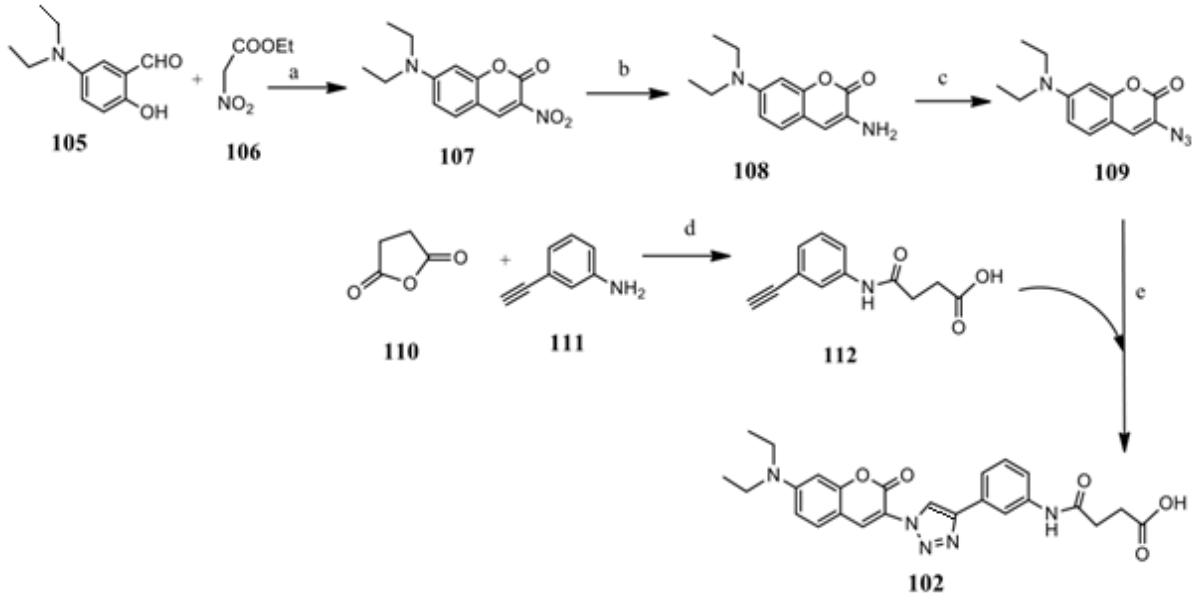

Scheme 23: Synthesis of coumarin dye **102**; a) piperidine, acetic acid, *n*-butanol b) $SnCl_2$, HCl, r.t. c) HCl, $NaNO_2$, NaN_3 d) dichloromethane e) THF, $CuSO_4$ 7.5% (1 M in water), sodium ascorbate 10% (1 M in water).

4-(3-Ethynyl-phenylcarbamoyl)butyric acid **112** was earlier prepared from the condensation of succinic anhydride **110** and 3-ethynylaniline **111**. The ^{1}H NMR spectra for compounds **107**, **108**, **109** and **112** are shown in **Figures A11**, **A12**, **A13** and **A14**, respectively, in the Appendices.

The coumarin-based dye **102** was characterized by NMR and mass spectrometry. **Figure 25** illustrates the assignment of selected proton signals in the ^{1}H NMR spectrum of the dye.

Conspicuously, the proton signal of the carboxylic acid hydroxyl group (a) is observed at 11.57 ppm while the proton signal of the triazole ring (b) is observed at 8.95 ppm.

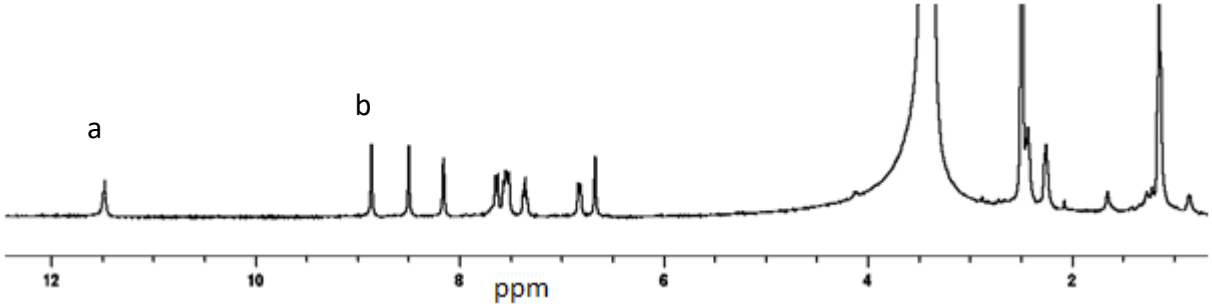

Figure 25: ^{1}H NMR spectrum of coumarin dye **102** in DMSO-d_6.

3.4.3 Labeling of chiral pPATs with dyes

The synthesized chiral pPATs **99** and **100** incorporating –OH groups in the side chains were functionalized with the rhodamine and coumarin dyes via DCC-mediated coupling, in DMF as shown in **Scheme 24**, to afford the labeled polymers **2** and **3**. The crude dye-functional polymers were precipitated from acetone, stirred for two hours and centrifuged to remove the unreacted dye and byproducts of esterification (urea). This process was repeated until the colors of the dyes were no longer visible.

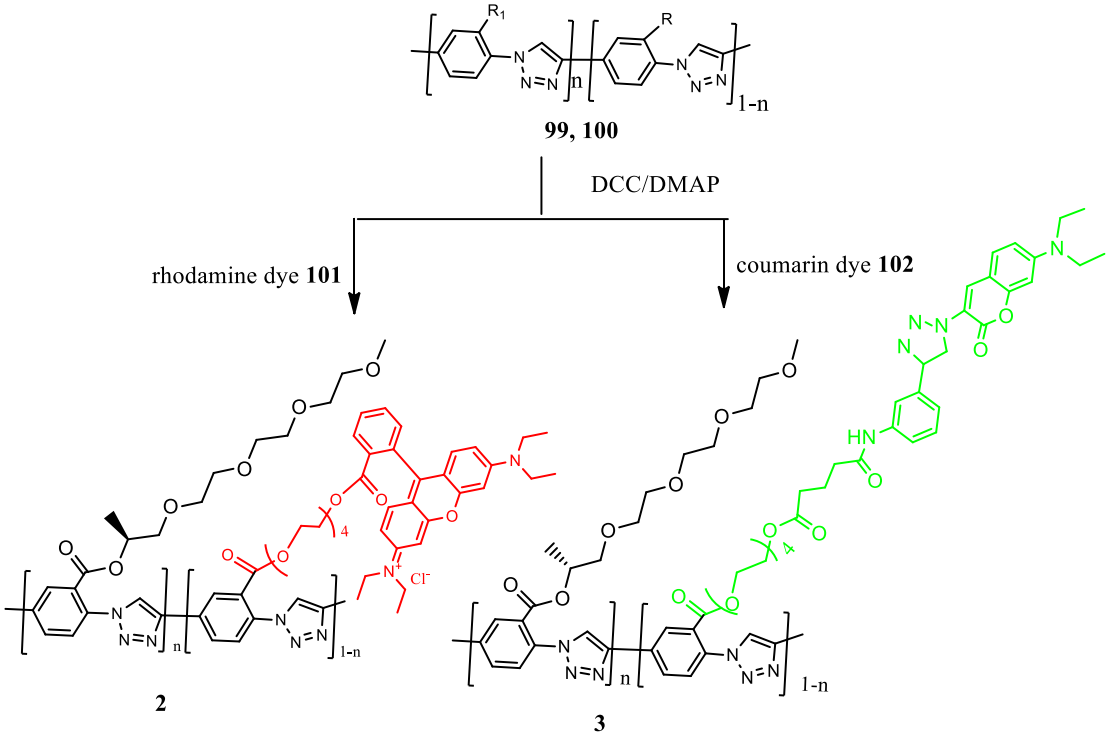

Scheme 24: Labeling the chiral pPATs **99** and **100** with dyes.

The structures of polymers **2** and **3** were confirmed by ^{1}H NMR and IR spectroscopy. **Figure 26** below illustrates the assignment of selected proton signals in the ^{1}H NMR spectrum for the rhodamine-functional pPAT **2**. Compared to the corresponding unlabeled pPAT **100**, the expected extra signals in the aromatic region (shown by the arrows) were attributed to the dye. However, the dye's terminal methyl (1.39 ppm) and their methylene protons (3.58 ppm) appear to overlap with the polymeric signals.

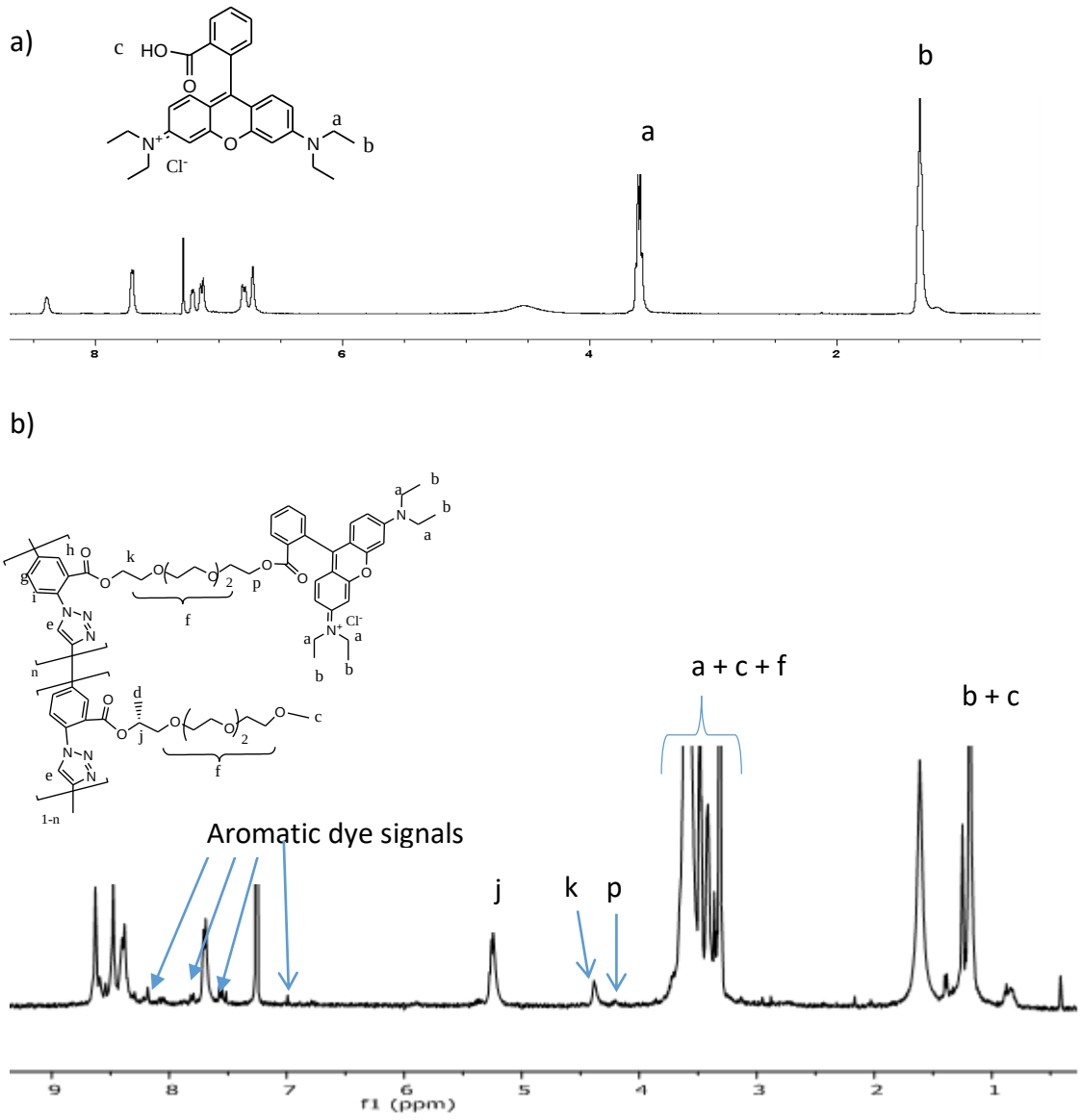

Figure 26: ^{1}H NMR spectra (a) for the rhodamine dye and (b) rhodamine-functionalized pPAT **2** in $CDCl_3$.

The FT-IR spectrum shows the disappearance of the –OH stretch frequency observed between 3200 and 5500 cm^{-1} for the pPAT **100** due to the esterification of the –OH group, as shown in **Figure 27** (an FT-IR overlay of the pPAT **100** and the labeled pPAT **2** spectra).

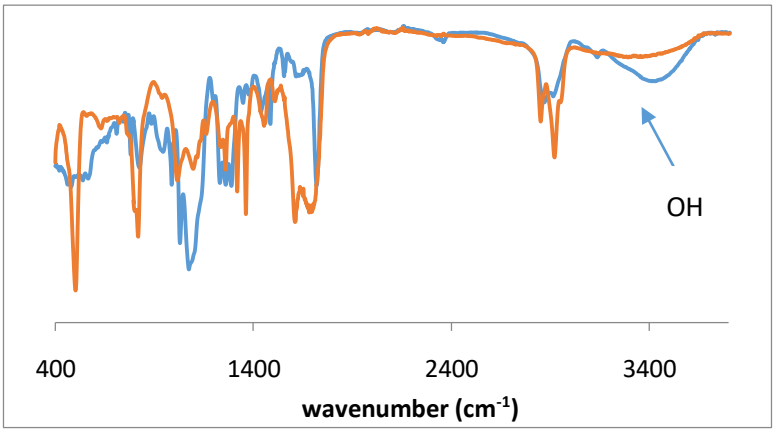

Figure 27: FT-IR overlay for pPAT **100** (blue) and the rhodamine-functionalized pPAT **2** (orange).

Figure 28 illustrates the assignment of proton signals in the ^{1}H NMR spectra for the coumarin-functional polymer **3** and the corresponding unlabeled pPAT **99**. Additional small signals in the aromatic region (shown by arrows) are attributed to presence of the small quantities of the coumarin-based dye (0.05%). Coumarin dyes are known to cluster [28], and a small amount was specifically used to avoid such clustering that could impair the organized interactions during the assembly of the double helices. The signals of the dye's methyl and methylene protons may overlap with the polymeric signals.

Similar to pPAT **2**, the FT-IR over-layed spectra for pPAT **99** and labeled pPAT **3** show the disappearance of the –OH stretch frequency observed between 3200 and 5500 cm^{-1} due to the formation of esters (**Figure A21** in the Appendices). ^{1}H NMR spectra for (above) pPAT **100** and rhodamine-functionalized pPAT **2** are shown in **Figure A19** in the Appendices.

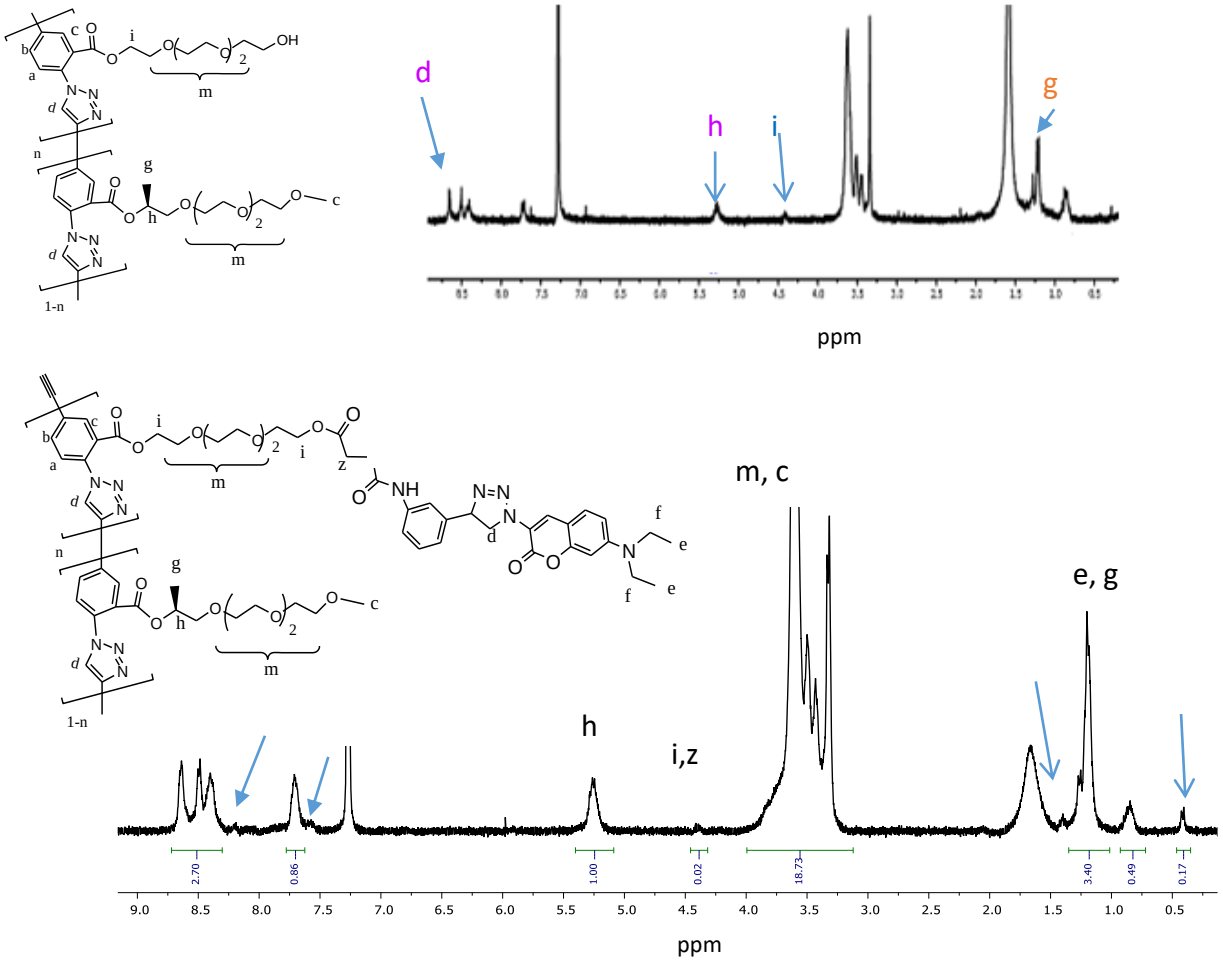

Figure 28: ^{1}H NMR spectra for (top) pPAT **99** and (bottom) coumarin-functionalized pPAT **3** in $CDCl_3$.

To further confirm the presence of the dyes, the labeled pPATs **2** and **3** were subjected to UV-Vis absorption. The spectra (**Figures 29a** and **b**) show the characteristic absorption signals for the coumarin and rhodamine dye at 410 nm and 552 nm, respectively.

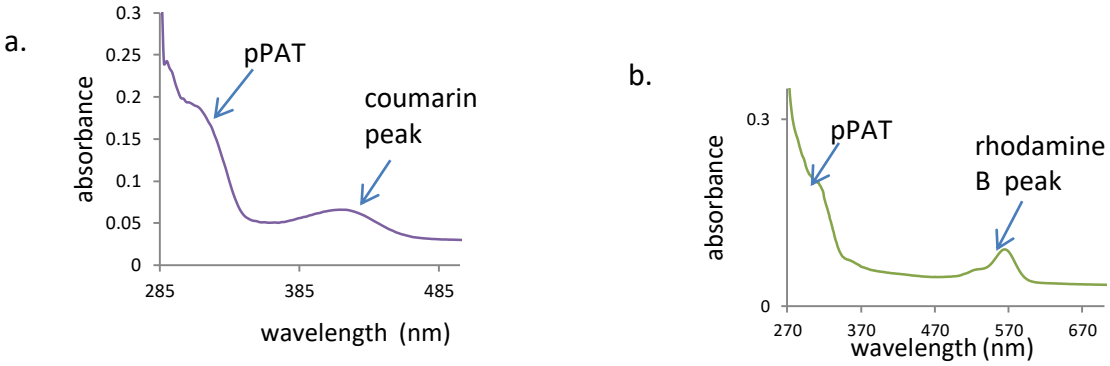

Figure 29: UV-Vis absorption curves of (a) chiral pPAT **2** and (b) chiral pPAT **3** at a concentration of 8.0×10^{-6} M at 25 °C.

3.5 Aggregation of poly(aryl triazoles) into double helical structures

In this section, the hierarchical assembly of labeled pPATs **2** and **3** is investigated. The helical folding processes from random coils into double helices, as a function of solvent quality and side chain chirality, are analyzed via elaborate UV-Vis and CD spectroscopic studies, TEM and the confocal fluorescence microscopy-based spatial distribution of the fluorescent signals. Previous studies have shown that helix-coil transitions can be driven by changes in solvent or temperature [21]. UV-Vis spectroscopy allows the detection of the presence of a helical conformation, while CD spectroscopy allows for the detection of the extent of any diastereomeric excess [21].

The pPATs **2** and **3** are analogous to the previously reported chiral polytriazoles, that show solvophobically-controlled hierarchical organization, which could be stabilized by hydrogen bonding and π-π stacking [21]. The chiral centre at the second carbon of the side chains from the backbone places the chiral stereochemical information in reasonably close proximity to the aromatic backbone, and is therefore able to bias the folding handedness of the resultant polymers and the incorporation of the dyes for the observation and tracking of the folding process under a confocal fluorescence microscope.

3.5.1 Insights and conditions for aggregation of polymers into ordered structures

For successful assembly studies, knowledge of the conditions for aggregation is important. Assembly of polymeric structures starts with a good solvent, correct concentration and temperature in which the monomeric polymers are molecularly dissolved and in which only random, disordered conformations exist. The hierarchical organization is induced by changes in solvent and temperature that encourage aggregation. With regards to π-conjugated systems, the poor solvents do not interfere with the internal π-π stacking and hydrogen bonds of the aryl backbone, which promotes aggregation [8 – 10].

In our assembly studies, DMF was selected as a ''good'' solvent while water was a "poor" solvent. Successful studies on these helices in these solvents have been reported [21]. Random disordered conformations were observed in DMF in which the pPATs are completely solvated while ordered, putative helical conformations were observed in water/DMF mixtures which poorly solvate the pPATs, leading to self-assembly, and eventually aggregation, with increasing water content.

3.5.2 Solvent-dependent formation of double helical structures

3.5.2.1 UV-Vis measurements for the chiral pPATs 2 and 3

The UV-Vis curves for the pPATs are bimodal. The first peak is observed at 282 nm corresponding to random coils while the second peak observed at 312 nm corresponds to the folded and interacting aromatic units as shown in **Figures 30** and **31** for pPAT **2**, and **Figure A15** in the Appendices for pPAT **3**). Their aggregation behavior was analyzed by following the changes in the absorption ratio of these two signals. This ratio has been extensively utilized to study the assembly behavior of many helical structures [21].

The hypochromic signal of pPATs **2** (**Figure 31**) and **3** at 282 nm in DMF is much stronger confirming the relatively good solubility of the pPATs, and thus neither folding nor transfer of chirality occurs in DMF. Also, no changes are observed in the absorption ratio of signals at 312 nm and 282 nm upon titration of 1 – 10% water, indicating that the pPATs still exist as random coils. Upon increasing the amount of water from 10 – 35%, a sharp increase in the 312/282 absorbance ratio was observed. This increase is presumably due to the organization of the pPATs into ''loose'' double helical bundles. In the literature, it has been shown that the addition of water initiates changes in the van der Waals forces and surface free energy, which facilitates the aggregation of the pPATs into strands which are ordered side by side [22, 23]. Once the strands are in this side by side alignment, they begin to twist into ''loosely'' wound double helical strands [22, 23, 27].

The 312/282 ratio does not change upon adding 35% – 40% water. This equilibrium region is suggestive of the existence of equal amounts of twisted strands (double helices) and untwisted strands which are still in side by side orientation. The equilibrium co-existence of the twisted and untwisted helical morphologies has been reported by Gruziel and Szymczac in their computational study of polymorphism in the aggregation of helical filaments [27].

The 312/282 ratio increases gradually upon adding 40% to 70% water. This increase is presumably caused by three scenarios. First is the organization of the remaining untwisted strands into the ''loosely'' wound double helices which is a very unstable state. Second, the ''loose'' helices release the internal stress to achieve more stable ''compact'' double helical morphology and a balance between the altered van der Waals forces and surface free energy [22, 23, 27]. Third, the ''compact'' double helices continue twisting further upon more water addition to afford tightly wound helices with ''tubular'' morphology. This morphological evolution is brought about by changes in surface energy and van der Waals forces created by variations in the solvent system.

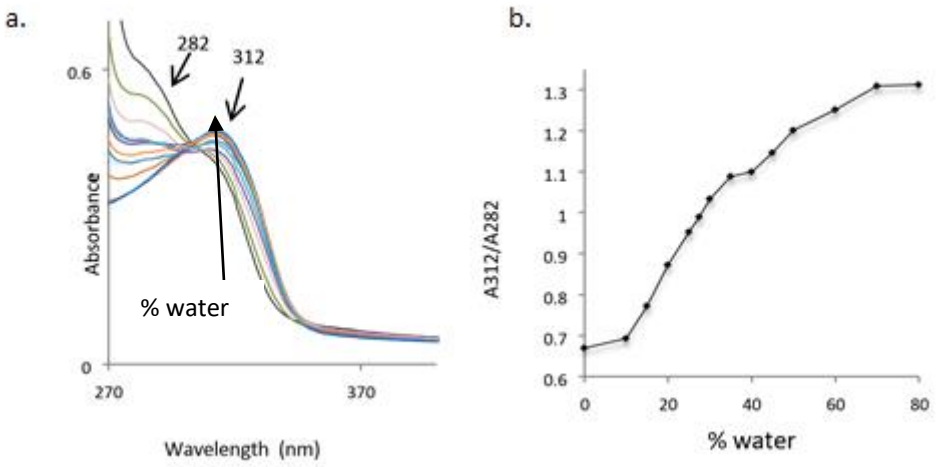

Figure 30: UV-Vis absorption curves of (a) chiral pPAT **2** and b) the corresponding Job's plot for the 312/282 absorption ratio upon titration of 10 – 80% water into the pPAT/DMF solution at a concentration of 8.0×10^{-6} M at 25 °C.

The 312/282 ratio remains constant upon addition of more than 70% water (**Figure 30**). This shows that the pPATs are fully organized into long and tight double helical strands with ''tubular'' morphology.

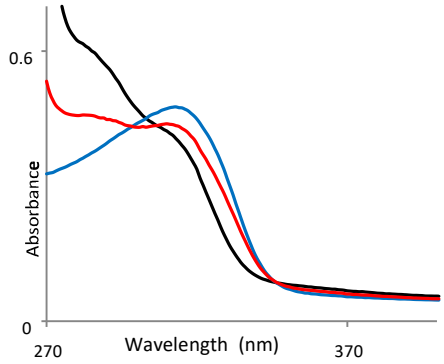

Figure 31: Selected UV-Vis absorption curves for chiral pPAT **2** after titration of 0% (black), 35% (red) and 70% (blue) water into the pPAT/DMF solution at a pPAT concentration of 8.0×10^{-6} M at 25 °C.

3.5.2.2 CD experiments: Confirmation of chirality-induced bias in the twist sense

To confirm the chirality-induced twist bias folding handedness and the presence of purely left- or right-handed double helical structures, the CD behavior of the chiral pPATs **2** and **3** in different DMF/water ratios was analyzed by tracking the Cotton effect (**Figure 32**).

In DMF and up to 10% water titration, no CD signal is observed for pPAT **2** as is expected for random coils that exist in this solvent system. This was also confirmed by the UV-Vis spectroscopic analysis (**Figure 31**). The onset of the negative Cotton effect is initiated when the fraction of water is about 10%. The signals at 312 nm increase sharply with an increase in the amount of water from 10 – 40% due to aggregation of pPATs with ''loose'' double-helical conformations being observed at 40% water fraction as will be shown later (**Figure 34**). Consistent with the UV-Vis analysis, a gradual decrease in the Cotton effect is observed when the fraction of water is increased from 40 – 80% as a result of the lateral interactions due to the assembly of more 'compact' double helices and ''tubular'' helices upon more twisting and release of internal stress to gain balance between changes in van der Waals forces and surface tension brought about by the addition of water into the system [22, 23].

pPAT **3** exhibits similar CD behavior as pPAT **2** but with an opposite Cotton effect due opposite folding handedness as shown in **Figure 32**. In DMF and up to 10% water titration, no CD signal is observed. The signal intensities at 321 nm increase sharply with an increasing amount of water from 10 – 40 % followed by a gradual decrease in the CD intensity upon titration of water from 40 – 80%.

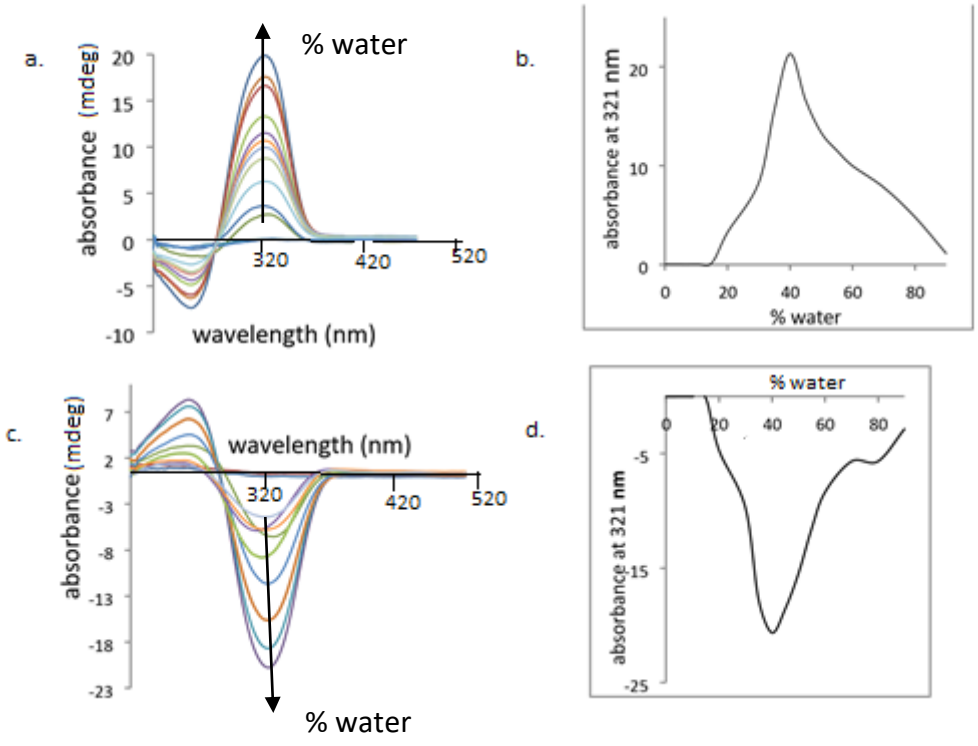

Figure 32: CD spectra for (a and c) pPATs **2** and **3** and (b and d) the corresponding job plots for the absorption at 321 nm upon titration with 10 – 80% water [conc. = 8.0×10^{-6} M at 25 °C].

3.5.2.3 Shifted isodichroic and isosbestic points

It is reported in the literature that lateral interactions of, for example, helical columns with each other to form multi-columnar architectures sometimes with an opposite overall CD effect is indicated by a shift or absence of an isodichroic point, and the inversion of chirality on the CD curves. This is due to changes in the structure of the helix which results in a modification of the exciton couple strength [24, 25].

While the CD spectra for our pPATs show twist sense bias in the folding handedness, no clear isodichroic point is observed on the CD spectra as shown in **Figure 33b** for pPAT **2**. This observation

may be due to lateral interactions that lead to twisting of the single strands to form double helices. However, no inversion of chirality is observed suggesting that the double helices are formed from one-handed twisted strands as illustrated later in **Figure 38**.

Despite showing changes in the peaks at 282 nm and 312 nm on the UV-Vis spectrum due to hierarchical organization, more evidence for lateral interactions that affords double helical structures would be the unclear isosbestic point (**Figure 33a**). Information on the changes at this point with regards to lateral interactions during assembly could not be found in the literature.

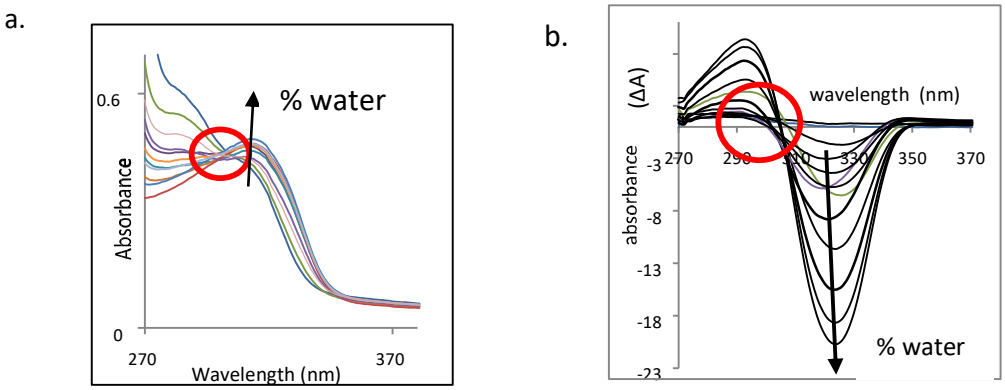

Figure 33: (a) UV-Vis and (b) CD curves of pPATs **2** upon titration of 10 – 80 % water showing shifts in isosbestic and isodichroic points at a concentration of 8.0×10^{-6} M at 25 °C.

3.5.3 Transmission electron microscopy (TEM) and fluorescent image analysis

To obtain visual evidence for the formation of the helical structures, scanning TEM (STEM) and fluorescence imaging were carried out on selected samples of pPATs **2** and **3**. For pPAT **2**, samples were prepared using 10% water (onset of folding), 40% water (equilibrium), and 60% water (when the double helical structures are expected to have been fully assembled) and 80% water (for the expected tubular structures) fractions as shown in **Figure 34**.

For samples with 10% water, no morphologies were observed on both STEM and fluorescent images as expected.

STEM samples prepared using a 40% water fraction showed ‘’loosely’’ wound double helical bundles (**Figure 34**). This strongly suggests the onset of double helix formation consistent with UV-Vis and CD analyses. Fluorescence images for this sample reveal the existence of ‘loose’ double helices of up to 10 micrometers in length and 200 nm in diameter.

Defined architectures with clear ‘’compact’’ double helical morphologies were observed on both STEM and fluorescence images for samples prepared with 60% water (**Figure 34**). Long double helices of more than 10 micrometers in length and 200 nm in diameter were observed. The significant length of the double helices observed suggest stacking of the short double helices.

STEM samples prepared from 80% water showed ‘’tubular’’ morphology (**Figure 34**). This morphology is a result of tightly wound double helical bundles. Fluorescence STEM images for this sample revealed the existence of ‘’tubular’’- or ‘’rod’’- like structures of up to 10 micrometers in length and 140 nm in diameter, with no clear pitches and turns due to tight twisting of the helices.

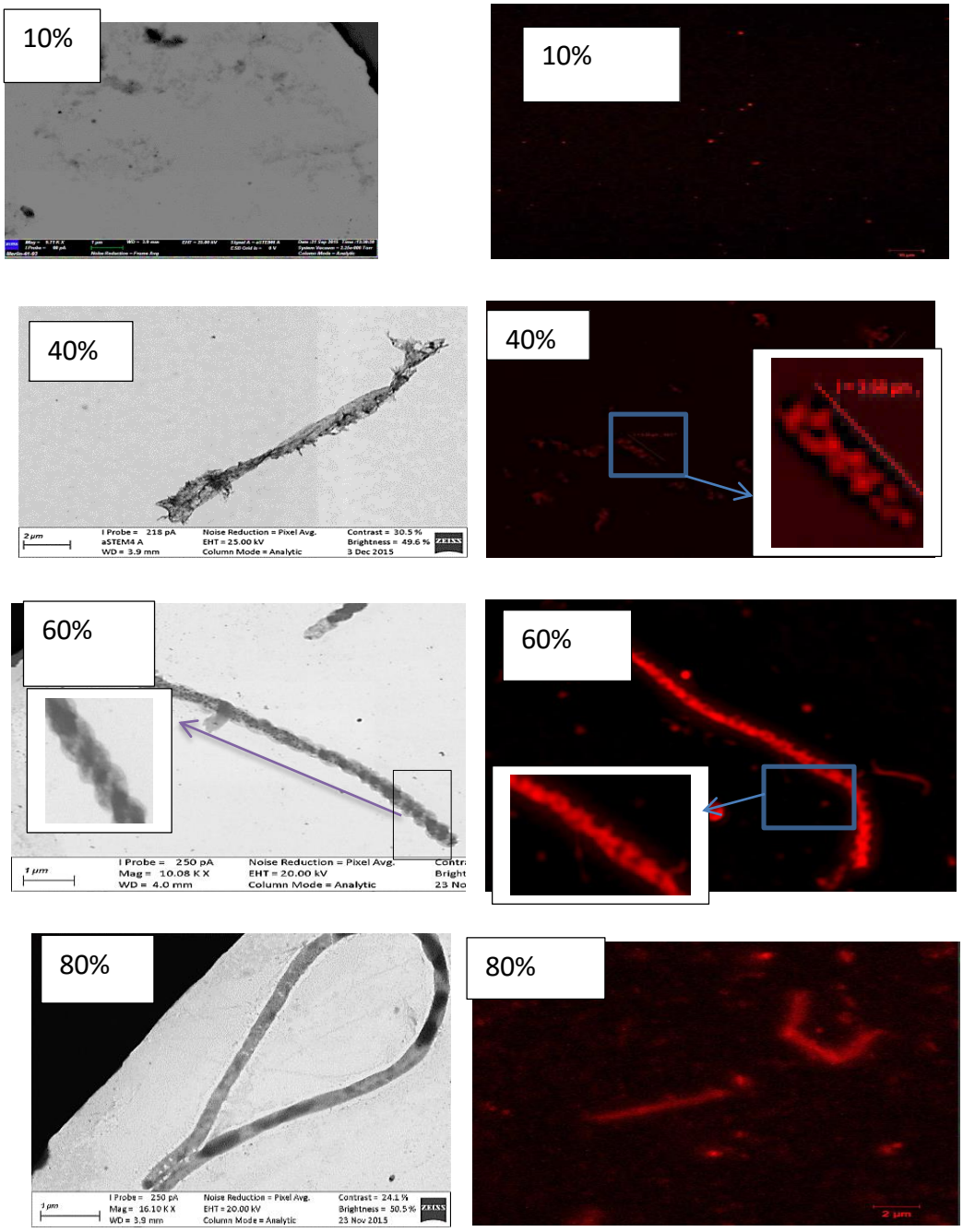

Figure 34: STEM and fluorescent images for pPAT **2** with 10%, 40%, 60% and 80% water at a concentration of 8.0×10^{-6} M at 25 °C.

Attempts to obtain fluorescent images with clear resolution were unsuccessful for the coumarin-functionalized pPAT **3**. The dye bleaches rapidly to give poor and blurred images when observed under confocal fluorescence microscopy [28]. However, STEM analysis of coumarin-functionalized

pPAT **3** confirmed the formation of helices with similar morphology as the ones observed on the rhodamine-functionalized pPAT **2** as shown in **Figure 35**. At 0.5% coumarin dye content, the images taken at 60% water show ''blurred'' rods. The morphology of these rods was confirmed by STEM. Defined architectures with clear ''compact'' double helical morphologies of more than 10 micrometers in length and 270 nm diameter are observed on STEM. At 80% water, fluorescence images reveal the existence of ''tubular''- or ''rod''-like structures of up to 8 micrometers in length and 200 nm in diameter. The STEM image does not show clear pitches and turns due to tight twisting of the helices. Again, as earlier explained, the tight twisting leads to the reduction of the diameter and length.

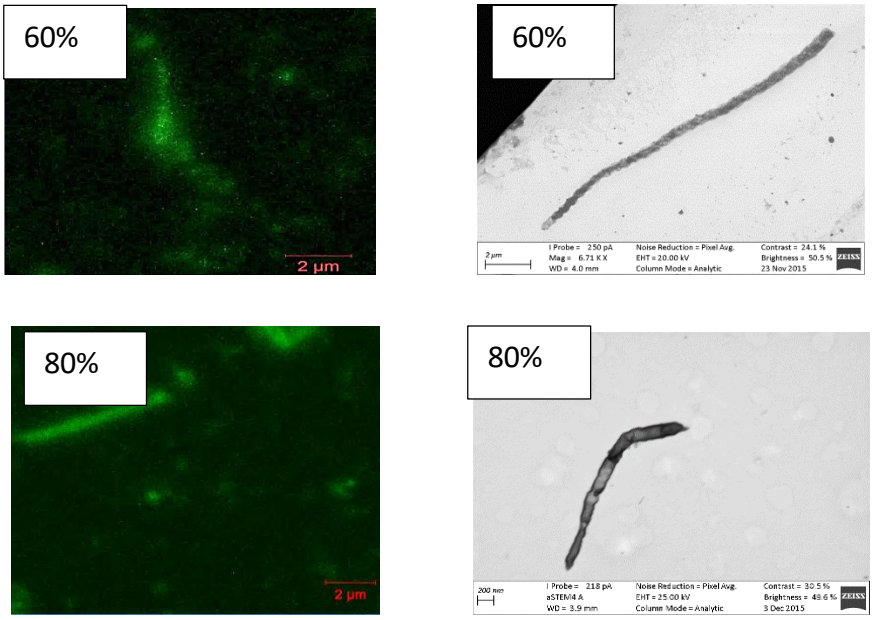

Figure 35: Clustered STEM and fluorescent images for coumarin-labeled pPAT **3** with 60% and 80% water at a concentration of 8.0×10^{-6} M at 25 °C.

3.5.4 Types of handedness of the double helices

Having confirmed the formation of double helices, we endeavored to analyse their handedness. As discussed earlier, shifts in the isodichroic and isosbestic points are observed on the CD and UV-Vis titration curves of pPATs **2** and **3** due to lateral interactions of the single strands to form and stack the double helices into long strands. However, no inversion of chirality is observed for the CD spectra of pPATs **2** and **3** suggesting that the double helices are formed from the intertwining of one-handed single strands (shown later in **Figure 38b** and **c**).

The ability of the pPATs to form double helices from the intertwining of different handed single strands and/or stacking of helices of different handedness in a random order was investigated by subjecting a mixture of the left-handed green pPAT **3** and the right-handed red pPAT **2** in equal concentration to UV-Vis, CD and fluorescence microscopy as shown in **Figure 36**.

The mixture exhibited normal UV-Vis behavior similar to the individual pPATs **2** and **3**. No change was observed up to 10% water addition. Upon titration of 10 – 35% water into the pPAT solutions in DMF, a gradual increase of the hyperchromic signals at 312 nm and the 312/282 absorption ratio is observed, which indicates the formation of helices. On adding 35 – 40% water, the 312/282 ratio remains constant. This equilibrium point is indicative of the existence of equal amounts of random coils and double helices. On increasing the amount of water from 40 – 70%, the hyperchromic signal at 312 nm decreases slowly as the 312/282 absorption ratio increases at the same rate. No more change is observed in the 312/282 absorption ratio upon increasing the amount of water above 70%. This is because the pPATs exist in 'tightly wound' double helical conformations and are stacked.

However, the CD spectra for the red and green pPATs mixture showed no Cotton effect as expected due to presence of the pPATs **2** and **3** with opposite chirality (**Figure 36b**).

Conclusively, the UV-Vis and CD results suggested the formation of double helices via intertwining of different handed strands and/or stacking of double helices of different handedness in a random order.

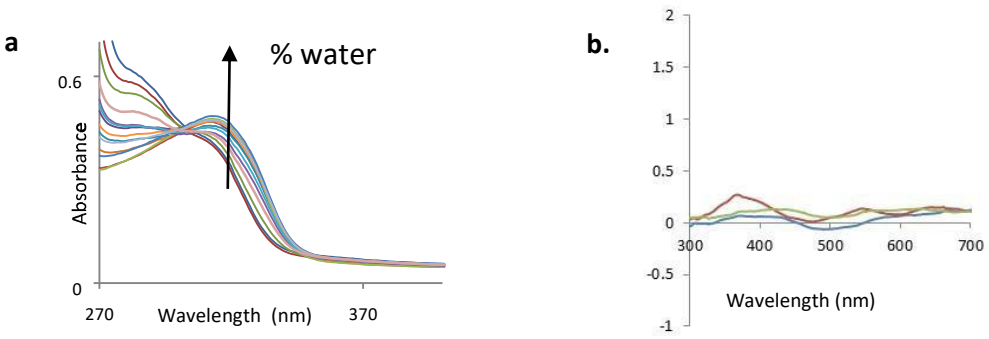

Figure 36: (a) UV-Vis curves of the pPATs **2** and **3** mixture upon titration of 10 – 80% water showing shifts and (b) CD curves upon titration of 10%, 40% and 70% water at a concentration of 8.0×10^{-6} M at 25 ^{o}C.

Further, this mixture of the red and green pPATs at 70% water fraction was subjected to fluorescence imaging experiments. This was performed to confirm the formation of double helices from the intertwining of different handed single strands and/or stacking of double helices of different handedness. The 70% water fraction was chosen because at this point the helices are fully formed and stacked. The images were taken on the same scale for the red region (**37a**), the green (**37a**) region and full-range region (**37c**) as shown in **Figure 37**.

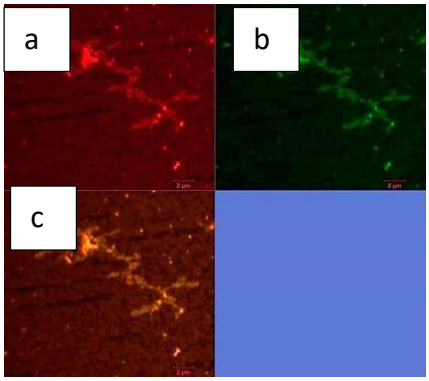

Figure 37: Fluorescent image for the rhodamine- and coumarin-functional pPATs **2** and **3** mixture at 70% water content at a concentration of 8.0×10^{-6} M at 25 ^{o}C.

Although, the image quality is low, both green and red helices could be seen at the exact same location on the images while the full spectral range image had its color between red and green (**Figure 37c**). This strongly suggests the formation of a double helix via intertwining of different handed strands as shown in **Figure 38a**. However, no evidence was observed for the stacking of different handed helices in these experiments (**Figure 38d**).

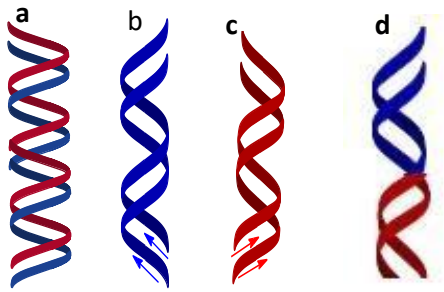

Figure 38: Different types of double helices; (a) a double helix made of twisted opposite-handed single strands, (b) double helix made of twisted left-handed strands, (c) a double helix made of twisted right-handed strands and (d) stacking of different handed helices which was not observed.

3.6 Mechanism for the formation of the double helix

Analysis of STEM images, fluorescent images, and UV-Vis and CD titration curves revealed the organization of our pPATs from random coils into double helical super structures. While the large diameter of the double helical assemblies (more than 150 nm) indicated that it is not a single strand but bundles consisting of many individual strands that twist to form the double helical super structures, studies on the assembly of related pPATs reported by Pfukwa and co-workers show that the pPATs' single strands organize into helices which cluster into bundles which stabilize when 80% water has been added into the pPATs solutions in DMF [21].

We therefore speculate that the formation of the double helical nanostructures observed in this work follows a two-process-mechanism. Firstly, the pPATs single strands organize into helices which may also stack into helical columns upon changes in solvent quality achieved through addition of water into the pPATs/DMF solutions. This process for the formation of single strand

helices, reported to occur upon slow addition of water, happened so fast that it eluded our experimental capture. Only clustered helical bundles were observed after 30 – 40% water had been titrated.

Secondly, the clustered helical bundles organize into double helices. According to Shaomin Zhou and co-workers who have reported the assembly of double helix micro fibrils from achiral helical columns, a combination of π-interactions and the temperature-driven changes in the van der Waals forces and surface free energy among adjacent helical bundles as the primary driving force for the formation of double-helical structures of approximately 200 nm in diameter, a pitch of 150 nm and an extended length of several micrometers [26]. In our case, increasing the amount water into our pPATs' solutions in DMF, solvent driven-changes in van der Waal forces and surface free energy facilitates the side by side arrangement of the pPATs' helical bundles [22, 23, 26, and 27]. Once these pPATs' bundles of helical columns are in this side by side arrangement, adjacent bundles coil on one another or twist into double helices and release internal stress to achieve a more stable compact morphology and a balance between the altered van der Waals force and surface free energy.

Loose double helices are observed after 40% water has been titrated into the pPATs solutions in DMF as shown earlier in **Figure 34**. The helices either stack onto one another to form long stacks which continue to twist into the tubular structures or first twist further into small tubules which then stack into long tubular structures, as shown in **Figure 39** for the suggested mechanism followed during the assembly of the observed double helical nanostructures.

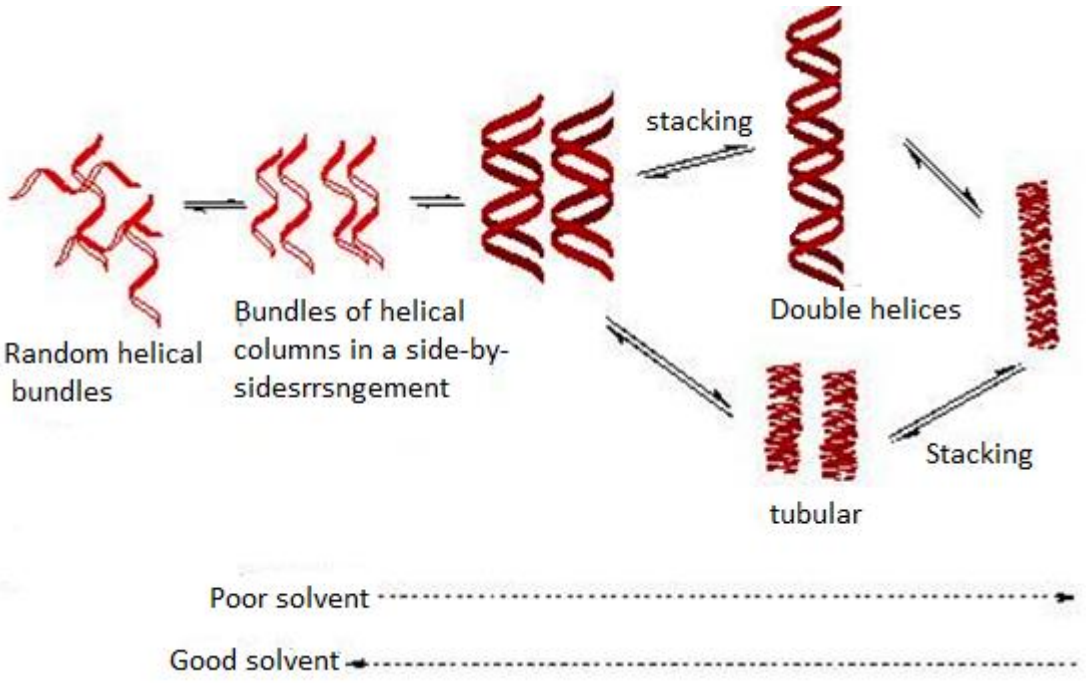

Figure 39: Suggested mechanism for the formation of double helical super structures.

3.7 Conclusions

A double helical assembly system based on poly(*para*-aryl triazole)s (pPATs) has been developed. The conformational preferences of the foldamers were controlled by adjusting the fraction of water (a poor solvent) in DMF (a good solvent) and tracked by a combination of UV-Vis and CD, STEM and fluorescence imaging spectroscopy. CD Spectroscopic analysis was possible by the addition of chiral side chains to the pPAT backbone, which biased the screw sense of the helix. Careful analysis of UV-Vis and CD signals, STEM and fluorescence images allowed a hierarchical self-assembly pathway of the double helix to be proposed.

The pPATs first formed ''loose'' double helical bundles directly from the helical bundles in a side by side alignment. With increasing solvophobic driving force and changes in the van der Waals forces and surface free energy, the 'loose' double helices further twisted first into 'compact' and stable

double helices with a diameter of 200 nm, a pitch of 200 nm and a length of up 20 micrometers and, second, into ''tubular'' conformations of 150 nm diameter and of up 20 micrometers in length.

The shift of both isodichroic and isosbestic points on the UV-Vis and CD spectra, respectively, upon increasing the amount of water provided strong evidence for the formation of double helical morphology.

3.8 Experimental

3.8.1 General details

All starting materials and solvents were purchased from Sigma Aldrich or Merck and used as received without further purification unless stated. ^{1}H NMR and ^{13}C NMR spectra were recorded on a Bruker Avance DPX 400 or Oxford Origin NMR spectrometers. NMR samples were prepared in deuterated solvents ($CDCl_3$ or DMSO-d_6) purchased from Sigma Aldrich or Merck. The samples were run at room temperature. Coupling constants (J) are given in Hz, while chemical shifts are expressed in parts per million (ppm) using TMS as internal reference.

FT-IR spectra were recorded on a Bruker TENSOR 27 FT-IR spectrometer. Column chromatography was performed using silica gel (particle size 0.040-0.063 mm) purchased from Merck while thin layer chromatography (TLC) analyses were performed on pre-coated silica gel 60 F_{254} aluminum sheets (0.063 - 0.2 mm/70 - 230 mesh) purchased from Merck and compounds detected by observation under UV light and/or exposure to iodine vapour.

TLC SnakeSkin® Pleated dialysis tubing, MW cut off 10 000 Da, was purchased from Thermoscientific. SEC experiments were performed in DMAc at 40 ^{o}C and a flow rate of 0.5 mL/min, using a system equipped with a Waters 410 differential refractometer and PL Gel mixed C column (internal diameter 7.8 mm, length 30 cm). Number average molecular weights (M_n) were calculated using calibration curves obtained from PMMA standards.

STEM samples [1 µM] (2 µL) were pipetted onto carbon coated 200 mesh copper grids, vacuum dried and then viewed using a JEOL 1200 – EX II TEM at 120 kV. Images were collected using a Proscan CCD camera.

UV-Vis measurements were carried out on a Perkin Elmer Lambda 20 photodiode array spectrophotometer in 1 cm quartz cuvettes while CD measurements were made on a Jasco J-815 instrument in 1 cm quartz cuvettes. UV-Vis and CD titration samples (in µM concentration range) were prepared volumetrically, by mixing a fixed volume of pPAT from the same stock solution, with the appropriate volume of water and/or DMF up to a constant total volume. These experiments were carried out at 22 °C, unless stated otherwise.

Fluorescence imaging samples [1 µM] (2 µL) samples were pipetted on to glass plates then viewed using a ZEN 2011 [Carl Zeiss (Germany)] confocal microscope. Images were collected using an Andor EMCCD IXon DU 885 camera.

3.8.2 Synthesis of chiral monomers

Compounds **71** to **90** were synthesized according to procedures available in the literature [21] and their structures confirmed by NMR.

3.8.2.1 Methyl (2*S*)-2-(tetrahydro-2H-pyran-2-yloxy)propanoate 74: ^{1}H NMR (400 MHz, $CDCl_3$) δ: δ 4.69– 4.65 (m, 2H), 4.40 (q, *J* = 7.0 Hz, 1H), 4.19 (q, *J* = 6.8 Hz, 1H), 3.94 – 3.74 (m, 2H), 3.711 (s, 3H), 3.707 (s, 3H), 3.54 – 3.38 (m, 2H), 1.91 – 1.46 (m, 12H), 1.43 (d, *J* = 6.9 Hz, 3H), 1.37 (d, *J* = 6.9 Hz, 3H). ^{13}C NMR (100 MHz, $CDCl_3$) δ: 173.92, 173.81, 98.41, 97.73, 72.49, 70.07, 62.57, 62.55, 52.02, 52.00, 30.57, 30.48, 25.47, 25.36, 19.31, 19.27, 18.92, 18.12.

3.8.2.2 (2*S*)-2-(Tetrahydro-2H-pyran-2-yloxy)propan-1-ol 75: ^{1}H NMR (400 MHz, $CDCl_3$) δ: 4.70 (dd, *J* = 5.1, 2.7 Hz, 1H), 4.52 (dd, *J* = 6.3, 2.6 Hz, 1H), 4.01 – 3.72 (m, 4H), 3.69 – 3.37 (m, 6H), 1.87 – 1.64 (m, 5H), 1.61 – 1.43 (m, 8H), 1.18 (d, *J* = 6.4 Hz, 3H), 1.10 (d, *J* = 6.5 Hz, 3H). ^{13}C NMR (100 MHz,

$CDCl_3$) δ: 99.99, 99.14, 77.75, 74.96, 67.27, 66.25, 64.64, 63.24, 31.67, 31.17, 25.44, 25.18, 21.00, 20.14, 17.81, 17.29.

3.8.2.3 2-[2-(2-Methoxy-ethoxy)-ethoxy]-ethyl *p*-tosylate 76: ^{1}H NMR (400 MHz, $CDCl_3$) δ: 7.78 (d, *J* = 7.33 Hz, 2H), 7.33 (d, *J* = 7.9 Hz, 2H), 4.16 – 4.13 (m, 2H), 3.69 – 3.66 (m, 2H), 3.61 – 3.56 (m, 6H), 3.53 – 3.50 (m, 2H), 3.35 (s, 3H) 2.43 (s, 3H). ^{13}C NMR (100 MHz, $CDCl_3$) δ: 144.89, 133.12, 129.91, 128.07, 72.00, 70.84, 70.66, 70.64, 69.34, 68.77, 59.13, 21.74.

3.8.2.4 (13*S*)-2,5,8,11-Tetraoxatetradecan-13-ol 79: ^{1}H NMR (400 MHz, $CDCl_3$) δ: 3.99 – 3.90 (m, 1H), 3.69 – 3.61 (m, 10H), 3.55 – 3.51 (m, 2H), 3.47 (dd, *J* = 9.9, 3.0 Hz, 1H) 3.36 (s, 3H), 3.24 (dd, *J* = 9.9, 8.4 Hz, 1H), 2.90 (s, 1H), 1.10 (d, *J* = 6.4 Hz, 3H). ^{13}C NMR (100 MHz, $CDCl_3$) δ: 77.18, 71.97, 70.61, 70.60, 70.52, 70.51, 66.30, 59.06, 18.55.

3.8.2.5 Aryl azide 86: ^{1}H NMR (400 MHz, $CDCl_3$) δ: 8.50 (s, 1H), 7.98 (d, *J* = 8.44, 1H), 7.03 (d, *J* = 8.44, 1H) ^{13}C NMR ($CDCl_3$, 100 MHz) δ_C 167.09, 142.90, 141.66, 140.23, 122.57, 121.48, 87.74.

3.8.2.6 (*S*)-1-{2-[2-(2-Methoxyethoxy)ethoxy]ethoxy}propan-2-yl 2-azido-5-iodobenzoate 88: ^{1}H NMR (400 MHz, $CDCl_3$) δ: 8.08 (d, *J* = 2.1 Hz, 1H), 7.76 (dd, *J* = 8.5, 2.1 Hz, 1H), 6.95 (d, *J* = 8.5 Hz, 1H), 5.32 – 5.23 (m, 1H), 3.73 – 3.57 (m, 12H), 3.55 – 3.51 (m, 2H) 3.35 (s, 3H), 1.33 (d, *J* = 6.5 Hz, 3H). ^{13}C NMR (100 MHz, $CDCl_3$) δ: 163.33, 141.72, 140.25, 140.00, 124.93, 121.79, 87.44, 77.16, 73.58, 72.00, 70.98, 70.83, 70.72, 70.69, 70.58, 59.09, 16.73.

3.8.2.7 (*S*)-1-{2-[2-(2-Methoxyethoxy)ethoxy]ethoxy}propan-2-yl 2-azido-5-[2 (triethylsilyl) ethynyl] benzoate 90: ^{1}H NMR (400 MHz, $CDCl_3$) δ: 7.89 (d, *J* = 2.0 Hz, 1H), 7.47 (dd, *J* = 8.4, 2.0 Hz, 1H), 6.98 (d, *J* = 8.4 Hz, 1H), 5.09 – 5.00 (m, 1H), 3.43 – 3.30 (m, 12H), 3.27 – 3.25 (m, 2H), 3.15 (s, 3H), 1.05 (d, *J* = 6.5 Hz, 3H), 0.00 (t, *J* = 7.9 Hz, 9H). ^{13}C NMR (100 MHz, $CDCl_3$) δ: 164.17, 139.88, 136.38, 135.29, 123.20, 119.87, 104.90, 104.50, 93.42, 73.68, 72.05, 70.89, 70.83, 70.77, 70.76, 70.74, 70.63, 59.13, 16.81, 7.60, 4.46.

3.2.8.8 Aryl amine side product 92: ^{1}H NMR (400 MHz, $CDCl_3$) δ: 7.97 (d, *J* = 2.0 Hz, 1H), 7.33 (dd, *J* = 8.5, 2.0 Hz, 1H), 6.56 (d, *J* = 8.5 Hz, 1H), 5.92 (bs, 2H), 5.35 – 5.22 (m, 1H), 3.72 – 3.57 (m, 12H), 3.55 – 3.50 (m, 2H), 3.36 (s, 3H), 1.34 (d, *J* = 6.4 Hz, 3H), 1.03 (t, *J* = 7.9 Hz, 9H).

3.8.2.9 (*S*)-2,5,8,11-Tetraoxatetradecan-13-yl 2-azido-5-ethynylbenzoate 72: ^{1}H NMR (400 MHz, $CDCl_3$) δ: 7.95 (d, *J* = 2.0 Hz, 1H), 7.60 (dd, *J* = 8.4, 2.0 Hz, 1H), 7.18 (d, *J* = 8.4 Hz, 1H), 5.37 – 5.24 (m,

1H), 3.74 – 3.57 (m, 12H), 3.55 – 3.51 (m, 2H), 3.36 (s, 3H), 3.12 (s, 1H), 1.35 (d, *J* = 6.5 Hz, 3H). ^{13}C NMR (100 MHz, $CDCl_3$) δ: 163.94, 140.48, 136.37, 135.53, 123.26, 120.05, 118.57, 104.90, 82.06, 78.54, 73.66, 72.04, 70.90, 70.85, 70.77, 70.73, 70.62, 59.13, 16.78.

3.8.2.10 Methyl(2*R*)-2-(tetrahydro-2H-pyran-2-yloxy)propanoate 81: ^{1}H NMR (400 MHz, $CDCl_3$) δ: δ 4.69–4.65 (m, 2H), 4.40 (q, *J* = 7.0 Hz, 1H), 4.19 (q, *J* = 6.8 Hz, 1H), 3.94 – 3.74 (m, 2H), 3.711 (s, 3H), 3.707 (s, 3H), 3.54 – 3.38 (m, 2H), 1.91 – 1.46 (m, 12H), 1.43 (d, *J* = 6.9 Hz, 3H), 1.37 (d, *J* = 6.9 Hz, 3H). ^{13}C NMR (100 MHz, $CDCl_3$) δ: 173.92, 173.81, 98.41, 97.73, 72.49, 70.07, 62.57, 62.55, 52.02, 52.00, 30.57, 30.48, 25.47, 25.36, 19.31, 19.27, 18.92, 18.12.

3.8.2.11 (2*R*)-2-(Tetrahydro-2H-pyran-2-yloxy)propan-1-ol 82: ^{1}H NMR (400 MHz, $CDCl_3$) δ: 4.70 (dd, *J* = 5.1, 2.7 Hz, 1H), 4.52 (dd, *J* = 6.3, 2.6 Hz, 1H), 4.01 – 3.72 (m, 4H), 3.69 – 3.37 (m, 6H), 1.87 – 1.64 (m, 5H), 1.61 – 1.43 (m, 8H), 1.18 (d, *J* = 6.4 Hz, 3H), 1.10 (d, *J* = 6.5 Hz, 3H). ^{13}C NMR (100 MHz, $CDCl_3$) δ: δ 99.99, 99.14, 77.75, 74.96, 67.27, 66.25, 64.64, 63.24, 31.67, 31.17, 25.44, 25.18, 21.00, 20.14, 17.81, 17.29.

3.8.2.12 (3*R*)-2,5,8,11-Tetraoxatetradecan-13-ol 84: ^{1}H NMR (400 MHz, $CDCl_3$) δ: δ 3.99 – 3.90 (m, 1H), 3.69 – 3.61 (m, 10H), 3.55 – 3.51 (m, 2H), 3.47 (dd, *J* = 9.9, 3.0 Hz, 1H) 3.36 (s, 3H), 3.24 (dd, *J* = 9.9, 8.4 Hz, 1H), 2.90 (s, 1H), 1.10 (d, *J* = 6.4 Hz, 3H). ^{13}C NMR (100 MHz, $CDCl_3$) δ: 77.18, 71.97, 70.61, 70.60, 70.52, 70.51, 66.30, 59.06, 18.55.

3.8.2.13 (*R*)-1-{2-[2-(2-Methoxyethoxy)ethoxy]ethoxy}propan-2-yl-2-azido-5-iodobenzoate 87: ^{1}H NMR (400 MHz, $CDCl_3$) δ: 8.08 (d, *J* = 2.1 Hz, 1H), 7.76 (dd, *J* = 8.5, 2.1 Hz, 1H), 6.95 (d, *J* = 8.5 Hz, 1H), 5.32 – 5.23 (m, 1H), 3.73 – 3.57 (m, 12H), 3.55 – 3.51 (m, 2H) 3.35 (s, 3H), 1.33 (d, *J* = 6.5 Hz, 3H). ^{13}C NMR (100 MHz, $CDCl_3$) δ: 163.33, 141.72, 140.25, 140.00, 124.93, 121.79, 87.44, 77.16, 73.58, 72.00, 70.98, 70.83, 70.72, 70.69, 70.58, 59.09, 16.73.

3.8.2.14 (*R*)-1-{2-[2-(2-Methoxyethoxy)ethoxy]ethoxy}propan-2-yl-2-azido-5-[2(triethylsilyl)ethynyl] benzoate 89: ^{1}H NMR (400 MHz, $CDCl_3$) δ: 7.89 (d, *J* = 2.0 Hz, 1H), 7.57 (dd, *J* = 8.4, 2.0 Hz, 1H), 7.14 (d, *J* = 8.4 Hz, 1H), 5.36 – 5.24 (m, 1H), 3.73 – 3.57 (m, 12H), 3.54 – 3.50 (m, 2H), 3.36 (s, 3H), 1.35 (d, *J* = 6.5 Hz, 3H), 1.03 (t, *J* = 7.9 Hz, 9H), 0.67 (q, *J* = 7.9 Hz, 6H). ^{13}C NMR (100 MHz, $CDCl_3$) δ: 164.17, 139.88, 136.38, 135.29, 123.20, 119.87, 104.90, 104.50, 93.42, 73.68, 72.05, 70.89, 70.83, 70.77, 70.76, 70.74, 70.63, 59.13, 16.81, 7.60, 4.46.

3.8.2.15 Aryl amine side product 91: ^{1}H NMR (400 MHz, $CDCl_3$) δ: 7.97 (d, *J* = 2.0 Hz, 1H), 7.33 (dd, *J* = 8.5, 2.0 Hz, 1H), 6.56 (d, *J* = 8.5 Hz, 1H), 5.92 (bs, 2H), 5.35 – 5.22 (m, 1H), 3.72 – 3.57 (m, 12H), 3.55 – 3.50 (m, 2H), 3.36 (s, 3H), 1.34 (d, *J* = 6.4 Hz, 3H), 1.03 (t, *J* = 7.9 Hz, 9H).

3.8.2.16 (*R*)-2,5,8,11-Tetraoxatetradecan-13-yl 2-azido-5-ethynylbenzoate 71: ^{1}H NMR (400 MHz, $CDCl_3$) δ: 7.95 (d, *J* = 2.0 Hz, 1H), 7.60 (dd, *J* = 8.4, 2.0 Hz, 1H), 7.18 (d, *J* = 8.4 Hz, 1H), 5.37 – 5.24 (m, 1H), 3.74 – 3.57 (m, 12H), 3.55 – 3.51 (m, 2H), 3.36 (s, 3H), 3.12 (s, 1H), 1.35 (d, *J* = 6.5 Hz, 3H). ^{13}C NMR (100 MHz, $CDCl_3$) δ: 163.94, 140.48, 136.37, 135.53, 123.26, 120.05, 118.57, 104.90, 82.06, 78.54, 73.66, 72.04, 70.90, 70.85, 70.77, 70.73, 70.62, 59.13, 16.78.

3.8.3 Synthesis of achiral monomer

3.8.3.1 2-[2-(Tetrahydro-2H-pyran-2-yloxyethoxy)ethoxy]ethanol 94: A solution of tetra- ethylene glycol **93** (5 g, 26.33 mmol) and 3, 4-dihydro-2H-pyran (1.6 g, 19. 04 mmol) in DCM was stirred at 0 ^{o}C for 1 h and at room temperature for 14 h before it was diluted with more dichloromethane, transferred to a separating funnel, washed with aq. $NaHCO_3$ and extracted 3 times with dichloromethane. The DCM residue was concentrated under reduced pressure and purified by column chromatography (hexane:ethyl acetate = 1:2) to yield the required 2-[2-(tetrahydro2H-pyran-2-yloxyethoxy)ethoxy]ethanol **94** (5.03 g, 70%) as a colorless oil. ^{1}H NMR ($CDCl_3$, 400 MHz) δ_H 4.59 (s, 1H), 3.77 – 3.72 (m, 2H), 3.60 – 3.45 (m, 8H), 3.52 – 3.46 (m, 3H), 3.42 – 3.36 (m, 1H), 3.25 (s, 1H), 1.75 – 1.67 (m, 1H), 1.62 – 1.57 (m, 1H), 1.50 – 1.38 (m, 4H). ^{13}C NMR ($CDCl_3$, 100 MHz) δ_C 98.76, 72.53, 70.39, 66.52, 62.05, 61.47, 30.42, 25.31, 19.30.

3.8.3.2 2-{2-[2-(Tetrahydro-2H-pyran-2-yloxy)ethoxy]ethoxy}-propyl 2-azido 5-iodobenzoate 95: Compound **95** was synthesized following the procedure for the synthesis of **87** using DCC (0.87 g, 4.21 mmol), 2-azido-5-iodobenzoic acid **86** (1.00 g, 3.46 mmol), 2-{2[2(tetrahydro-2H-pyran-2-yloxy)ethoxy]ethoxy}ethanol **94** (1.09 g, 3.94 mmol) and DMAP (0.05 g, 0.42 mmol) to afford **95** (1.36 g, 72%) as a very viscous pale yellow liquid after work-up and purification by column chromatography (hexane : EtOAc = 1:2). ^{1}H NMR ($CDCl_3$, 100 MHz) δ_H 7.99 (d, *J* = 2.08, 1H), 7.59 (dd, *J* = 2.08, 8.48, 1H), 6.80 (d, *J* = 8.48, 1H), 4.48 (t, *J* = 3.52, 3.6, 1H), 4.36 (m, 2H), 3.72 – 3.61 (m, 3H),

3.52 – 3.36 (m, 19H), 3.34 – 3.25 (m, 1H), 1.73 – 1.61 (m, 1H), 1.60 – 151(m, 1H), 1.50 – 1.25 (m, 4H). ^{13}C NMR ($CDCl_3$, 100 MHz) δ_C 163.63, 141.84, 140.37, 140.04, 124.35, 121.72, 98.93, 87.34, 73.68, 70.82, 70.65, 70.59, 70.53, 68.69, 68.25, 66.64, 62.20, 33.80, 30.56, 29.68, 25.56, 25.43, 24.88, 19.47, 17.11

3.8.3.3 2-{2-[2-(Tetrahydro-2H-pyran-2-yloxy)ethoxy]ethoxy}ethoxypropyl-2-azido-5[2(trimethylsilyl)ethynyl]benzoate 96*:* The TMS-aryl azide **96** was prepared following the procedure for the synthesis of **89** using THP-protected aryl iodide **95** (1.0 g, 1.82 mmol), trimethylsilyl acetylene (0.18 g, 1.82 mmol), THF (5 mL) and TEA (5 mL) $Pd(PPh_3)_4$ (0.02 g, 0.017 mmol) and CuI (0.003 g, 0.016 mmol). Two spots were observed on TLC after the reaction. These were separated upon workup using column chromatography (hexane: EtOAc = 1:2) The first fraction (R.F. = 0.6) (0.52 g, 55%) was determined by NMR to be the required aryl azide **96** as viscous yellow oil**.** ^{1}H NMR ($CDCl_3$, 400 MHz) δ_H 7.99 (s, 1H), 7.59 (d, *J* = 8.36, 1H), 7.25 (d, *J* = 8.36, 1H), 4.59 (s, 1H), 4.49 (d, *J* = 5.16, 2H), 3.93 – 3.87 (m,2H), 3.85 – 3.49(m, 12H), 1.90 – 1.80 (m, 1H), 179 – 1.70 (m,1H), 1.69 – 1.49 (m,4H), 0.25 (s, 9H). ^{13}C NMR ($CDCl_3$, 100 MHz) δ_C 164.43, 140.09, 136.38, 135.47, 122.69, 119.98, 119.75, 103.22, 99.02, 95.91, 73.97, 70.96, 70.79, 70.66, 68.82, 68.20, 66.76, 62.28, 30.69, 25.57, 19.59, 17.33, 0.00**.** The second fraction (R.F. = 0.45) (0.3 g) was determined by NMR spectroscopy to be an aromatic amine side product **97**, produced from reduction of the azide product by PPh_3. ^{1}H NMR ($CDCl_3$, 400 MHz) δ_H 7.87 (d, *J* = 1.76, 1H), 7.12 (dd, *J* = 1.76, 8.56, 1H), 6.35 (d, *J* = 8.56, 1H), 5.68 (bs, 1H, NH_2), 4.59 (t, *J* = 3.51, 3.56, 1H), 4.49 (d, *J* = 5.36, 2H), 3.64 – 3.58 (m, 3H), 3.51 – 3.33 (m, 21H), 3.27 – 3.23 (m, 1H), 1.62 – 1.55 (m, 1H), 1.51 – 1.49 (m, 1H), 1.40 – 1.25 (m, 4H), 1.02 (d, *J* = 6.32, 3H), 0.00 (s, 9H). ^{13}C NMR ($CDCl_3$, 100 MHz) δ_C 167.03, 150.41, 137.15, 135.41, 116.51, 110.17, 105.14, 98.82, 91.27, 73.69, 70.72, 70.45, 70.39, 68.49, 67.06, 66.52, 62.08, 30.43, 25.30, 19.36, 16.92, 15.02, 0.00

3.8.4 2-{2-[2-(Tetrahydro-2H-pyran-2-yloxy)ethoxy]ethoxy}propyl-2-azido-5-[2-(trimethylsilyl)-ethynyl]benzoate 96 (from amine 97): Aryl amine **97** (0.12 g, 0.24 mmol) in THF (15 mL) was cooled to 0 ^{o}C in a sodium chloride/ice bath and *t*-$BuNO_2$ (0.16 g, 1.58 mmol) added dropwise. The mixture stirred for a further 30 min at 0 ^{o}C. TMS-N_3 (0.072 g, 0.64 mmol) was then added drop wise and the mixture stirred at 0 ^{o}C for 30 min and at room temperature for 10 h. Progress of the reaction was followed by TLC(hexane/ethyl acetate = 1:2). Afterwards, the reaction mixture was concentrated

and the product purified by column chromatography (hexane:ethyl acetate = 1:2) affording the azide **96** (0.11 g, 85%) as a yellow viscous oil.

3.8.3.5 2-{2-[2-(Ethoxy)ethoxy]ethoxy}propyl2-azido-5-[2-(trimethylsilyl)ethynyl]benzoate 98: The TMS-aryl alcohol **98** was prepared following a procedure described for the synthesis of **88** using THP-protected aryl azide **97** (1 g, 1.93 mmol) and PTSA.H_2O (0.1 g, 0.526 mmol). Work-up and purification by column chromatography (hexane:ethyl acetate = 1:2) afforded the required aryl alcohol **98** (0.67 g, 80%) as a viscous pale yellow oil. ^{1}H NMR ($CDCl_3$, 400 MHz) δ_H 7.99 (s, 1H), 7.59 (d, *J* = 8.36, 1H), 7.19 (d, *J* = 8.36, 1H), 4.49 (d, *J* = 5, 2H), 3.86 (d, *J* = 8.64, 2H), 3.72 – 3.6 (m, 10H), 3.59 (d, *J* = 8.64), 2H 2.62 (bs, 1H), 0.25 (s, 9H). ^{13}C NMR ($CDCl_3$, 100 MHz) δ_C 164.03, 140.10, 136.40, 135.76, 135.47, 122.69, 119.97, 119.75, 103.23, 95.93, 73.86, 72.74, 70.93, 70.77, 70.71, 70.66, 70.63, 70.40, 68.78, 68.19, 61.80, 0.25.

3.8.3.6 Achiral Monomer 70: TMS protected aryl alkyne **98** (0.2 g, 0.45 mmol) was dissolved in THF, in a 25 mL round bottomed flask and TBAF (0.208 g, 0.8 mmol) added and the reaction mixture stirred for 5 min. The mixture was then filtered through a short silica gel plug, concentrated and purified by column chromatography (hexane : EtOAc = 1:3) to yield monomer **70** (0.13 g, 80%) as a dark red viscous oil. ^{1}H NMR ($CDCl_3$, 400 MHz) δ: 8.00 (s, 1H), 7.69 (d, *J* = 7.18 1H), 7.20 (d, *J* = 8.28, 1H), 4.48 (s, 2H), 3.82 (s, 2H), 3.70 – 3.61 (m, 12H), 3.18 (s, 1H), 2.51 (bs, IH). ^{13}C NMR ($CDCl_3$, 100 MHz) δ_C 164.25, 140.46, 136.43, 135.60, 122.60, 119.96, 118.50, 81.87, 78.45, 72.49, 70.67, 70.63, 70.56, 70. 27, 69.01, 64.49, 61.73.

3.8.4 Synthesis of pPATs

3.8.4.1 Synthesis of pPAT 99: A mixture of monomer **70** (0.002 g, 0.007 mmol), monomer **71** (0.52 g, 1.32 mmol**,** ascorbic acid (1.10 mg, 0.06 mmol) and PMDETA (4.40 mg, 0.25 mmol) in DMF (1 mL) was degassed of oxygen/air, in three freeze-pump-thaw cycles. The flask was backfilled with nitrogen, opened and CuBr (1.85 mg, 0.13 mmol) added and closed. After two more freeze-pump-thaw cycles, the reaction mixture was backfilled with nitrogen gas and transferred to a preheated oil bath at 40 ^{o}C and stirred for 48 h. After the reaction was completed, the flask was opened, the

crude polymer diluted with more DMF and precipitated from an aqueous EDTA solution. The mixture was vigorously stirred for an hour and centrifuged and decanted to afford the polymer. The polymer was re-dissolved in DMF, precipitated from aq. EDTA, stirred and centrifuged and decanted again. This process was repeated four times to remove the copper catalyst. To remove unreacted monomer(s) and short polymer chains, the crude pPAT were dissolved in $CHCl_3$ and further purified by dialysis using dialysis tubing with molecular weight cut-off of 10 kDa for 24 h in $CHCl_3$. Removal of the solvent afforded the required pPAT **99** as brown solid.

3.8.4.2 Synthesis of pPAT 100: The pPAT **100** was synthesized following the procedure described for the synthesis of pPAT **99** using a mixture of monomer **70** (0.047 g, 0.133 mmol), monomer **72** (0.471 g, 1.23 mmol, ascorbic acid (1.10 mg, 0.06 mmol), PMDETA (4.40 mg, 0.25 mmol) and CuBr (1.85 mg, 0.13 mmol).

3.8.5 Synthesis of coumarin dye

Compounds **107** – **109** were synthesized according to procedures in the literature and their structures confirmed by NMR [20].

3.8.5.1 3-Nitro-7-diethylaminocoumarin 107: ^{1}H NMR ($CDCl_3$, 400 MHz) δ: 8.73 (s, 1H), 7.45 (d, *J* = 8.24, 1 H), 6.51 (b, 2H), 3.89 (bs, 2H), 3.412 (q, 4H), 1.20 (t, *J* = 6.04, 7.0, 6H). ^{13}C NMR ($CDCl_3$, 100 MHz) δ_C: 162.31, 151.56, 149.45, 145.68, 137.21, 129. 01, 111.57, 105.03, 45.81, 12.90.

3.8.5.2 3-Amino-7-diethylaminocoumarin 108: ^{1}H NMR ($CDCl_3$, 400 MHz) δ: 7.28 (s, 1H), 6.19 (d, *J* = 8.24, 1 H), 6.69 (d, *J* = 8.96, 1H), 6.51 (s, 1H), 3.48 (q, 4H), 1.61 (t, *J* = 6.01, 6.24 6H). ^{13}C NMR ($CDCl_3$, 100 MHz) δ_C: 160.43, 156.89, 154.35, 139.37, 129.64, 113.67, 112.14, 111.08, 105.69, 45.41, 12.63.

3.8.5.3 3-Azido-7-diethylaminochromen-2-one (3-azido-7-diethylaminocoumarin) 109: ^{1}H NMR ($CDCl_3$, 400 MHz) δ_H 7.20 (d, *J* = 9.04, 1 H), 7.11 (s, 1H), 6.60 (d, *J* = 8.96, 1H), 6.52 (s, 1H), 3.44 – 3.39

(q, 4H), 1.24 – 1.20 (t, *J* = 6.04, 7.00 6H). ^{13}C NMR ($CDCl_3$, 100 MHz) δ_C: 158.34, 152.78, 151.89, 149.98, 149.34, 128.47, 118.18, 112.95, 111.02, 45.67, 12.72.

3.8.5.4 3-(3-Ethynylphenylcarbamoyl)propanoic acid 112: Succinnic anhydride **110** (190 mg, 1.9 mmol) was dissolved in anhydrous dichloromethane (7 mL) and followed by the addition of 3-ethynylaniline **111** (200 mg, 1.7 mmol). The mixture was allowed to stir at room temperature for 24 h. The solvent was evaporated under reduced pressure to afford **112** as a white solid (369 mg, 99%). ^{1}H NMR (DMSO-d_6, 400 MHz) δ_H 10.06 (s,1H), 7.77 (s, 1H), 7.54 (d, *J* = 8.08, 1H), 7.30 (t, *J* = 7.80, 7.92, 1H), 7.13 (d, *J* = 7.44, 1H), 4.14 (s, 1H), 2.60 – 2.49 (m, 8H). ^{13}C NMR (DMSO-d_6, 100 MHz) δ_C: 179.56, 175.60, 139.64, 129.12, 128.67, 127.71, 122.85, 121.37, 82.67, 80.07, 32.54, 30.73.

3.8.5.5 3-{3-[1-(7-(Diethylamino-2-oxo-2H-chromen-3-yl)-4,5-dihydro-1H-1,2,3-triazol-4-yl]phenylcarbamoyl}propanoic acid 102 (Coumarin Dye): To a mixture of phenylacetylene **112** (36 mg, 0.17 mmol) and 7-diethylamino-3-azidocoumarin **109** (45 mg, 0.17 mmol) in THF, sodium ascorbate (34 µL, 0.034 mmol) of freshly prepared 1 M solution in water was added, followed by the addition of 7.5 % of $CuSO_4.5H_2O$ in water (28 µL, 0.0085 mmol). The heterogeneous mixture was stirred vigorously overnight in the dark at room temperature. The THF was removed and the residue was diluted with water (20 mL), cooled in ice, and the precipitate collected by filtration. After washing the precipitate with cold water (3 X 10 mL), it was dried under vacuum and purified by column chromatography using methanol as eluent in chloroform to afford a yellowish green powder as product (0.51 mg, 84%).^{1}H NMR (DMSO-d_6, 400 MHz) δ_H 10. 62 (s,1H), 8.86 (s, 1H), 8.85 (s, 1H), 8.18 (s, 1H), 7.72 – 7. 58(m, 4H), 7.44 (t, *J* = 7.80, 7.92, 2H), 6.87 (d, *J* = 7.44, 2H), 6.67 (s, 2H), 2.56 (s, 4H), 1.12 (s, 6H). ^{13}C NMR (DMSO-d_6, 100 MHz) δ_c: 179.62, 174.93, 166.43, 152.67, 149.5, 142.34, 139.45, 130.59, 129.28, 128.01, 125.98, 121.75, 120.96, 112.65, 110.35,105. 67, 65.99, 45.13, 31.80, 30.11, 13.34.

3.8.6 Labeling of the pPATs

3.8.6.1 Synthesis of 2; Labelling of pPAT 100 with Rhodamine dye 101: DCC (0.87 g, 4.21 mmol) was added in one portion to a stirring solution of pPAT **100** (0.02 g) in dry re-distilled CH_2Cl_2 (50 mL),

rhodamine dye **101** (0.03 g) and DMAP (0.05 g, 0.42 mmol) in DMF (30 mL) at 0 ^{o}C. The reaction was further stirred for an hour at 0 ^{o}C, before being allowed to stir at room temperature for 72 h. After the reaction, the crude polymer-dye conjugate was precipitated into acetone, stirred for two hours and centrifuged to remove the unreacted dye and the by-products of esterification (urea). This process was repeated until the dye's colors disappeared to afford 0.03 g of reddish solid as product **2**.

3.8.6.2 Synthesis of 3; functionalizing of pPAT 99 with coumarin dye 102: The coumarin functional pPAT was prepared according to the procedure for synthesis of pPAT **2** using DCC (0.87 g, 4.21 mmol), coumarin dye **102** (0.03 g) and DMAP (0.05 g, 0.42 mmol) to afford **3**.

3.8.7 Synthesis of rhodamine-functional monomer

3.8.7.1 Rhodamine-functional (R)-{2-[2-(2-ethoxy)ethoxy]ethoxy}propyl-2-azido-5[2(trimethylsilyl)ethynyl]benzoate 103: DCC (0.11 g, 0.526 mmol) was added in one portion to a solution of Rhodamine B (0.2 g, 0.418 mmol) in dry re-distilled CH_2Cl_2 (50 mL), azide **98** (0.32 g, 0.651 mmol) and DMAP (0.006 g, 0.0525 mmol) at 0 ^{o}C. The reaction was stirred for an hour at 0 ^{o}C, before being allowed to stir at room temperature for 16 h. Afterwards the reaction mixture was chilled, the white precipitate of dicyclohexylurea filtered off and the productoi purified by column chromatography (chloroform : methanol = 95:5) to yield **103** as a viscous dark red viscous oil (0.23 g, 54%). ^{1}H NMR ($CDCl_3$, 400 MHz) δ_H 8. 27 (d, *J* = 6.84, 1H), 8.08 (d, *J* = 7.76, 1H), 8.85 (s, 1H), 7.69 (s, 1H), 7.57 (t, *J* = 6.52, 6.54, 1H), 7.49 (t, *J* = 6.52, 6.54, 1H), 7.34 (d, *J* = 8.22, 1H), 7.06 (S, 1H), 6.92 (d, *J* = 8.2, 1H), 6.82 (d, *J* = 7.4, 2H), 6.65 (d, *J* = 9.72, 2H), 6.56 (s, 2H), 6.50 (d, *J* = 6.96, 2H), 4.19 (bs, 2H), 3.92 (bs, 2H), 3.56 (bs, 2H), 3.45 - 3.30 (bm, 12 H), 3.06 (s, 4H), 1.08(t, *J* = 6.08, 6.88, 12H), 0.00 (s, 9H)

3.8.7.2 Rhodamine-functional monomer 104: TMS-protected rhodamine-functional monomer precursor **103** (0.2 g, 0.02 mmol) was dissolved in THF in a 25 mL round bottomed flask and TBAF (0.104 g, 0.4 mmol) added and the reaction stirred for 5 min. After work-up, only the starting monomer precursor **103** was isolated.

REFERENCES

1. K. H. Sandhage, S.M. Allan, M. B. Dickerson, C. S. Gaddis, S. Shian, M. R. Weatherspoon, Y. Cai, G. Ahmad, M. S. Haluska and R. L. Snyder, *Int. J. Appl. Ceram. Technol*., **2005**, 2, 317– 326.
2. S. Hecht and I. Huc, Foldamers: Structure, Properties and Applications, *Wiley-VCH*, Weinheim, **2007**.
3. G. M. Whitesides and B. Grzybowski, *Science,* **2002**, 295:2418-2421.
4. J. M. Lehn, *Science*, **2002**, 295:2400-2403.
5. P. J. G. Butler, *Phil.Trans. R. Soc. Lond. B*., **1976,** 276, 151 – 163.
6. Y. Okamoto and T. Nakano, *Chem. Rev.,* **1994**, 94, 349-372.
7. H. Y. Hu, J. F. Xiang, Y. Yang and C. F. Chen, *Org. Lett.* **2008**, 10, 69–72.
8. H. Goto, H. Katagiri, Y. Furusho and E. Yashima, *J. Am. Chem. Soc*., **2006**, 128, 7176 – 7178.
9. J. C. Nelson, J. G. Saven, J. S. Moore and P. G. Wolynes, *Science*, **1997**, 277, 1793 – 1796.
10. S. Lahiri, J. L. Thompson and J. S. Moore, *J. Am. Chem. Soc*., **2000**, 122, 46.
11. J. M Lehn, *Science*, **2002**, 295, 2400-2403.
12. K. A. Dill, *Biochemistry*, **1990**, 29, 7133-7155.
13. D. B. Amabilino, J.L. Serrano, T. Sierra and J. Veciana, *J. Polym. Sci., Part A: Polym.Chem*. **2006**, 44, 3161-3174.
14. R. Chinchilla and C. Na´ jera, *Chem. Soc. Rev*., **2011**, 40, 5084–5121.
15. A. J. Qin, J. W. Y. Lam and B. Z. Tang, *Chem. Soc. Rev*., **2010,** 39, 2522.
16. W. H. Binder and R. Sachsenhofer, *Macromol. Rapid Commun.,* **2008**, 29, 952–981.

17. J. Duchateau, L. Lutsen, W. Guedens, T. J. Cleij and D. Vanderzande, *Polym. Chem*., **2010**, 1, 1313– 1322.

18. F. Biedermann, E. A. Appel, J. del Barrio, T. Gruendling, C.Barner-Kowollik and O. A. Scherman, *Macromolecules*, **2011**, 44, 4828–4835.

19. T. Zdrojewski and A. Jon´ czyk*, J. Org. Chem*., **1998,** 63, 3.

20. K. Sivakumar, F. Xi , B. M. Cash, S. Long, H. N. Barnhill and Q. Wang, *Org. Lett*., **2004**, 6 (24) 4603– 4606.

21. R. Pfukwa, P. H. J. Kouwer, A. E. Rowan and B. Klumperman, *Angew. Chem. Int. Ed*., **2013**, 52, 11040 –11044.

22. Y. Tanaka, H. Katagiri, Y. Furusho and E. Yashima, *Angew. Chem. Int. Ed*. **2005**, 44, 3867.

23. X. Y. Ji, M. Q. Zhao, F. Wei and X. Qi. Feng, *Appl. Phys. Lett*., **2012,** 100, 263104.

24. Y. Wang, F Li, Y. Han, F. Wang and H. Jiang, *Eur. J Chem.,* **2009**, 15, 9424 – 9433.

25. A. M. Ramos, S. C. J. Meskers, E. H. A. Beckers, R. B. Prince, L. Brunsveldand A. J. Janssen*, J. Am. Chem*. *Soc*., **2004**, 126, 9630-9644.

26. X. Jia, S. Lou, H. Yuan,R. Yuan, S. Tian, C. Niu, X. Licand and S. Zhou*, J. Mater. Chem. C*, **2015**, 3, 79.

27. M. Gruziel andP. Szymczak, *Soft matter*, **2015**, 11, 6294-6304.

28. J. Chen, W. Liu, J. Ma, H. Xu, J. Wu, X. Tang, Z. Fan and P. Wang, *J. Org. Chem*., **2012**, 77, 3475−3482.

CHAPTER 4. GUEST GUIDED ORGANIZATION OF POLYARYLTRIAZOLE FOLDAMERS

4.1 Introduction

Guest-binding guided organization of foldamers involves the use of anions, cations and neutral organic molecules to induce the folding of flexible polymer strands [1-7]. In this chapter, a neutral organic template [poly(γ-benzyl-L-glutamate) (PBLG)] and anions are utilized in inducing and organizing the folding of our pPATs. The template-assembly structures and processes will be compared with their untemplated counterparts.

4.2 Template-guided assembly

The controlled fabrication of nanometer-scale objects is without doubt one of the central issues in current science and technology. For micro-sized objects made using self-assembly, careful design of hierarchical processes should lead to the creation of more intricate structures. Biological systems with their highly ordered assemblies show sufficient control, through templates, in the design and the interactions between the building blocks [8]. Inspired by nature, researchers are now pursuing *directed self-assembly,* where a template is fabricated to guide the correct folding of proteins in competition with other possible processes (such as intermolecular aggregation and precipitation) [9 – 13]. Like in the macroscopic world, a chemical template organizes reaction partners and thus allows the chemist to control their reactivity to achieve the formation of a desired product.

Generally, templates organize reaction partners for the formation of a desired product whose synthesis cannot be achieved in the absence of the template. While uncontrolled assembly operates on thermodynamic equilibrium, controlled assembly facilitates the modulation of thermodynamic forces to afford ordered non-equilibrium structures which are free from the constraints of entropy maximization. The template needs to bind to the reaction partners. Molecular recognition is thus a necessary prerequisite for template syntheses, and the binding sites of the components must be complementary to each other. Usually, binding is due to non-covalent bonds, although examples of

covalent templates exist. The control of reactivity and the recognition of the reaction partners imply information to be programed into the template which is transferred to the product of the reaction [6, 7, 9 – 13].

4.3 Introduction of the template

In this section, a template, hydrophobic poly(γ-benzyl-L-glutamate) (PBLG) **114** (**Figure 41**), is introduced and its effects and modifications on the pPATs assembly into higher order structures are analyzed by UV-Vis, CD and STEM.

This template (PBLG), which has previously been used to organize the assembly of pPATs into well-defined helices, was shown to be CD silent upon addition of up to 18% water fraction into the PBLG solution in DMF [26]. In these solvent mixtures (up to 18% water in DMF), PBLG equilibrated between right- and left-handed conformations, making it CD inactive [26]. The template was introduced at the transition region of the pPAT (10% water in DMF) when the PBLG template was CD inactive. In comparison to the helical structures assembled in the absence of the template, the templated structures were more stable and of longer length. Furthermore, self-assembly did not take place when the template was introduced in DMF before the addition of any water (**Figure 40**) [26].

In this work, the PBLG template will be introduced at 18% water fraction in DMF when it is still CD silent. In this solvent mixture, the pPATs' are already assembled into bundles of strands which are randomly organized (not yet ordered side by side). The side by side arrangement is a crucial step for the double helix assembly as earlier described (Chapter 3). At this stage (18% water content) when the template is introduced, no double helices have been formed and any observed differences in the structures assembled, in comparison with the double helical structures formed in the absence of the template, could be attributed to the template. A PBLG template of 110,000 Da was used [26]. The utilized amount of the pPAT was kept constant at 8.0×10^{-6} moles while the amount of the template was varied from 1.0×10^{-8} to 8×10^{-8} moles.

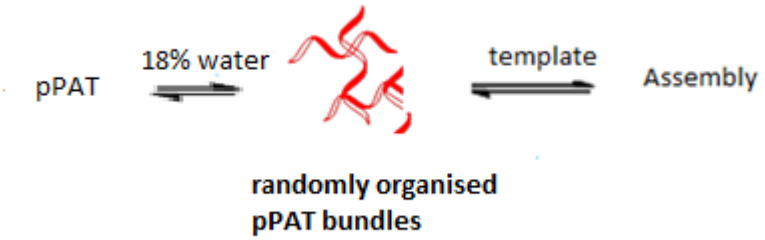

Figure 40: Approach for the introduction of the PBLG template

The α-helix template **114** has been described to exist in a tight wound helical conformation with 3.6 repeat units per turn and a residue translation of 0.15 nm, along the helical axis with a helical pitch of 0.54 nm. Hydrogen bonds formed between the N-H group and the four amide carbonyl repeat units stabilize the structure [26].

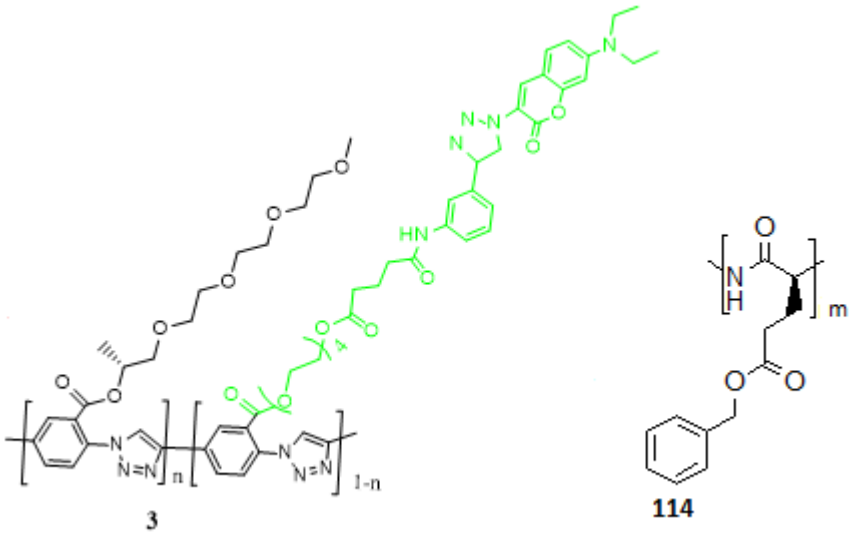

Figure 41: pPAT **3** and hydrophobic PBLG template **114** (n = fraction of the chiral monomer).

4.3.1 Template-guided hierarchical growth of chiral pPAT 3

4.3.1.1 UV-Vis analysis

Consistent with the untemplated pPATs assembly, the UV-Vis spectra are bimodal with peaks at lower and longer wavelengths corresponding to non-aggregated and aggregated pPATs. The 312/282 absorption ratio gradually increases with increasing concentration of the template (**Figure 42**). This is indicative of a helix assembly. Compared to the solvent-guided assembly (in the absence of the template) where double helices are formed, the pPAT's random coils thread around the PBLG template followed by stacking to form long ''tubules'' in template assembly. This is evident in the electron microscopic images taken at this point showing the pPAT threads around the template (**Figure 44**). Further, unlike the solvent-guided assembly, no equilibrium point is observed and the 312/282 ratio increases continuously with increasing concentration of the template.

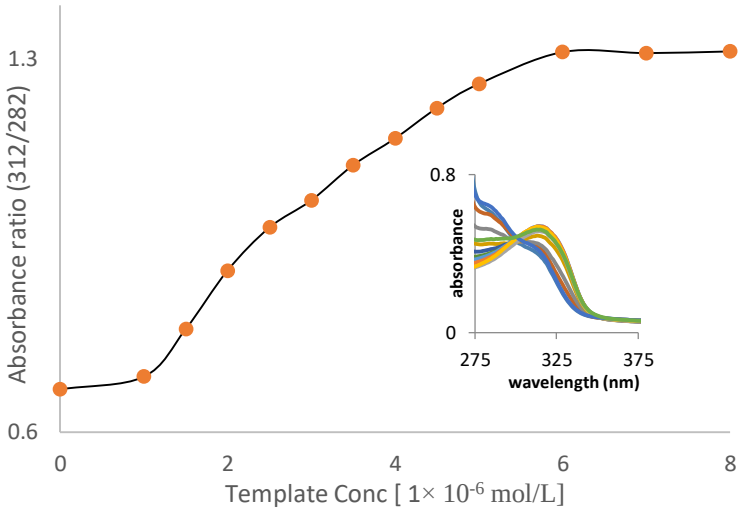

Figure 42: Uv-vis spectra (inset) and the 312/282 absorption ratio of pPAT **3** upon titration of 1.0 × 10^{-6} – 8.0 × 10^{-6} M of the template at 25 °C

4.3.1.2 CD Analysis

To confirm the chirality biased twist sense and the presence of purely one-handed structures, the CD measurements of the chiral pPAT **2** were monitored in different template concentrations by tracking the behavior of the Cotton effect (**Figure 43**). The CD experiments were performed in 18% water content in DMF when the template in CD inactive so that any changes in the CD spectra are attributed to the hierarchical organization of the pPATs in the presence of the template. The Cotton effect increased with increasing amount of template before eventually decreasing. The signals at

321 nm increase sharply with increasing the amount of template up to 4.0×10^{-6} moles due to threading of the pPAT strands around the template.

A gradual decrease in the Cotton effect is observed when the amount increases from 4.0×10^{-6} to 8.0×10^{-6} moles. This gradual decrease in the Cotton effect was attributed to multiple coiling of the pPAT's strands around the already threaded template and subsequent stacking. The multiple coiling of the pPAT's helical bundles around the already threaded template, which was confirmed by STEM images (shown later in **Figure 44**), presumably brings pPATs bundles into contact as they thread, on top of one another, around the template. This contact caused the lateral interactions of the pPAT bundles causing a decrease in the Cotton effect. The chirality transfer is confirmed by the presence of a uniform negative Cotton effect.

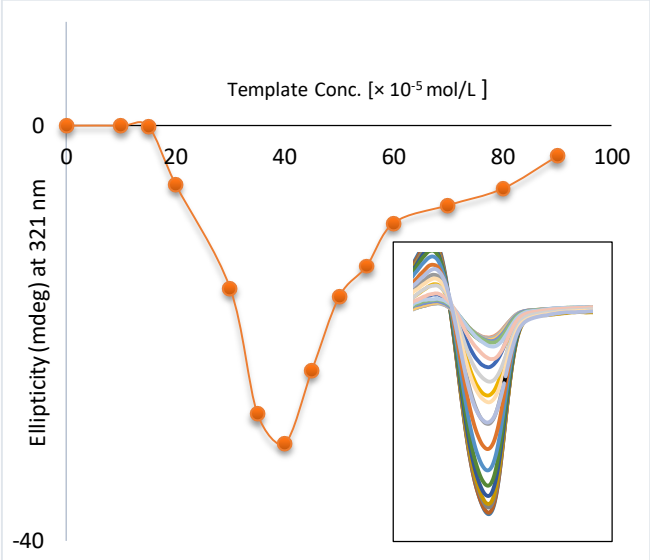

Figure 43: CD Spectra (inset) and the 321 nm absorption of pPAT **3** upon titration of 1.0×10^{-6} – 8.0×10^{-6} M of the template at 25 °C.

4.3.2 STEM Analysis

To obtain further evidence for the role of the template and the type of structures formed, STEM images were analyzed as the ratio of the template to the pPAT was increased from 0:1 to 2:1.

While pPAT's random bundles are observed when the template has not been added (**Figure 44a**), short nanostructures with clear morphologies in which the template is wrapped (coiled) around the template are observed when the ratio of the template to pPAT is 1:2 (**Figure 44**,). These structures presumably stack to yield long nanostructures of up to 10 micrometers in length and 150 nm maximum diameter (when the ratio of the template to pPAT is 1:1 as shown in **Figure 44b**). It is worth noting that varied diameter is observed for the templated structure as shown in the expanded section (**Figure 44c**). This is attributable to multiple coiling of the pPAT bundles around the template in some parts of the structure leading to the observed highest diameter of 150 nm.

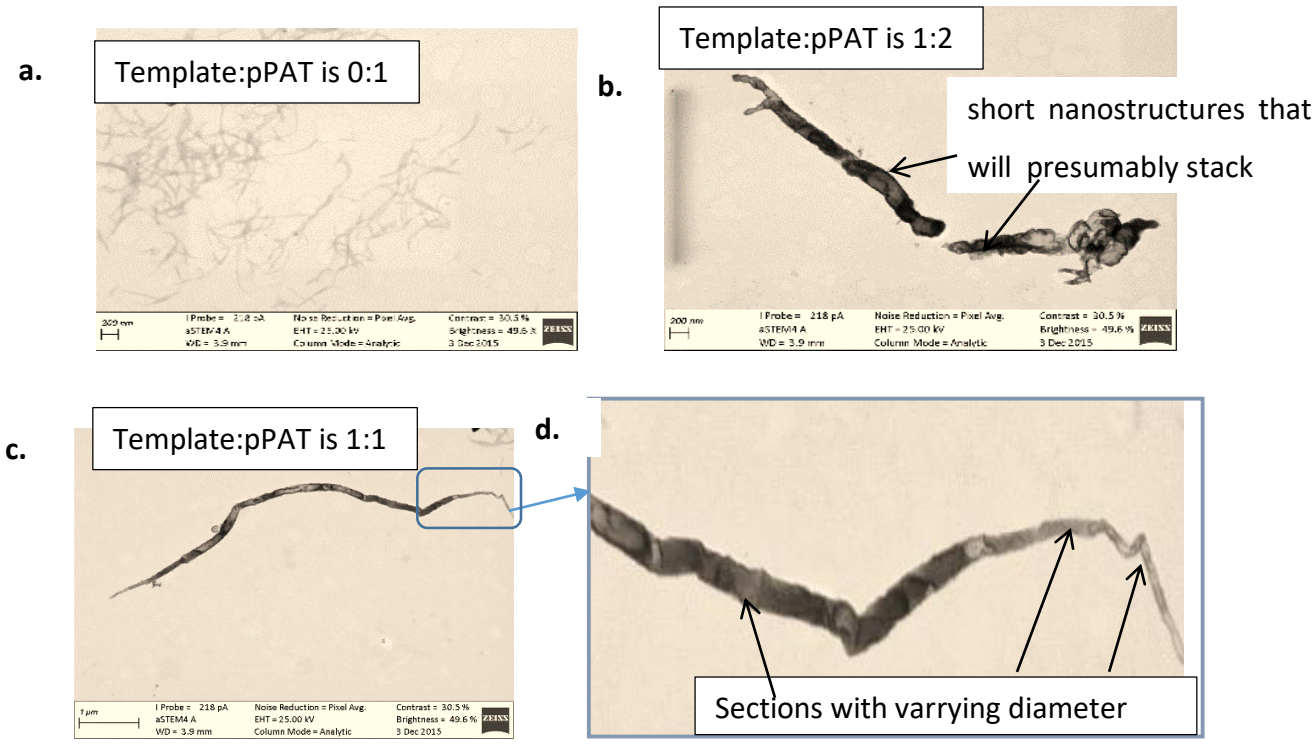

Figure 44: STEM image of templated assemblies when the ratio of the template to pPAT is (a) 0:1, (b) 1:2, (c) 1:1 and (d) an expansion to show the varied diameter of the structure.

4.3.3 Mechanism for template assembly

Having confirmed the wrapping or coiling of the pPAT bundles around the template by UV-Vis, CD and STEM, we postulated the assembly process for the observed structures to be a two-process-

mechanism. In the first process of the mechanism, the pPAT assembles into bundles strands that are randomly organized before the introduction of the template at 18% water fraction into the pPAT's solution in DMF. However, this process, for the organization of the pPATs random coils to bundles of strands, might have happened so fast when only a small amount of water had been added (18%) that it eluded our experimental capture. Only pPATs random bundles were observed at 18% water fraction as shown earlier in **Figure 44a**.

As soon as the template is added, the pPAT starts threading around the template in the second process of the mechanism to afford structures in which the pPAT is coiled around the template. The threading of the pPAT bundles around the template continues as more template is added. Further, multiple threading (coiling) of the pPAT bundles in some parts of the structures affords the observed highest diameter of 150 nm in some parts of the structure. These individual nanostructures, in which the pPAT bundles are wrapped around the template, stack on top of one another, thus yielding long nanostructures as shown in **Figure 45**.

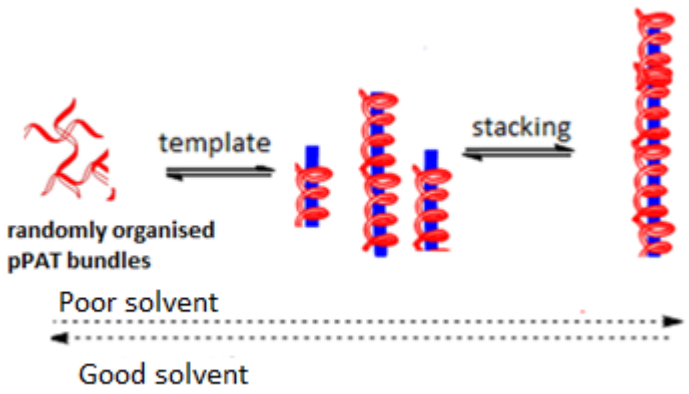

Figure 45: Proposed mechanism for the templated assembly. The pPATs random coils threads around the template.

4.4 Comparison of templated and untemplated assembly

4.4.1 Comparison of the UV-Vis and CD spectra

Comparison on the UV-Vis absorbance for the templated and non-templated (solvent-guided) assembly of our pPATs is shown in **Figure 46**. In the absence of a template, tightly twisted double helical structures of up to 10 micrometers in length are assembled upon increasing the amount of water from 10% to 80% into the pPAT solutions in DMF, in a process that involves the assembly of short double helices and subsequent stacking as previously discussed in Chapter 3. The onset of the stacking is marked by a pronounced "kick" in the absorbance ratio from 40% water indicated by an equilibrium point (shown by a circle in Figure **46).** In the presence of a template, this kick is not is not pronounced (**Figure 46b**). This is because the threading of the pPATs bundles around the template and subsequent stacking is a continuous process that starts as soon as a template is added. Importantly, the template modifies the hierarchical self-assembly processes observed for the untemplated assembly by eliminating the 'kick' as shown in the circled region (**Figure 46**).

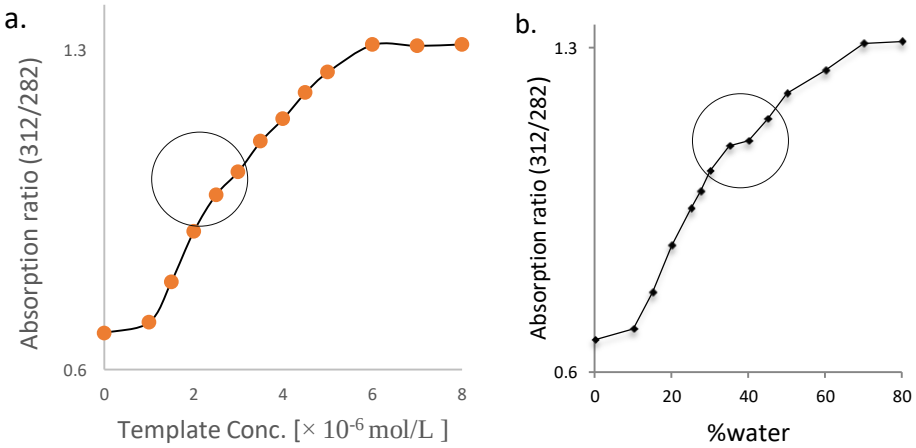

Figure 46: UV-Vis comparison of the 312/282 absorption ratio for (a) the templated and (b) the untemplated assembly of pPAT **3**

The CD spectra of the template assembly shows enhanced intensity (**Figure 47**). This was expected since the template stabilizes the structures formed.

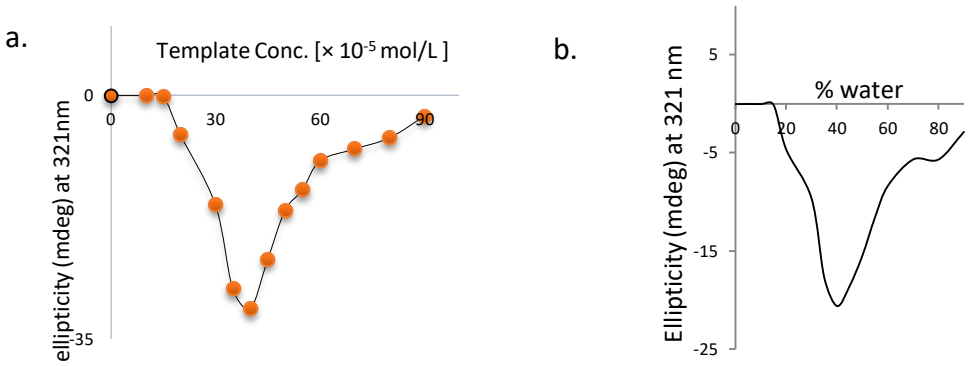

Figure 47: (a) Job's plot of the 321 nm absorption of pPAT **3** upon titration of 1.0×10^{-6} – 8.0×10^{-6} M of the template and (b) Job's plot for the absorption at 321 nm upon titration with 10 – 80% water [conc. of 8.0×10^{-6} M at 25 °C]

4.4.2 Comparison of templated and untemplated structures

In the absence of the template, the tubular-like structure is formed from a ''tightly'' twisted double helix (**Figure 48b**) as discussed in Chapter 3. In the presence of the template, the helices thread around the template to afford nanostructures (**Figure 48a**) following a completely different mechanism in comparison to the mechanism described for the double helical assembly. However, some of the dimensions for the templated and non-template assemblies are quite comparable. Such dimensions include the length of more than 10 micrometers and diameter of more than 150 nm.

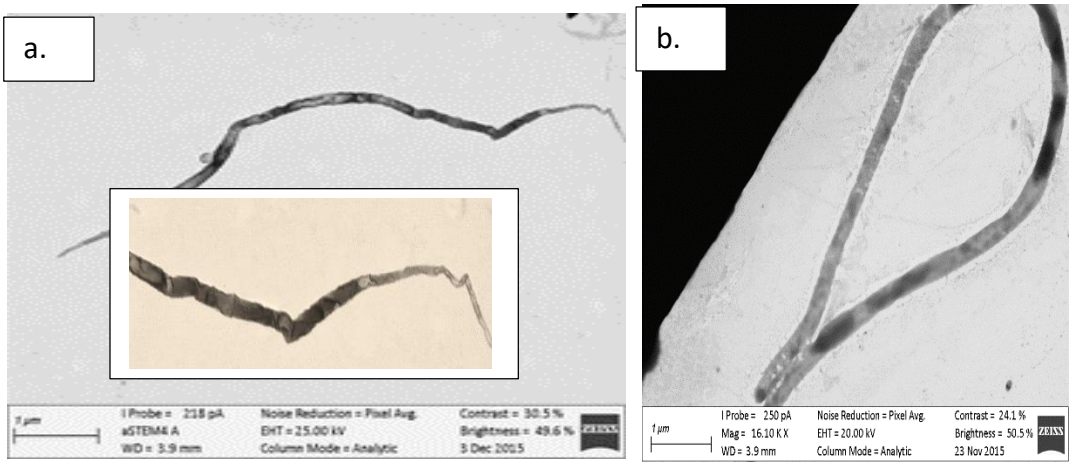

Figure 48: pPAT **3**'s STEM Images for the (a) templated and (b) untemplated assembly at 80% water.

4.5 Anion guided assembly

4.5.1 Introduction

Recent studies have presented the triazole ring as multifaceted in functionality. Easily accessed via the Cu(I)-catalyzed 1,3-dipolar cycloaddition (click) reaction of azides and acetylenes [15, 16], the triazole ring binds and forms complexes with cations, anions and neutral molecules. These properties are derived from the three electronegative sp^2 hybridized nitrogen's, which are nested on one side of the ring, and the electropositive C-H group, which also offers minor steric hindrance [16-21].

Utilizing the C^5-H, the triazole allows hydrogen bonding with electronegative species that are as strong as the classical, intrinsically polarized hydrogen bond donors N–H and O–H, and plays an important role in the conformation, interaction, and recognition of both organic and inorganic structures [1, 14, and 22]. Consequently, electron-deficient 1,4-diarylated 1,2,3-triazole derivatives form intermolecular bonds with halogen ions and other anions. Examples include a series of shape-persistent pre-organized triazolophanes, designed by Lee and Flood [23], that binds the chloride ion with a high affinity and selectivity over other halide ions. A pre-organized triazole based anion

receptor with two hydroxyl groups on the central phenylene ring has been reported [24]. Also, anion-binding light-induced triazole-based foldamers containing a photoresponsive azo-benzene in between the two phenyl-triazole oligomer units has been reported by Jiang *et*. *al*. [25].

Herein we show both the electropositive triazole C-H atom of 1,2,3-triazole ring as a potent intramolecular hydrogen bond donor and the re-organization or tuning of the conformation and/or shape of pPAT **2**. Different anions are introduced to the polytriazoles, and the changes in NMR and fluorescent properties arising from the binding effect of triazole moiety to the halogen ions were investigated.

4.5.2 NMR experiments

Considering the triazole ring as a functional group that can coordinate and form complexes with anions, we set out to investigate the pPAT binding and formation of complexes with halide ions through the changes in the pPAT's NMR and fluorescence spectra upon introduction of F^-, Cl^- and Br^- ions using their tetra-butyl ammonium sources in $CDCl_3$. Titration of these anions into the pPAT solution in $CDCl_3$ induced significant shifts of the triazole C-H proton signal in the ^1H NMR spectra. The Br^- ion induced the highest shift of the triazole C-H proton signal from 8.53 ppm for the uncoordinated pPAT to 8.96 ppm upon titration of up to 5.0×10^{-8} moles of Br^- into 8.0×10^{-8} moles of pPAT, as shown in the partial proton NMR spectrum (**Figure 49**). This is presumably because the larger bromide anion fits into the cavity of foldamer compared to the small sized fluoride and chloride anions. Generally, the shift of triazole C-H proton signal confirms the participation of triazole C-5 proton, as hydrogen bond donor, in coordinating the halide anion.

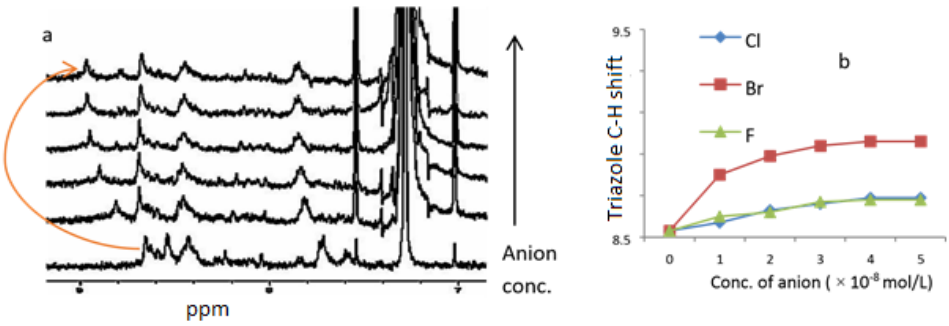

Figure 49: (a) ^{1}H NMR chemical shifts of pPAT **2**'s triazole signal (red arrow) as the number of moles of Br^- increases in chloroform, and (b) comparison of the shifts on the triazole proton upon titration of F^-, Br^- and Cl^- ions; the shifts in the ^{1}H NMR spectra of pPAT **2** upon increase in the titration of F^- and Cl^- ions are shown in **Figure A20** in the Appendices. The amount of the pPAT was maintained 8.0×10^{-6} moles.

In general, the binding of the halides to the pPAT presumably arises from an organization that involves folding up of the analogous pPAT strand such that the polarized triazole C-H H-bonds and the positive ends of their 5 D dipoles are directed into the central cavity to accommodate the halide [8]. Consequently, the presence of the halide ions induces rotation about the bonds connecting the triazole ring to the aryl ring which leads to folding into a helical conformation. The ester functionality is likely to exert a stronger polarizing effect on the CH H-bonds by virtue of its electron withdrawing character.

4.5.3 UV-Vis and CD experiments

In further studies to confirm the participation of the triazole C-H in coordinating to the anions, changes in the UV-Vis spectra upon introduction of the halide anions were investigated. Recent studies have shown that the formation of the complexes between the C-H group of the triazole and anions does quench fluorescence of the triazole-bearing chromophores [23]. As shown in **Figure 50** and consistent with NMR titrations, the pPAT displays a more pronounced quenching effect with Br^- compared with Cl^- and F^-.

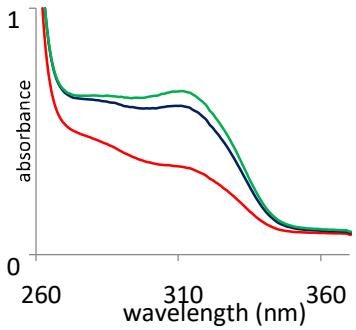

Figure 50: UV-Vis of pPAT **2** upon addition of 4.0×10^{-6} moles of Br^- (red), Cl^- (black) and F^- (green) at 25 °C in chloroform. The amount of the pPAT was 8.0×10^{-6} moles

To distinguish whether the observed optical properties were caused by aggregated and non-aggregated organizations of the pPAT **2** upon introduction of anions, the UV-Vis and CD behavior was monitored upon increasing the concentration of Br^- (**Figure 51**). Bromine was selected because it exhibits higher binding activity to the pPATs (as shown in Figure **50**).

Upon plotting the absorption at 312 nm against concentration of the chiral pPAT **2**, a linear behavior is observed which confirms the dependence of the optical properties on concentration. This suggests a folding but non-aggregating organization of the pPAT in the presence of the anion [26].

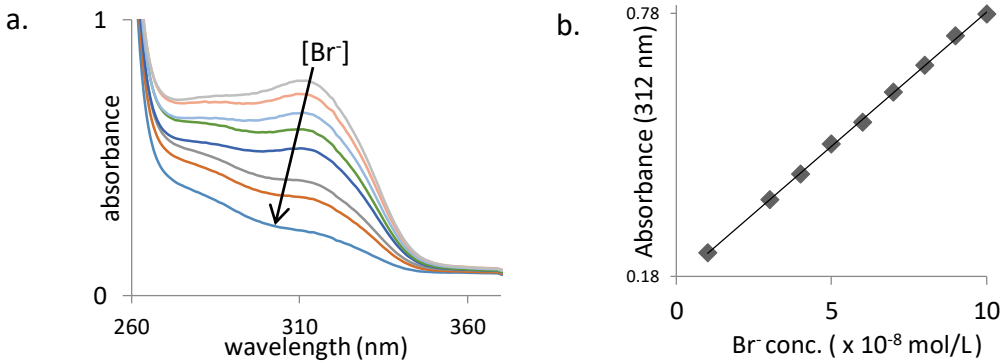

Figure 51: (a) UV-Vis absorption of chiral pPAT **2** in the presence of Br^- and (b) corresponding absorbance at 312 nm as a function of Br^- concentration. The amount of the pPAT was 8.0×10^{-6} moles

Similar results were observed from the CD experiments. Upon plotting the absorption at 321 nm versus the increasing concentration of the of bromide anions using 8.0×10^{-6} moles of pPAT **2** (**Figure 52**), a linear behavior is observed, which like the UV-Vis analysis, confirms a non-aggregating organization of the pPAT in the presence of the anion. The appearance of a negative Cotton effect shows the presence of only one-handed foldamers. Furthermore, the clear isodichroic point at 302 nm is indicative of the absence of lateral interactions which were observed in the assembly of the pPAT in the absence of anions.

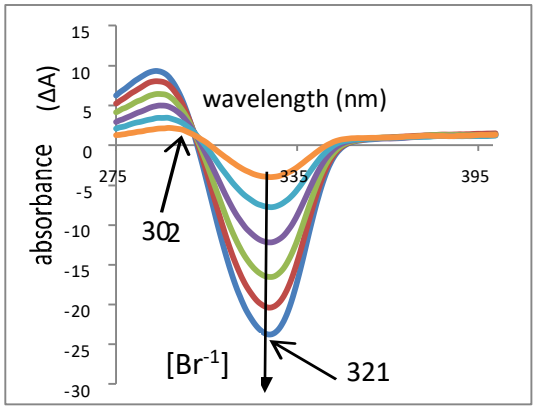

Figure 52: (a) CD Spectra of pPAT **2** upon titration of 1.0×10^{-6} – 6.0×10^{-6} M of Br^- at 25 °C. The amount of the pPAT was 8.0×10^{-6} moles.

Generally, the nature of the UV-Vis and CD spectra upon increasing the concentration of bromide ions reveals a non-aggregation assembly. The optical properties are dependent on concentration and, consequently, the UV-Vis absorption ratio (shown previously in **Figure 51b**)) and CD absorption at 321 nm (**Figure 53**) proceeds linearly with increasing concentration confirming non-aggregation assembly.

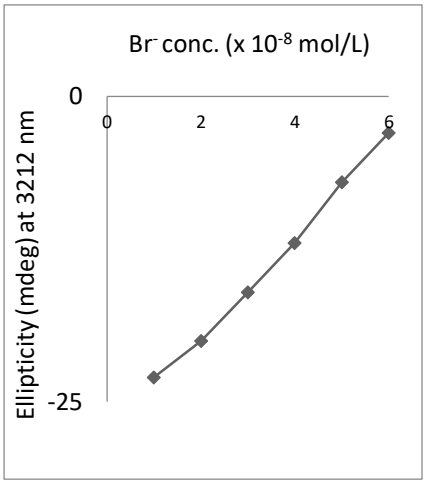

Figure 53: CD absorbance at 321 nm after titration of 1.0×10^{-6} – 6.0×10^{-6} M of Br^- at 25 °C. The amount of the pPAT was 8.0×10^{-6} moles.

4.6 Conclusions

Assembly of pPATs random coils in the presence of a template has been assessed via UV-Vis, CD and STEM, and compared to the untemplated assembly. The templated structures, which do not intertwine into double helices as in the case of the untemplated assembly, thread around the template and subsequently stack into long tubules. While the dimensions such as length (more than 10 micrometers) and diameter (150 nm) for the templated and non-templated assemblies are comparable, we have shown that such structures are assembled following completely different mechanisms. Furthermore, the pPATs show concentration-dependent aggregation behavior in the presence of anions. The pPATs bind to halide ions through the triazole, the binding of which is effective to prevent aggregated assembly and stacking. This is because the observed optical properties were linearly dependent on the concentration of the anion. As such, we have shown that the pPATs do not assemble into nanostructures in the presence anions.

4.7 Experimental

Solvents were purchased from Sigma Aldrich and Merck and used as received unless stated.

STEM samples [1 μM] (2 μL) were pipetted on to carbon coated 200 mesh copper grids, vacuum dried and then viewed using a JEOL 1200 – EX II TEM at 120 kV. Images were collected using a Proscan CCD camera.

UV-Vis spectroscopy measurements were carried out using a Perkin Elmer Lambda 20 photodiode array spectrophotometer in 1 cm quartz cuvettes. CD spectroscopy measurements were made using a Jasco J-815 instrument in 1 cm quartz cuvettes. The experiments were carried out at 25 ^{o}C unless stated otherwise. For PBLG templated assembly, UV-Vis and CD spectroscopy titration samples were prepared by mixing a fixed volume of pPAT (8×10^{-8} moles) from the a prepared stock solution in DMF with the 18% water by volume, template solutions of $1.0 \times 10^{-8} – 8 \times 10^{-8}$ moles from same stock solution of template in DMF. The samples were topped up to a fixed volume with DMF. The PBLG, 10000 Da, was purchased from Merk and used as received.

For anion guided-assembly, UV-Vis and CD spectroscopy titration samples were prepared by mixing a fixed volume of pPAT (8×10^{-8} moles) from a prepared stock solution in chloroform with $1.0 \times 10^{-8} – 6 \times 10^{-8}$ moles of Br^- from the same anionic stock solution of Br^- prepared using tetrabutyl ammonium bromide in chloroform. The samples were topped up to a fixed volume with chloroform. For NMR experiments, titration samples were prepared by mixing a fixed volume of pPAT (8×10^{-8} moles) in $CDCl_3$ with $1.0 \times 10^{-8} – 6 \times 10^{-8}$ moles of Br^- from the anionic stock solution of Br^- prepared using tetra-butyl ammonium bromide in $CDCl_3$. The samples were topped up to a fixed volume.

REFERENCES

1. J. M. Suk and K. S. Jeong, J. Am. *Chem. Soc*., **2008**, 130, 11868.
2. A. Petitjean, L. A. Cuccia, J. M. Lehn, H. Nierengarten and M. Schmutz, *Angew. Chem., Int. Ed*., **2002**, 41, 1195.
3. V. Berl, I. Huc, R. G. Khoury, M. J. Krische and J.-M. Lehn, *Nature,* **2000**, 407, 720.
4. R. B. Prince, T. Okada and J. S. Moore, *Angew. Chem., Int. Ed.,* **1999**, 38, 233.
5. M. Inouye, M. waki, and H. Abe, *J. Am. Chem. Soc.,* **2001**, 123, 1792.
6. A. Tanatani, M. J. Mio and J. S. Moore, *J. Am. Chem. Soc*., **2004**, 126, 2022.
7. A. Qin, J. W. Y. Lam and B. Z. Tang, *Macromolecules*, **2010**, 43, 8693-8702.
8. D. S. Goodsell, *Bionanotechnology*, Wiley-Liss, Hoboken, New Jersey, **2004**.
9. S. Anderson, H. L. Anderson and J. K. M. Sanders, *Acc. Chem. Res*., **1993**, 26, 469-475.
10. J. D. Watson and F. H. C. Crick, *Nature*, **1953**, 171, 964-9.
11. A. Imhof and D. J. Pine, *Nature*, **1997**, 389, 948-951.
12. M. A. Herman and H. Sitter, *Molecular Beam Epitaxy: Fundamentals and Current Status, 2nd Ed.*; Springer-Verlag: New York, **1996**.
13. Y. N. Xia, B. Gates, Y. D. Yin and Y. Lu, *Adv. Mater*., **2000**, 12, 693-713.
14. A. Qin, J. W. Y. Lam and B. Z. Tang, *Macromolecules* **2010**, 43, 8693-8702.
15. W. H. Binder and R. Sachsen-hofer, *Macromol. Rapid Commun*. **2008**, 29, 952-981.
16. A. Bianchi, K. Bowman-James and E. Garcia-Espana, Supramolecular Chemistry of Anions, *ed. Wiley-VCH*, **1997**.
17. J. L. Sessler, P. A. Gale and W.S. Cho, Anion Receptor Chemistry, *RSC Publishing*, **2006.**
18. Y. Hua and A.H. Flood, *Chem. Soc. Rev*., **2010**, 39, 1262-1271.
19. J. Alcantara-Garcia, V. Jancik, J. Barroso, S. Hidalgo-Bonilla, R. Cea-Olivares, R. A. Toscano and M. Moya-Cabrera, *Inorg. Chem*., **2009**, 48, 5874–5883.
20. M. Tropiano, C. J. Record, E. Morris, H. S. Rai, C. Allain and S. Faulkner, *Organometallics*, **2012**, 31, 5673–5676.
21. L. Y. You, S. G. Chen, X. Zhao, Y. Liu, W. X. Lan, Y. Zhang, H. J. Lu, C. Y. Cao and Z. T. Li, *Angew. Chem. Int. Ed*. **2012**, 51, 1657 –1661.

22. Y. Li, and A. H flood, *Angew. Chem., Int. Ed*., **2008**, 47, 2649-2652.

23. S. Lee, Y. Hua, H. Park and A. H. Flood, *Org. Lett*., **2010**, 12, 9, 2100-2102.

24. Y. Wang, F. Bie and H. Jiang, *Org. Lett*., **2010**, 12, 3630-3633.

25. Y. Wang, F. Li, Y. Han, F. Wang and H. Jiang, *Chem. Eur. J*. **2009**, 15, 9424 – 9433.

26. R. Pfukwa, P. H. J. Kouwer, A. E. Rowan and B. Klumperman, *Angew. Chem. Int. Ed*. **2013**, 52, 11040 –11044.

CHAPTER 5: AMPLIFICATION OF CHIRALITY; APPLICATION OF THE ''SERGEANTS AND SOLDIERS'' PRINCIPLE

5.1. Introduction

A large number of polymers are capable of adopting helical conformations. However, most of them fold into racemic mixtures of helical isomers. To bias the relative folding of two different helices and form unequal ratios of two diastereomeric helices, strategies such as the binding of chiral guests to achiral foldamers and the introduction of small chiral segments of foldamers as part of the backbones or side chains have been utilized [1-12].

The incorporation of small amounts of chiral side chains drives the assemblies to form domains with a particular handedness [13, 14]. This phenomenon referred to as 'sergeants and soldiers' involves small chiral units (sergeants) controlling the overall chirality and therefore folding handedness of achiral segments (soldiers) through cooperative interactions in the side chains. Green *et al.* have shown that a slight excess of one enantiomer leads to a strong bias towards the helicity preferred by the enantiomer that is present in the majority [15, 16]. Green's work was based on polyisocyanates which have stiff helical backbones. The macromolecular helicity of these polymers was quantitatively controlled via the incorporation of asymmetric centres in the side chain. Interestingly, the chiroptical properties of the polymers did not change when the ratio of the chiral to achiral monomers was lowered from 100:0 to 15:85. Even at 0.5% chirality, the polymers expressed a strong chiroptical activity.

Also, Meijer and co-workers observed large optical activities for chiral columnar assemblies containing only a small fraction (~5%) of chiral components [12, 17-19].

Generally, the transfer of chirality to the backbone, due to co-operativity of the side chains, results in a non-linear relationship between the number of chiral side chains and the specific optical rotation of an intrinsically helical polymer. Further insights into the fundamentals of chirality transfer and amplification as one potential mechanism responsible for the homochirality in bio macromolecules will enable the design of new enantioselective materials for chiral recognition and

asymmetric catalysis [20]. Henceforth, the access to responsive assemblies which allow for convenient tuning of properties is desirable.

In this chapter, the 'sergeants and soldiers' principle is examined using the achiral pPAT **1** incorporating different amounts of chiral side chains. Importantly, we report on the chirality amplification and cooperativity that causes the achiral components to 'follow' the helicity of the minority chiral components [15].

5.2 Synthesis and characterization of pure achiral and chiral pPATs

Two pPATs **115** and **1** containing chiral and achiral side chains, respectively, were prepared via the click-based Cu(I)-catalyzed AB step-growth co-polymerization of chiral monomer **72** and achiral monomer **70**, respectively, as shown in **Scheme 25**. The synthesis of the monomers was previously discussed (Chapter 3).

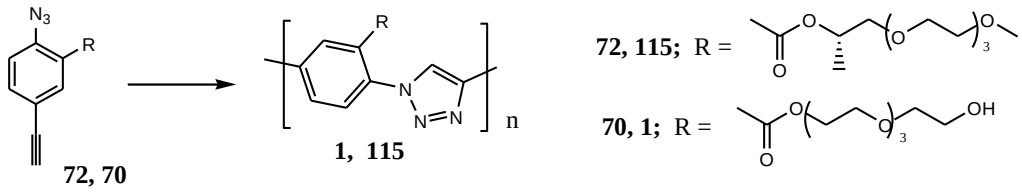

Scheme 25: Synthesis and characterization of pure achiral and chiral pPATs **1** and **115**

The structures of the pPATs were confirmed by ^{1}H NMR and SEC. **Figure 54** illustrates the assignment of proton signals in the ^{1}H NMR spectra for chiral and achiral pPATs **115** and **1**. The triazole ring C-H proton is observed at 9.43 ppm. For the achiral pPAT, the proton ortho to the ester group appears at 4.25 ppm while the terminal –OH proton signal appears at 4.58 ppm. For the chiral pPAT, the chiral centre proton is observed at 5.02 ppm for the chiral pPAT while its chiral methyl protons signal is observed at 1.00 ppm. The pPATs were also characterized by FTIR. For

illustration, **Figure A18** in the Appendices shows the FTIR spectrum of pPAT **1**. Notably, the monomeric azide stretch which is observed at 2300 cm^{-1} in the monomer spectrum (**Figure 21**) is absent in the polymer spectra due to conversion of this group to the triazole.

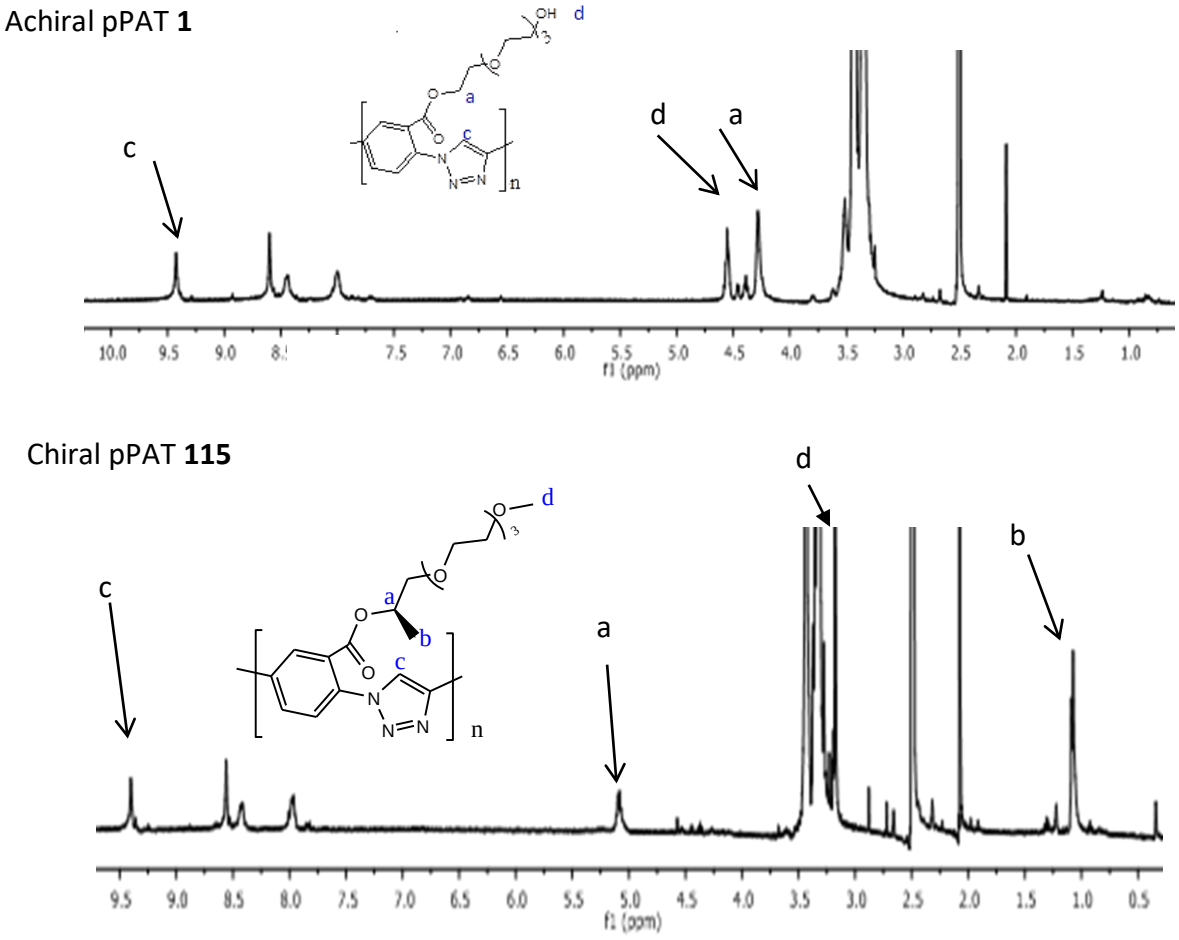

Figure 54: NMR spectra of achiral pPAT **1** and chiral pPAT **115**

5.3 Assembly behavior of the pure achiral and chiral pPATs

5.3.1 UV-Vis experiments

The achiral and chiral pPATs **1** and **115** exist as random coils in DMF and only form helices upon titration of the pPATs/DMF mixtures with water, as shown in **Figure 55**. Upon titration of 10 – 35%

water to the pPAT solutions in DMF, a gradual increase of the hyperchromic signals at 312 nm and the 312/282 absorption ratio is observed, which indicates the formation of helices. On adding 35 – 40% water, the 312/287 ratio remains constant. This equilibrium point is indicative of the existence of equal amounts of random coils and double helices. On increasing the amount of water from 40 – 70%, the hyperchromic signal at 312 nm decreases slowly and the 312/282 absorption ratio increases at the same rate. No more change is observed in the 312/282 absorption ratio upon increasing the amount of water above 70%. This is because all of the pPATs have already been organized and at this point exist in double helices and are stacked following a mechanism described earlier in Chapter 3.

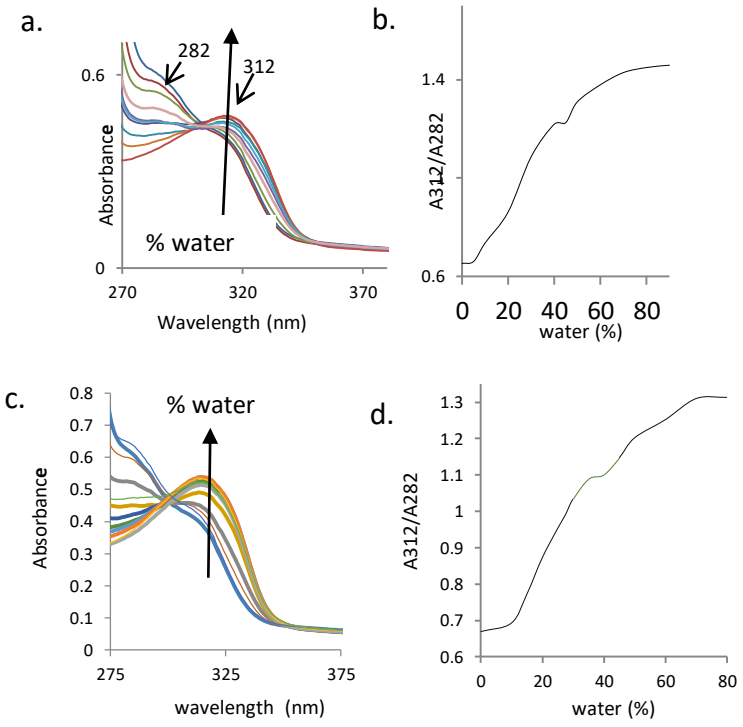

Figure 55: (a and c) UV-Vis absorption curves of chiral and achiral pPATs **115** and **1**, respectively, and (b and d) the corresponding Job plots for the 312/282 absorption ratio upon titration of 10 – 80% water [Conc. = 8.0×10^{-6} M at 25 °C]

5.3.2 CD experiments

To confirm the twist sense bias due to chirality, the chiral and achiral pPATs **115** and **1** were subjected to CD measurements as shown in **Figure 56**. The CD spectra for the achiral polymer show no Cotton effect, upon addition of water, due to non-biased folding leading to the formation of both right- and left handed double helices (**Figure 56b**). For the chiral pPAT **115**, a normal Cotton effect is observed (**Figure 56a**). The onset of the Cotton effect occurs when the fraction of water is about 10%. The absorption at 320 nm increase sharply with increasing the amount of water from 10 – 40% due to aggregation of the pPATs into double helical conformations with a bias for the one handed helical sense. Consistent with the UV-Vis analysis, a gradual decrease in the CD intensity is observed when the fraction of water is increased from 40 to 70% as a result of lateral interactions due to stacking of the double helices into long strands, a process that involves parallel strand-strand arrangement, coiling of adjacent strands and release of internal stress to gain balance between the changing van der Waals forces and surface tension brought about by the addition of water into the system.

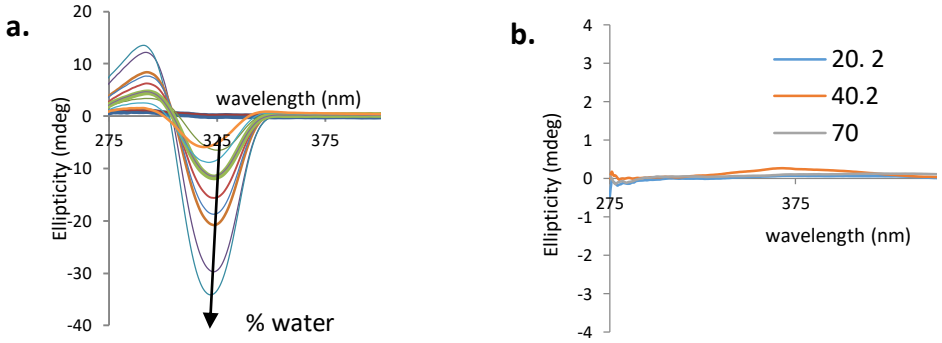

Figure 56: CD Spectra for (a) pPAT **115** upon titration with 10 – 80 % water, and (b) pPAT **1** upon titration of 20.2%, 40.2 % and 70% water [conc. = 8.0×10^{-6} M at 25 °C].

5.4 Preparation and characterization of mixed chain co-PATs

In a system with 'sergeants and soldiers' behavior, the chiral derivatives (sergeants) impose their chirality on a structure composed mainly of achiral segments (the soldiers). To study the chirality

transfer and amplification through CD-based 'sergeants and soldiers' experiments, three mixed chain co-pPATs **116**, **117**, and **118** containing 1%, 5 %, and 20% chiral components were prepared via the click based Cu(I)-catalyzed AB step-growth co-polymerization of 1%, 5 %, and 18% chiral monomer **72** with achiral monomer **70**, respectively, as shown in Scheme **26** and **Table 2**.

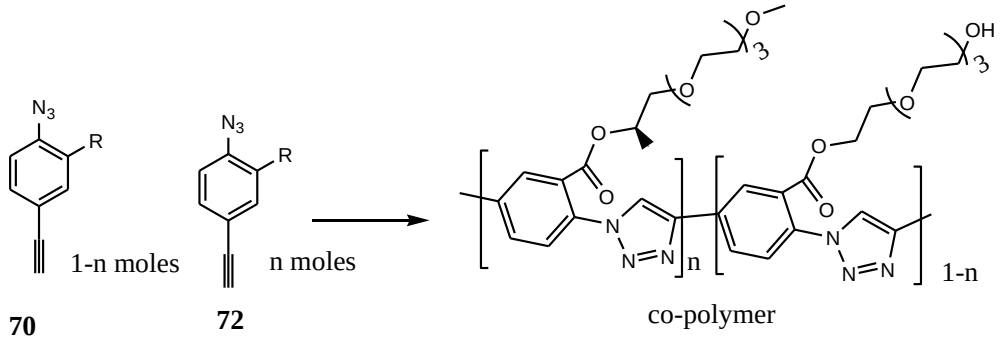

Scheme 26: Synthesis of co-pPATs **116**, **117** and **118.** The side chains (R) for monomers **70** and **72** are shown in **Scheme 25**. (n = fraction of the chiral monomer).

Table 2: Analysis of the polymers (pPATs and co-pPATs) used for 'sergeants and soldiers' experiments.

Polymer	Monomer **70**	Monomer **72**	M_w	M_n	*Đ*
1	0%	100%	20991	82408	3.9
115	100%	0%	18324	81016	4.4
116	99%	1%	17452	76123	4.3
117	95%	5%	19820	77656	3.9
118	82%	18%	17469	73451	4.2

The structures of the mixed chain co-pPATs were confirmed by ^{1}H NMR spectroscopy. They all show similar NMR spectra. For illustration, **Figure 57** shows the assignment of proton signals in the ^{1}H NMR spectrum for co-pPAT **118** with 18% chiral component. Generally, aromatic polymeric protons, compared to the monomers, are downshifted due to the deshielding effect of the triazole ring, which is absent in the monomers. The characteristic triazole ring C-H proton is the most deshielded and is observed at 9.43 ppm. Likewise, the proton ortho to the electron withdrawing ester group is deshielded and is observed at 8.56 ppm. The proton signal of the -CH_2 group close to the ester functionality appears at 4.09 ppm while the chiral methyl proton signal is observed at 1.03 ppm. The terminal –OH proton signal is observed at 4.58 ppm.

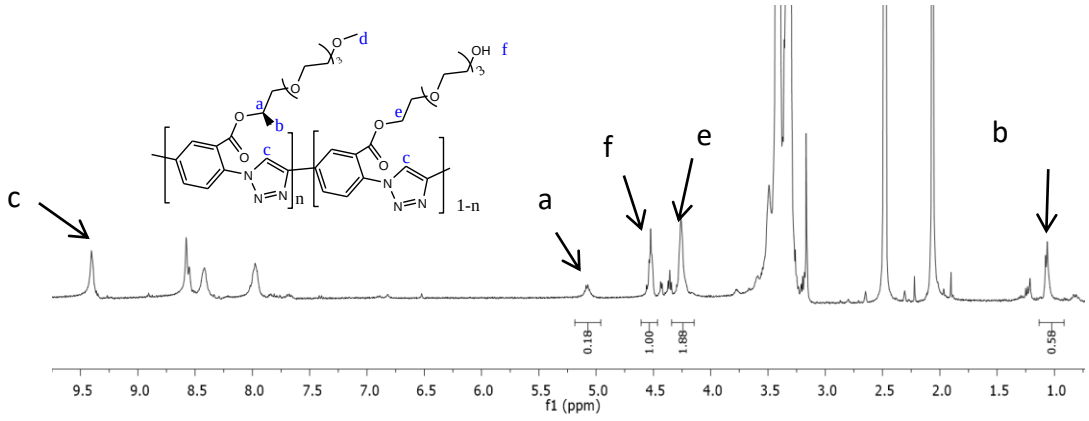

Figure 57: ^{1}H NMR spectrum for chiral pPAT **118** with 18% chiral component.

To approximate the fraction of each of the monomers in the polymer chain, the peak at 4.51 ppm (for the terminal –OH of the achiral monomer) and the peak at 5.01 ppm (for the chiral Centre proton) were integrated and their ratio was assumed to be the ratio of the monomers on the polymer chain. For further NMR analysis, **Figure 58** shows the overlay of the NMR spectra of the co-pPATs used for 'sergeants and soldiers' studies. It shows an increase in intensity of the peaks at 5.25 ppm (**a**) and 1.25 ppm (**b**) on increasing the amount of the chiral monomer. These are assigned to the proton of the chiral centre and the chiral methyl protons, respectively, as shown in the **Figure 57**.

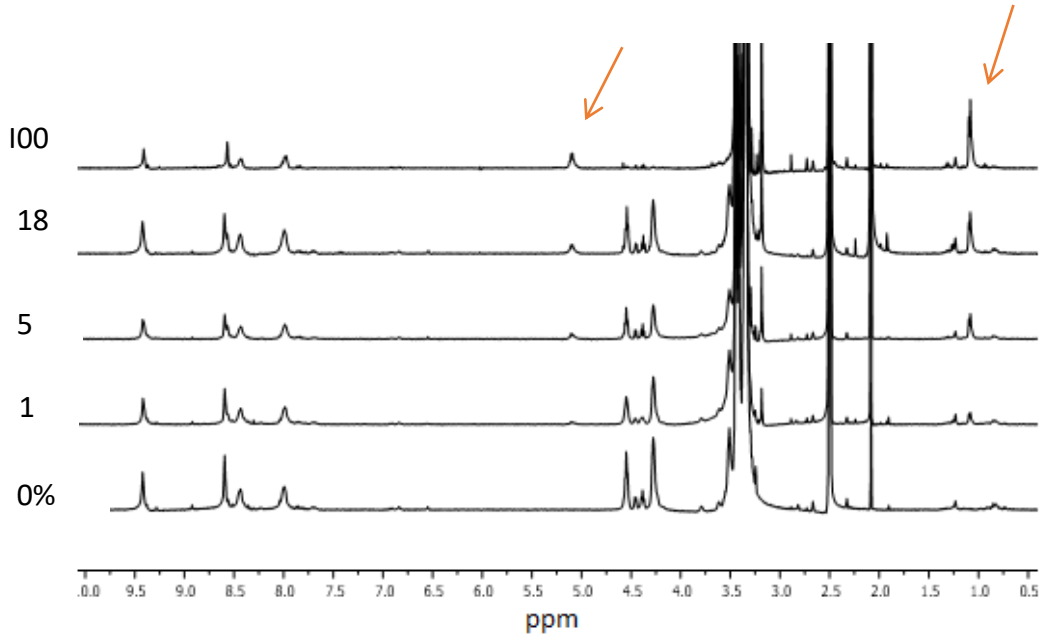

Figure 58: Overlay of the NMR spectra of the pPATs and co-pPATs; the % indicates the amount of chiral monomer used.

5.5 Chirality transfer and amplification: 'sergeants and soldiers' experiments

5.5.1 UV-Vis analysis of the co-pPATs

The co-pPATs exist as random coils both in DMF and up to 10% water fraction in DMF. In these solvent mixtures, no change in the 312/282 absorption ratio is observed as shown in figure **59b.** The co-pPATs only start to assemble into double helical nanostructure after 10% water has been titrated into the co-pPATs/DMFsolution. Upon titration of 10 – 35% water into the co-PAT solutions in DMF, a gradual increase of the hyperchromic signals at 312 nm and the 312/282 ratio is observed which confirms the assembly of the co-pPAT following the mechanism described for the untemplated assembly of pPATs in Chapter 3. The 312/282 ratio remains constant on adding 35 – 40% water. At this point some of the co-pPATs bundles of strands have been organized into double helical structures and as such the amount of co-pPATs bundles of strands (presumably ordered side by

side) and the double helices are equal. On increasing the amount of water from 40 – 70%, the remaining co-pPATs' bundles of strands continue to assemble into double helices while the already formed double helices stabilize and stack. This leads to observed gradual increase in the 312/282 absorption ratio as shown in **Figure 59** (for the mixed chain co-pPAT **118**).

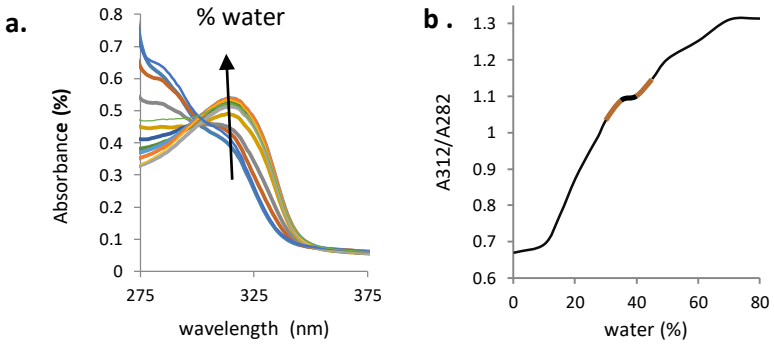

Figure 59: (a) UV-Vis spectra, and (b) the Job's plot for the 312/282 absorption ratio against the % of water titrated for the co-pPAT **118.**

Worthy to note is that the achiral, chiral and mixed chain pPATs (co-pPATs) exhibit similar UV-Vis spectra. As such, the UV-Vis experiments can only confirm the folding and formation of helices and cannot show the transfer of chirality. Circular dichroism experiments were then performed to determine the chirality transfer and amplification via the side chain co-operativity.

5.5.2 Circular dichroism experiments

Chiral amplification and propagation experiments were performed on all three mixed co-pPATs **116** – **118** under similar temperature, concentration and dilution conditions. The spectra were correlated to the amount of the chiral components to ascertain the chiral transfer.

In DMF (left), which solubilizes the co-pPATs very well, no folding occurs and thus no CD signal is observed. On the addition of water, a normal Cotton effect is observed for the CD signal at 321 nm. This is due to ordered aggregation of co-pPATs to double helices. The formation of one type of helix

handedness for all the co-pPATs with mixed side chains is confirmed by the presence of only a negative Cotton effect. For illustration, **Figure 60** shows the CD spectra for co-pPATs **116** (a) and **117** (b). The onset of the Cotton effect is initiated when the fraction of water is about 10% and it continues to increase until 40% water has been titrated. Consistent with the UV-Vis analysis, a gradual decrease in the CD intensity is observed when the fraction of water is increased from 40 to 70%. This behavior confirms the transfer of chirality from the side chain to the backbone leading the organization of the co-pPATs into helical conformation that is highly ordered with negative Cotton effect.

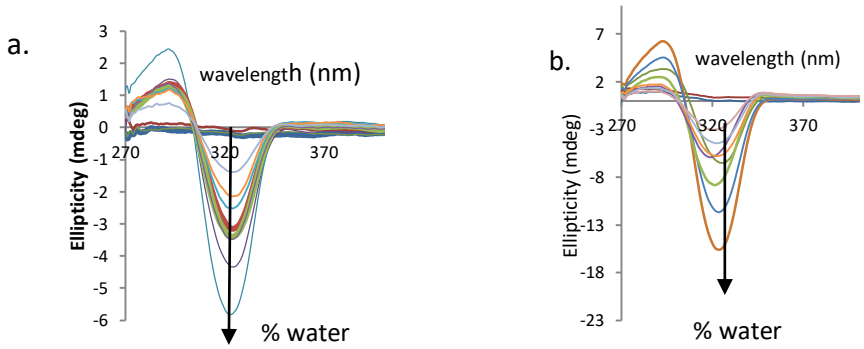

Figure 60: CD spectra for co-pPATs (a) **116** and (b) **117** upon titration with 10 – 80 % water [conc. = 8.0×10^{-6} M at 25 °C].

The plot of the CD_{max} points across the scanning range for achiral pPAT **1**, chiral pPAT **115** and the co-pPATs **116** – **118** with mixed side chains is shown in **Figure 61**. For the achiral pPAT **1**, no CD signal was observed due to the absence of chiral factors. pPAT **115** with all side chains chiral shows the largest Cotton effect. A considerable CD signal can be also observed for the mixed chain pPATs. Evidently, the Cotton effect increases with an increasing amount of the chiral segments for the co-pPATs. The presence of 1**%** of chirality in the co-PAT **116** amplifies the CD signal. Consequently, the CD signal intensity increases with increasing amount of chiral components, with co-pPAT **118** showing the highest Cotton effect among the co-pPATs. This is attributable to the highest percentage of chiral side chains in its structure. This observation demonstrates that the co-pPATs follow the 'sergeants and soldiers' rule. The sigmoid nature of the CD_{max} plots is likely to be due to the cumulative and cooperative nature of the assembly.

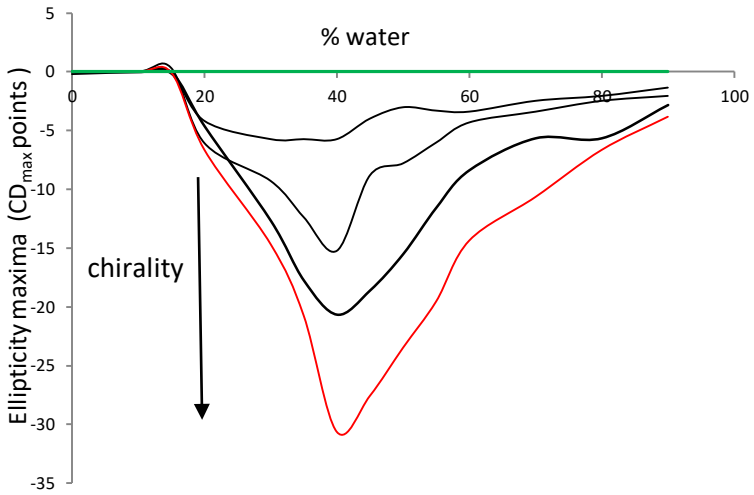

Figure 61: The plot of the CD_{max} points for the achiral (green), chiral (red) and the co-PATs with mixed side chains (black).

The plot of the CD_{max} at 40% water when all the pPATs show maximum Cotton effect is shown in **Figure 62**. The co-pPATs display a fairly strong Cotton effect, larger than expected in terms of linearity. The non-linear dependence of the optical activity on the percentage of the chiral side chains is observed. This supports a cooperative folding mechanism. The results further indicate that around 20% of the chiral side chains are needed for obtaining half the intensity of the Cotton effect exhibited by the homochiral pPAT.

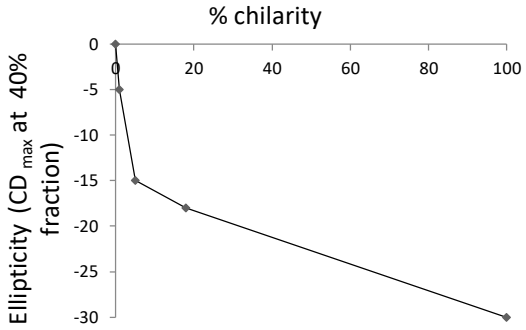

Figure 62: The plot of the CD_{max} points at 40% water fraction for all the pPATs and co-pPATs

The ability of the chiral side chain to transfer its chirality to the helical backbone was further examined by variable temperature CD experiments (**Figure 63**). The temperature denaturation behavior of co-pPAT **118** containing 18% chirality shows a similar transition shape for the loss of optical activity as co-pPAT **116** containing 1% chirality. The sigmoid temperature denaturation of the chiral helical conformations implies that the helical stability is affected by the number of chiral side chains, and the ratio of diastereomeric excess between the pPATs is not equal at all temperatures due to differences in the amount of chirality.

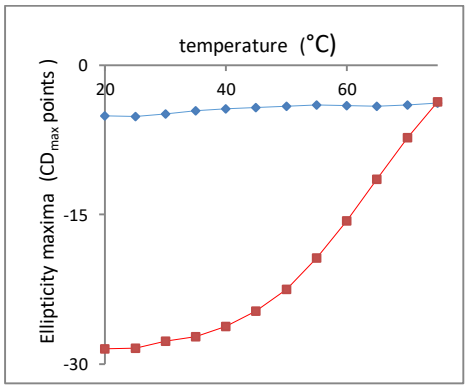

Figure 63: Temperature denaturation curves of co-pPATs **116** (blue) and **118** (red)

5.6 Conclusions

Amplification and propagation of chirality has been determined by CD based 'sergeants and soldiers' experiments on achiral pPAT containing different amounts of chiral side chains. The results indicate a non-linear dependence of the CD signal on the amount of chiral side chains, showing cooperativity among the side chains that leads to the transfer of chirality to the backbone. Chiral amplification was observed at as low as 1% of the chiral side chains. However, approximately 20% of the chiral side chains are needed for obtaining half the intensity of the Cotton effect exhibited by the homochiral pPAT.

5.7 Experimental

5.7.1 General information

All starting materials and solvents were purchased from Sigma Aldrich or Merck and used as received without further purification unless stated. ^{1}H NMR and ^{13}C NMR spectra were recorded on a Bruker Advance DPX 400 (400 MHz) or Oxford Origin (300 MHz) NMR spectrometers. NMR samples were prepared in deuterated solvents ($CDCl_3$ or DMSO-d_6) purchased from Sigma Aldrich or Merck. The samples were run at room temperature. Coupling constants (J) are given in Hz, while chemical shifts are expressed in parts per million (ppm) using TMS as internal reference.

FT-IR spectra were taken on a Bruker TENSOR 27 FT-IR spectrometer. Column chromatography was performed using silica gel (particle size 0.040-0.063 mm) purchased from Merck while thin layer chromatography (TLC) analyses were performed on pre-coated silica gel 60 F_{254} aluminum sheets (0.063 - 0.2 mm/70 - 230 mesh) purchased from Merck and compounds detected by observation under UV light and/or exposure to iodine vapour.

TLC SnakeSkin® pleated dialysis tubing, MW cut off 10000 Da, was purchased from Thermoscientific. SEC experiments were performed in DMAc at 40 ^{o}C and a flow rate of 0.5 mL/min, using a system equipped with a Waters 410 differential refractometer and PL Gel mixed C column (internal diameter 7.8 mm, length 30 cm). Samples were prepared by dissolving 200 mg in 4 mL of DMAc. Number average molecular weights (M_n) were calculated using calibration curves obtained from PMMA standards.

UV-Vis measurements were carried out on a Perkin Elmer Lambda 20 photodiode array spectrophotometer in 1 cm quartz cuvettes while CD measurements were made on a Jasco J-815 instrument in 1 cm quartz cuvettes. UV-Vis and CD titration samples (in μM concentration range) were prepared volumetrically, by mixing a fixed volume of pPAT/co-pPAT from the same stock solution, with the appropriate volume of water and/or DMF up to a constant total volume. These experiments were carried out at 25 ^{o}C, unless stated otherwise.

5.7.2 Syntheses

5.7.2.1 Synthesis of pPAT 1: A mixture of monomer **70** (0.48 g, 1.33 mmol), ascorbic acid (1.10 mg, 0.06 mmol) and PMDETA (4.40 mg, 0.25 mmol) in DMF (1 mL) was degassed of oxygen/air, in three freeze-pump-thaw cycles. The flask was backfilled with nitrogen, opened and CuBr (1.85 mg, 0.13 mmol) added and closed. After two more freeze-pump-thaw cycles, the reaction mixture was backfilled with nitrogen gas and transferred to pre-heated oil bath at 40 °C and stirred for 48 h. After the reaction, the flask was opened, the crude polymer diluted with more DMF and precipitated from an aqueous EDTA solution. The mixture vigorously stirred for an hour and centrifuged and decanted to afford the polymer. The polymer was re-dissolved in DMF, precipitated from aq. EDTA, stirred and centrifuged and decanted again. This process was repeated four times to get rid of all copper catalyst. To remove unreacted monomer(s) and short polymer chains, the crude pPAT were dissolved in $CHCl_3$ and further purified by dialysis using dialysis tubing with

molecular weight cut-off of 10 kDa for 24 h in $CHCl_3$. Removal of the solvent afforded the required pPAT **1** as brown solid.

5.7.2.2 Synthesis of pPAT 115: The pPAT **115** was synthesized following the procedure described for the synthesis of pPAT **1** using a mixture of monomer **72** (0.52 g, 1.33 mmol), ascorbic acid (1.10 mg, 0.06 mmol), PMDETA (4.40 mg, 0.25 mmol) and CuBr (1.85 mg, 0.13 mmol).

5.7.2.3 Synthesis of co-pPAT 116: The pPAT **116** was synthesized following the procedure described for the syhnthesis of pPAT **1** using a mixture of monomer **70** (0.475 g, 1.32 mmol), monomer **72** (0.005 g, 0.0133 mmol), ascorbic acid (1.10 mg, 0.06 mmol), PMDETA (4.40 mg, 0.25 mmol) and CuBr (1.85 mg, 0.13 mmol).

5.7.2.4 Synthesis of co-pPAT 117: The pPAT **117** was synthesized following the procedure described for the synthesis of pPAT **1** using a mixture of monomer **70** (0.46 g, 1.26 mmol), monomer **72** (0.026 g, 0.066 mmol), ascorbic acid (1.10 mg, 0.06 mmol), PMDETA (4.40 mg, 0.25 mmol) and CuBr (1.85 mg, 0.13 mmol).

5.7.2.5 Synthesis of co-pPAT 118: The pPAT 118 was synthesized following the procedure described for the synthesis of pPAT **1** using a mixture of monomer **70** (0.39 g, 1.09 mmol), monomer **72** (0.54 g, 0.239 mmol), ascorbic acid (1.10 mg, 0.06 mmol), PMDETA (4.40 mg, 0.25 mmol) and CuBr (1.85 mg, 0.13 mmol).

REFERENCES

1. T. Nakano and Y. Okamoto, *Chem. Rev*. **2001**, 101, 4013-4038.
2. Y. Okamoto and T. Nakano, *Chem. Rev*. **1994**, 94, 349-372.
3. H. Y. Hu, J.F. Xiang, Y. Yang and C. F. Chen, *Org. Lett*. **2008**, 10, 69–72.
4. P. K. Baruah, R. Gonnade, P. R. Rajamohanan, H.J. Hofmann and G. J. Sanjayan, *J. Org. Chem.,* **2007**, 72, 5077–5084.
5. Z. Zhong, andY. Zhao, *Org. Lett.,* **2007**, 9, 2891–2894.
6. R. M. Meudtner and S. Hecht, *Angew. Chem. Int. Ed.,* **2008**, 47, 4926–4930.
7. H. Masu, M. Sakai, K. Kishikawa, M. Yamamoto, K. Yamaguchi and S. Kohmoto, *J. Org. Chem.,* **2005**, 70, 1423–1431.
8. A. Khan, C. Kaiser and S. Hecht, *Angew. Chem*. *Int. Ed.,* **2006**, 45, 1878–1881.
9. H. Abe, H. Machiguchi, S. Matsumoto and M. J. Inouye, *Org. Chem*., **2008**, 73, 4650–4661
10. K. Goto and J. S. Moore, *Org. Lett.,* **2005**, 7, 1683–1686
11. D. B. Amabilino, J. L. Serrano, T. Sierra and J. Veciana, *J. Polym. Sci., Part A: Polym.Chem.* **2006**, 44, 3161-3174.
12. B. M. W. Langeveld-Voss, R. A. J. Janssen and E. W. Meijer, *J. Mol. Struct*., **2000**, 521, 285301.
13. Leonard J. Prins, Peter Timmerman and David N. Reinhoudt, *J. Am. Chem. Soc*., **2001**, 123, 10153-10163.
14. I. Destoop, H. Xu, C. Oliveras-Gonza´lez, E. Ghijsens, D. B. Amabilino and S. De Feyter, *Chem. Commun*., **2013**, 49, 7477—7479.
15. M. M. Green, M. P. Rediy, R. J. Johnson, G. Darling, D. J. O'Leary and G.Willson, *J. Am. Chem. Soc.,* **1989**, 111, 6452-6454.
16. M. M. Green, N. C. Peterson, T. Sato, A. Teramoto, R. Cook and S. Lifson, *Science*, **1995**, 268, 1860-1866.

17. A. R. A. Palmans, J. A. J. M. Vekemans, E. E. Havinga and E. W. Meijer, *Angew. Chem.* **1997**, *109,* 2763-2765; *Angew. Chem., Int. Ed. Engl.,* **1997**, *36*, 2648-2651.

18. L. Brunsveld, A. P. H. J. Schenning, M. A. C. Broeren, H. M. Janssen, J. A. J. M. Vekemans and E. W. Meijer, *Chem. Lett.,* **2000**, 292-293.

19. L. Brunsveld, B. G. G. Lohmeijer, J. A. J. M. Vekemans and E. W. Meijer, *Chem. Commun.,* **2000**, 2305-2306.

20. (a) R. M. Hazen and D. S. Sholl, *Nature*, **2003**, 2, 367; (b) T. Mallat, E. Orglmeister and A. Baiker, *Chem. Rev*., **2007**, 107, 4863.

CHAPTER 6. SUMMARY, CONCLUSIONS AND RECOMMENDATIONS FOR FUTURE WORK

6.1 Summary and conclusions

There is a growing interest in the design and synthesis of artificial helical polymers and oligomers in connection with biological importance as well as the development of novel chiral materials. Although the artificial double helices reported to date are still limited in number, recent advancement in supramolecular chemistry provides plenty of structural motifs for new designs. Therefore, artificial double helices hold great promise as a new class of compounds.

In this work, we have successfully demonstrated that polymeric strands can self-twist into well-defined double helical structures. Studies on the controlling factors revealed that solvents and chirality play a crucial role in the assembly of helical structures. The evolution process of the pPATs double helical structures was demonstrated via the analysis of UV-Vis and CD spectroscopy, and observations made from fluorescence and TEM images, which provided experimental evidence for the origin of double helical structures accomplished by the twisting of adjacent strands. Furthermore, the formation of the double helical structures may be realized through a balanced complex interplay between van der Waals forces among adjacent strands and free energy, as well as π-π interactions.

The absence of clear isodichroic and isosbestic points on the UV-Vis and CD spectra, respectively, upon increasing the amount of water, and therefore van der Waals forces, provided strong evidence for the formation of double helices. No single strand helices were observed when the assembly was followed by TEM and fluorescence imaging, and hence the foldamers first formed double helices directly from the random coils which further stacked with increasing solvophobic driving force and changes in the van der Waals forces and surface free energy upon increasing the water fraction of the pPATs solutions in DMF. Finally, columns of double helical stacks were visualized using TEM and fluorescence imaging upon driving the solvent system to 80 % water. Thus visual evidence of the

formation of double helices with a diameter of 200 nm, a pitch of 200 nm and a length of up 20 micrometers was obtained.

Further analysis of the CD spectra showed no inversion of chirality. This confirms the formation of a one-handed double helix. The individual strands intertwine in a similar one-handed helical twist to form double helices.

Assembly of the pPAT random coils in the presence of a template has also been assessed via UV-Vis, CD and TEM, and compared to the untemplated assembly. The template was introduced while the pPATs still existed as random bundles so that any observed differences in the structures assembled could be attributed to the template. Analysis of the templated structures via UV-Vis, CD spectroscopy and observation of TEM images showed the absence of double helices. Apparently, intertwining into double helices did not take place; rather, the pPATs random bundles thread around the template and subsequently stack into long nanostructures. Without forming double helical structures in the presence of a template, the template structures are formed following a completely different mechanism. The pPATs show concentration-dependent self-assembly behavior in the presence of anions. These pPATs bind halide ions through the triazole, and the binding of which is effective to prevent the assembly of the pPATs into nanostructures. Finally, a large number of polymers are capable of adopting helical conformations. However, most of them fold into racemate mixtures of helical isomers. To bias the relative folding of two different helices and form an unequal ratio of two diastereomeric helices, strategies such as the binding of chiral guests to achiral foldamers and the introduction of small chiral segments of foldamers as part of the backbones or side chains have been utilized. In this work, it was also proved that the addition of small amounts of small chiral segments on the structure of the achiral pPAT can bias the twist sense through side chain co-operative amplification and propagation of chirality. CD-Based 'sergeants and soldiers' experiments on the achiral pPAT with 0%, 1%, 5%, 20% and 100% chiral side chains indicated a non-linear dependence of the CD signal on the amount of chiral side chains. Chiral amplification was observed at as low as 1% of the chiral side chains. However, approximately

20% of chiral side chains are needed for obtaining half the intensity of the Cotton effect exhibited by the homochiral pPAT.

6.2 Recommendations for future work

While this work may provide a new alternative approach to the design and construction of well-ordered helical assemblies, the use of NMR spectroscopy to monitor the assembly of our pPATs is recommended. This will show how different protons interact and provide information on their relative distances in the course of the assembly, and thereby deliver more insights into the assembly pathways and mechanisms.

Furthermore, potential applications of our PATs can be derived from its triazole. Specifically, recent studies have presented the triazole ring, which is easily accessed via the Cu(I)-catalyzed 1, 3-dipolar cycloaddition (click) reaction of azides and acetylenes, as multifaceted in functionality [1 – 4]. In this light, it would be interesting to investigate how the introduction of cations, upon binding to the PATs via the triazole, can re-organise or tune the double helix conformation and/or shape the pPATs. Also, the possibility of using these pPATs for anion and/or cation chemosensing will be an attractive endeavor. This will be achievable via analyzing the sensitivity of the pPATs through changes in the NMR, UV-Vis, fluorescence and CD properties upon binding to different cations.

6.3. REFERENCES

1. J. Scheel, H. Komber and B. I. Voit, *Macromol. Rapid Commun*., **2004**, 25, 1175.
2. W. H. Binder and C. Kluger, *Macromolecules*, **2004**, 37, 9321.
3. C. W. Tornoe, C. Christensen and M. Meldal, *J. Org. Chem*., **2002**, 67, 3057.
4. S. Punna, J. Kuzelka, Q. Wang and M. G. Finn, *Angew. Chem. Int.Ed*., **2005**, 44, 2215.

APPENDICES

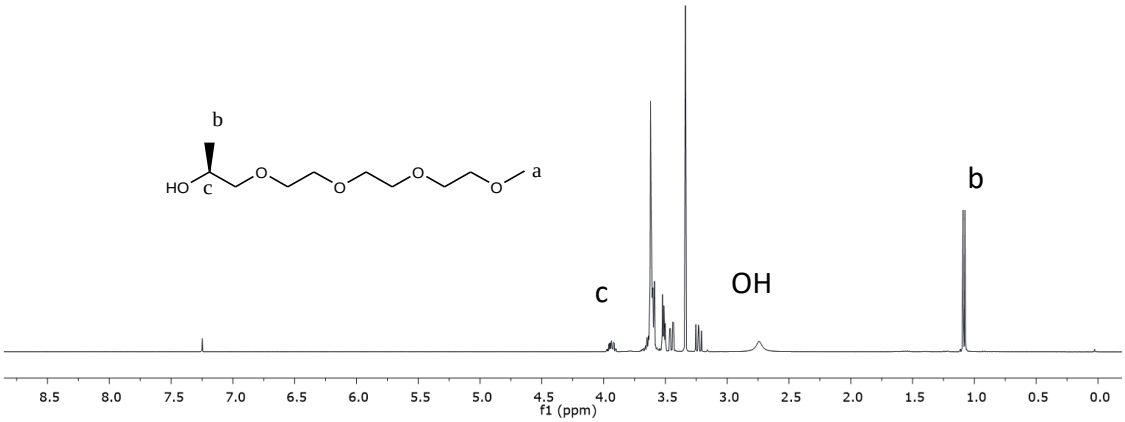

Figure A1: ^{1}H NMR spectrum of (13*S*)-2,5,8,11-tetraoxatetradecan-13-ol **79**

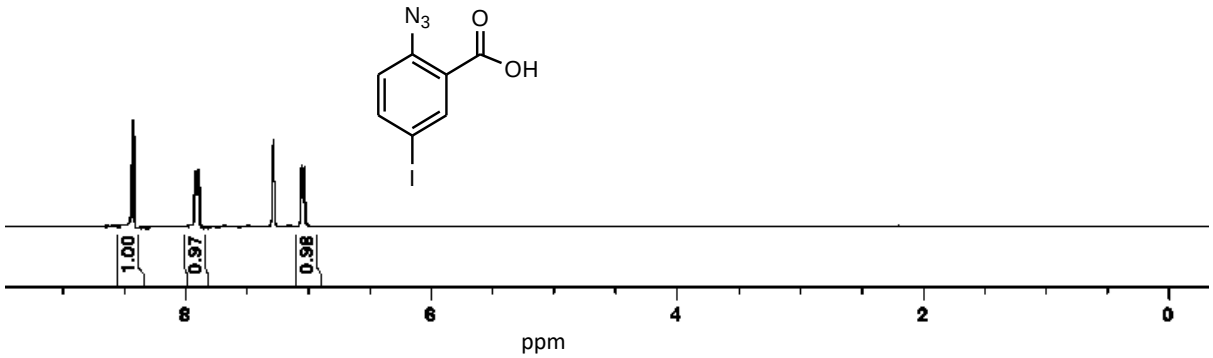

Figure A2: ^{1}H NMR spectrum of aryl azide **86**.

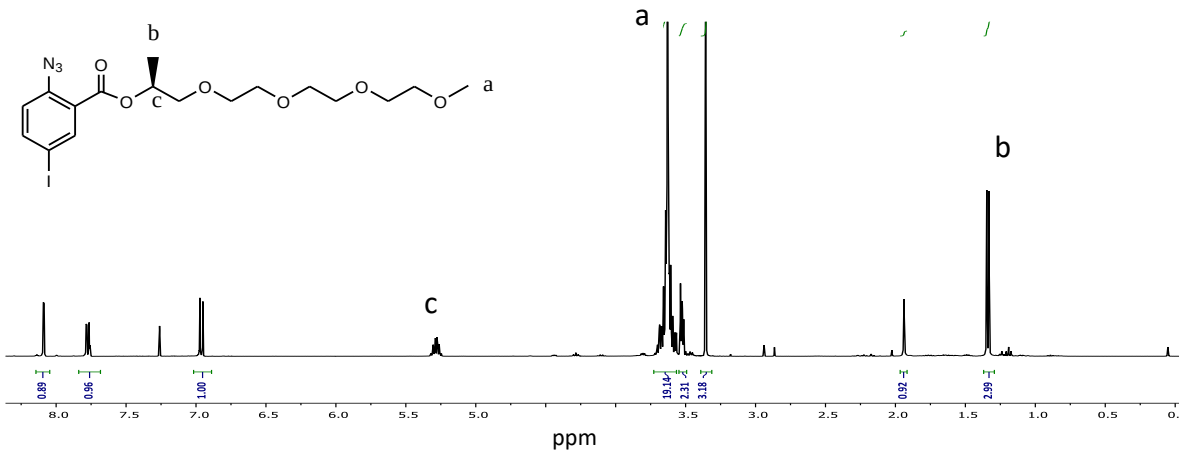

Figure A3: ^{1}H NMR spectrum of (*S*)-1-{2-[2-(2-methoxyethoxy)ethoxy]ethoxy}propan-2-yl 2-azido-5-iodobenzoate **88**.

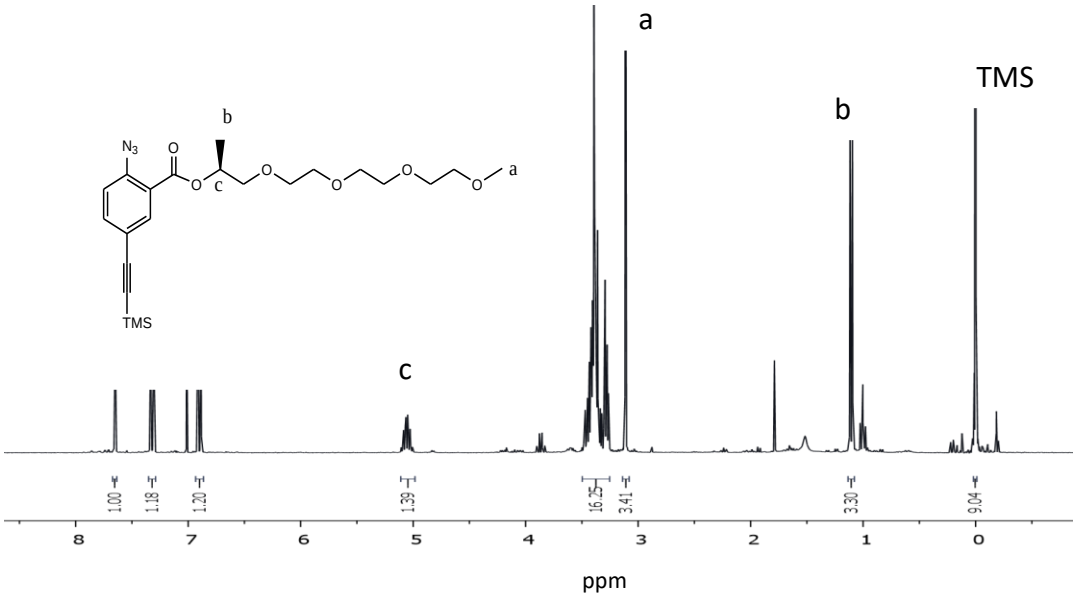

Figure A4: ^{1}H NMR spectrum of (*S*)-1-{2-[2-(2-methoxyethoxy)ethoxy]ethoxy}propan-2-yl 2-azido-5-[2 (triethylsilyl) ethynyl] benzoate **90**.

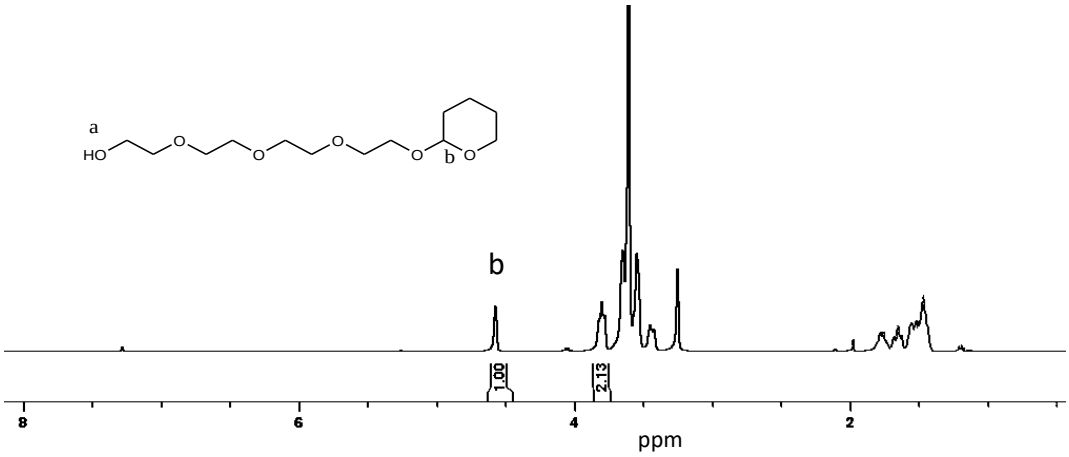

Figure A5: ^{1}H NMR spectrum of 2-[2-(tetrahydro-2H-pyran-2-yloxyethoxy)ethoxy]ethanol **94**.

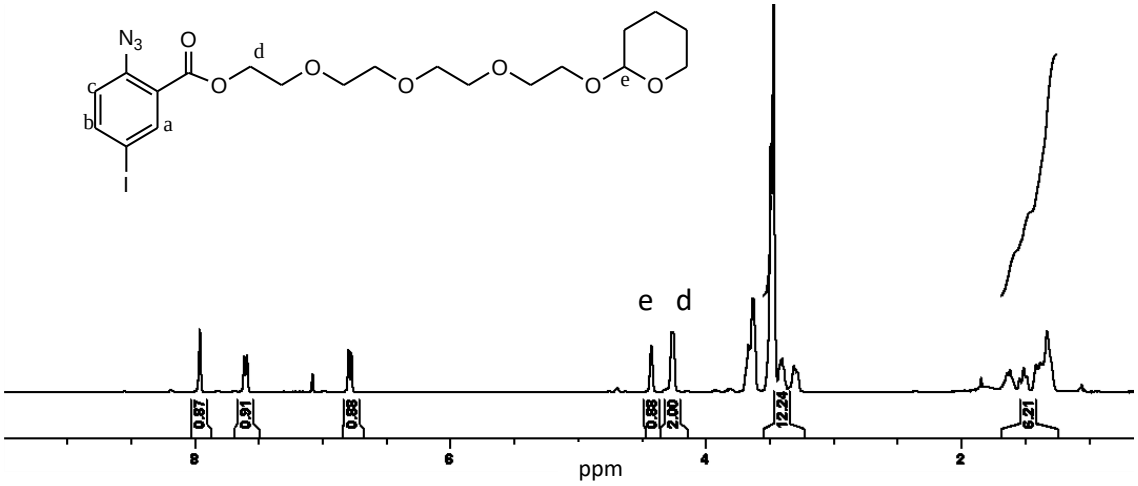

Figure A6: ^{1}H NMR spectrum of 2-{2-[2-(tetrahydro-2H-pyran-2-yloxy)ethoxy]ethoxy}-propyl 2-azido 5-iodobenzoate **95**.

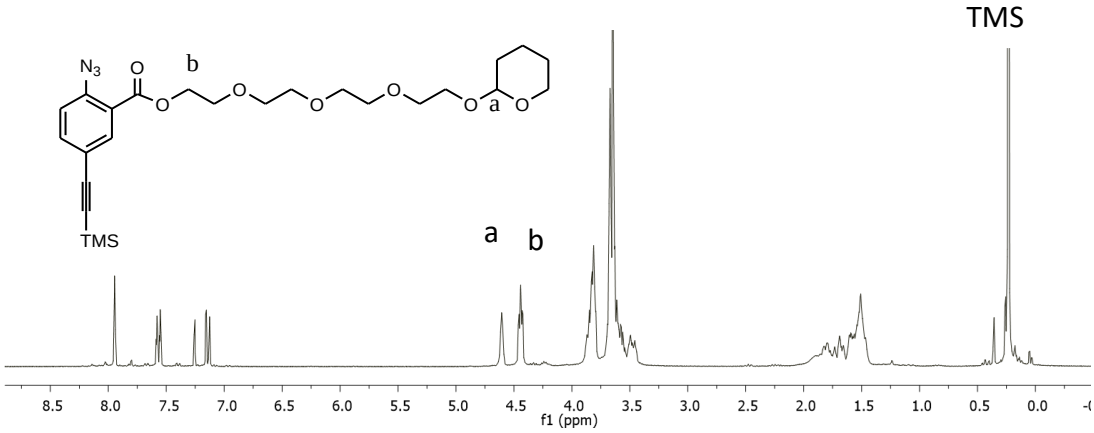

Figure A7: ^{1}H NMR spectrum of 2-{2-[2-(tetrahydro-2H-pyran-2-yloxy)ethoxy]ethoxy}ethoxypropyl-2-azido-5[2(trimethylsilyl)ethynyl]benzoate **96**.

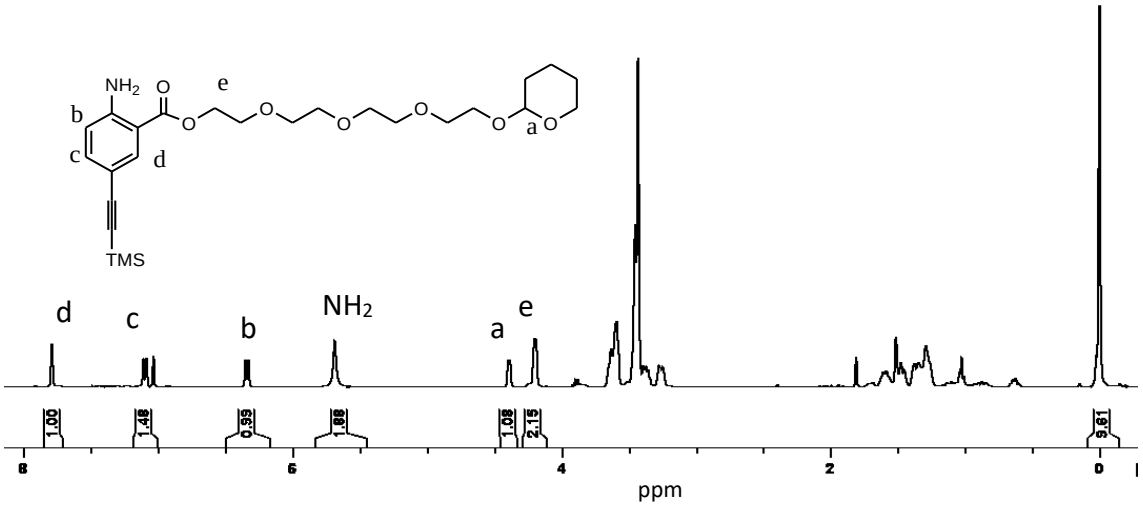

Figure A8: ^{1}H NMR spectrum of 2-{2-[2-(tetrahydro-2H-pyran-2-yloxy)ethoxy]ethoxy}ethoxypropyl-2-amino-5[2(trimethylsilyl)ethynyl]benzoate **97**.

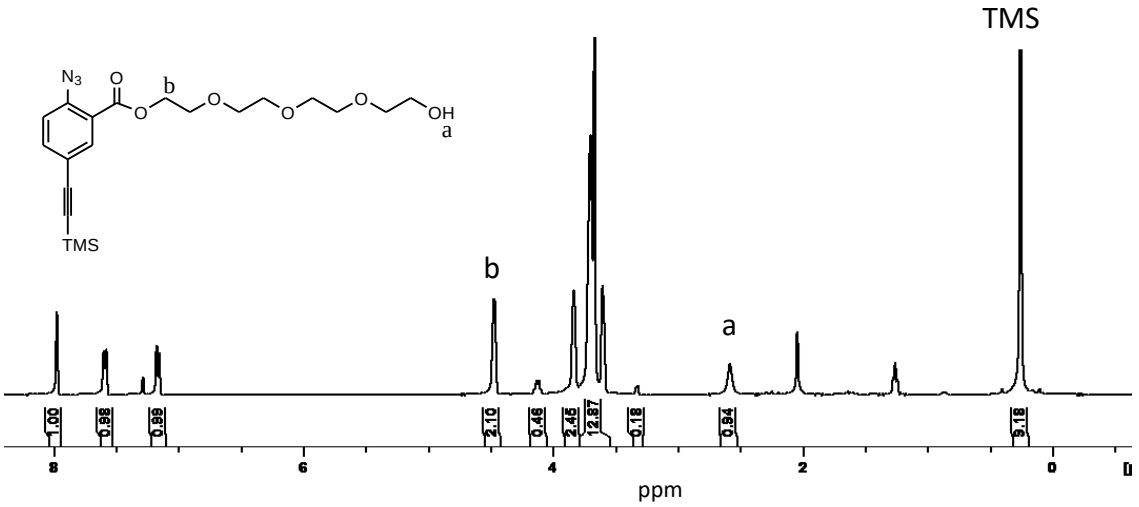

Figure A9: ^{1}H NMR spectrum of 2-{2-[2-(ethoxy)ethoxy]ethoxy}propyl2-azido-5-[2-(trimethylsilyl)-ethynyl]benzoate **98.**

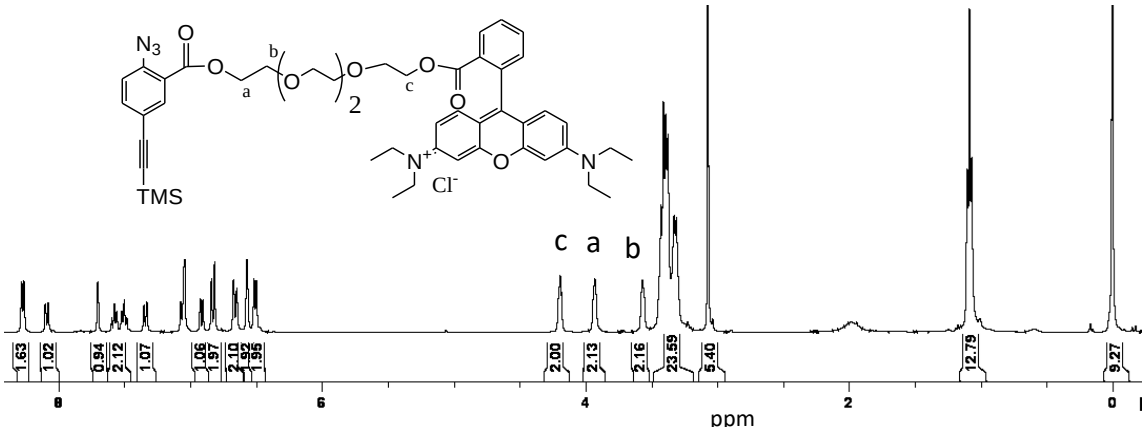

Figure A10: ^{1}H NMR spectrum of pigmented monomer precursor **103.**

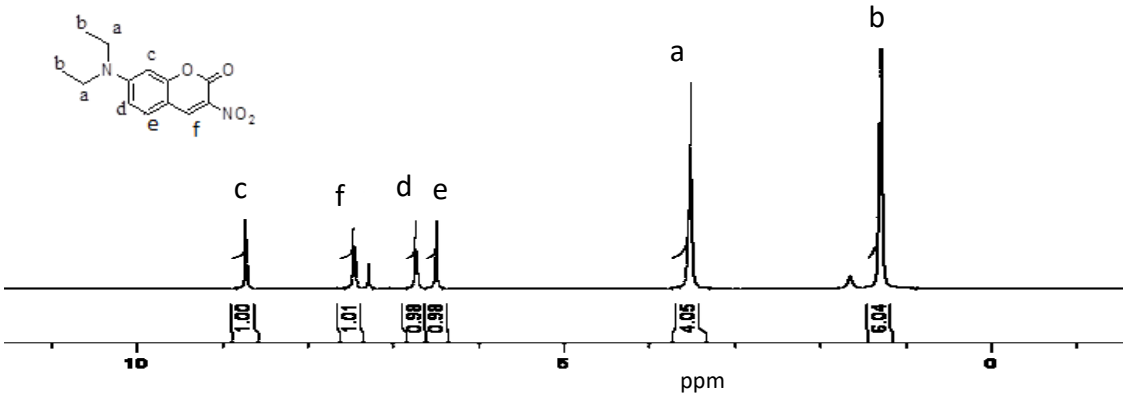

Figure A11: ^{1}H NMR spectrum of 3-nitro-7-diethylaminocoumarin **107**.

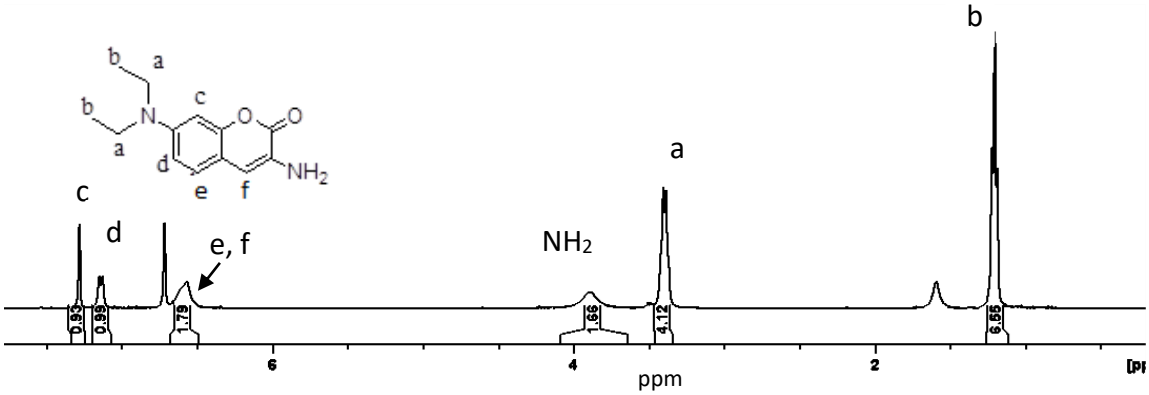

Figure A12: ^{1}H NMR spectrum of 3-amino-7-diethylaminocoumarin **108**.

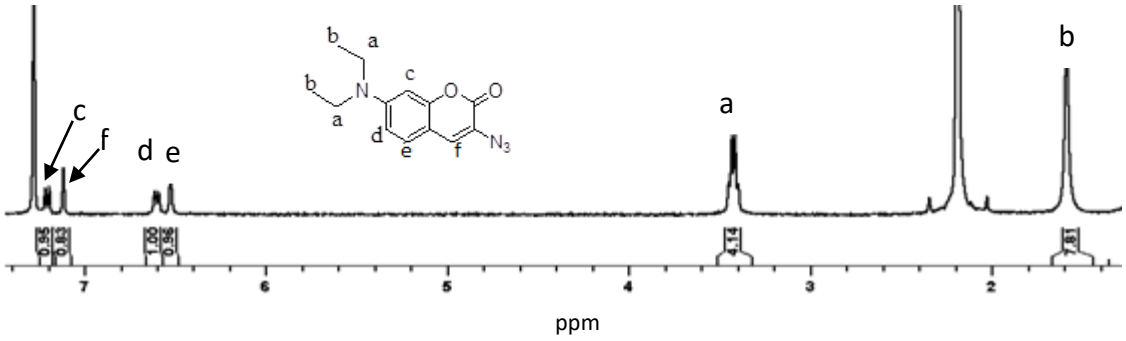

Figure A13: ^{1}H NMR spectrum of 3-azido-7-diethylaminocoumarin **109**.

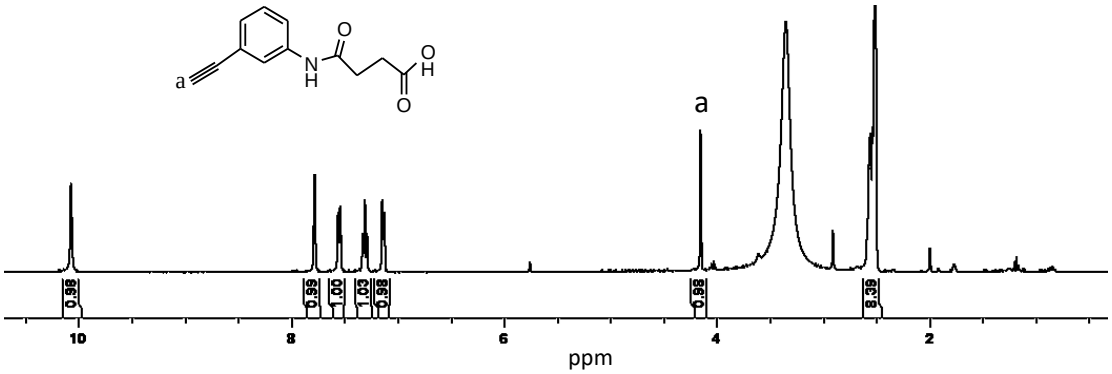

Figure A14: ^{1}H NMR spectrum of 3-(3-ethynylphenylcarbamoyl)propanoic acid **112**.

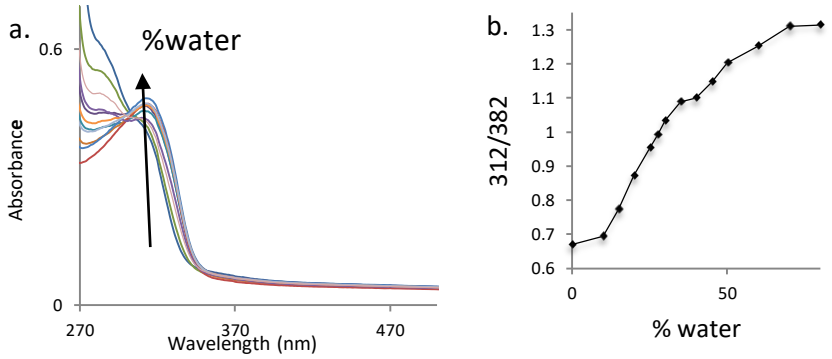

Figure A15: UV-Vis absorption curves of chiral (-) pPAT **3** [c] the corresponding job plot (d) for the 312/282 absorption ratio upon titration of 10 – 80% water into PAT/DMF solution at a concentration of 8.0×10^{-6} M at 25 °C.

a. b.

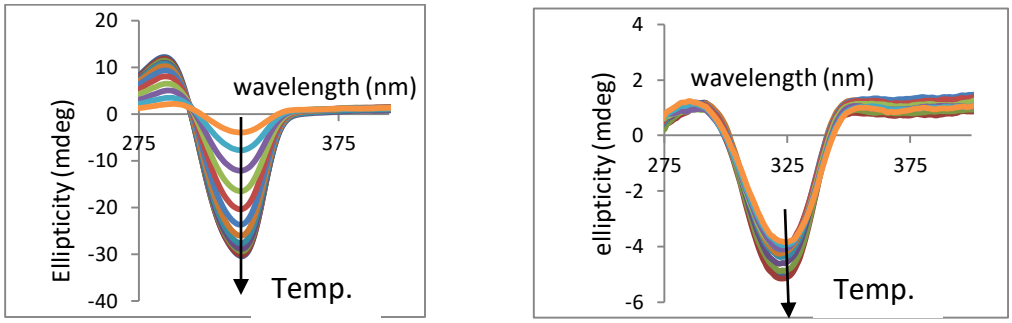

Figure A 16: The CD-based temperature denaturation of pPAT **5** (a) and co-pPAT **3** (b).

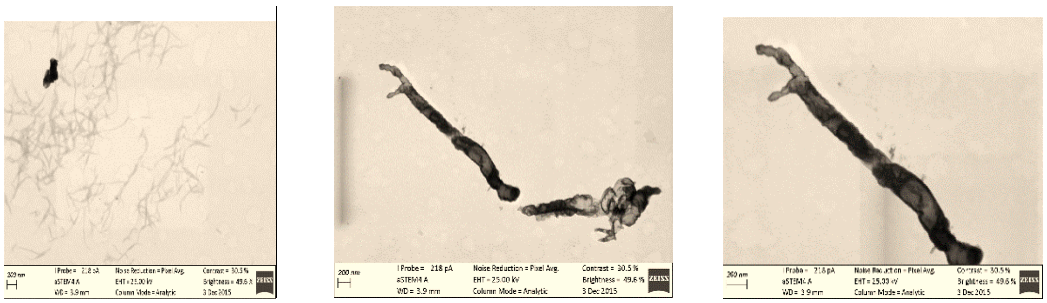

Figure A17: STEM image shows multiple wraps around the template.

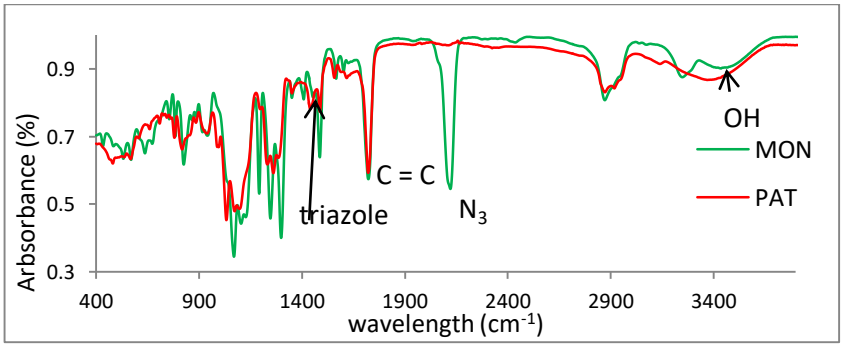

Figure **A18:** FT-IR overlay for the achiral pPAT **1** and its monomer **70**.

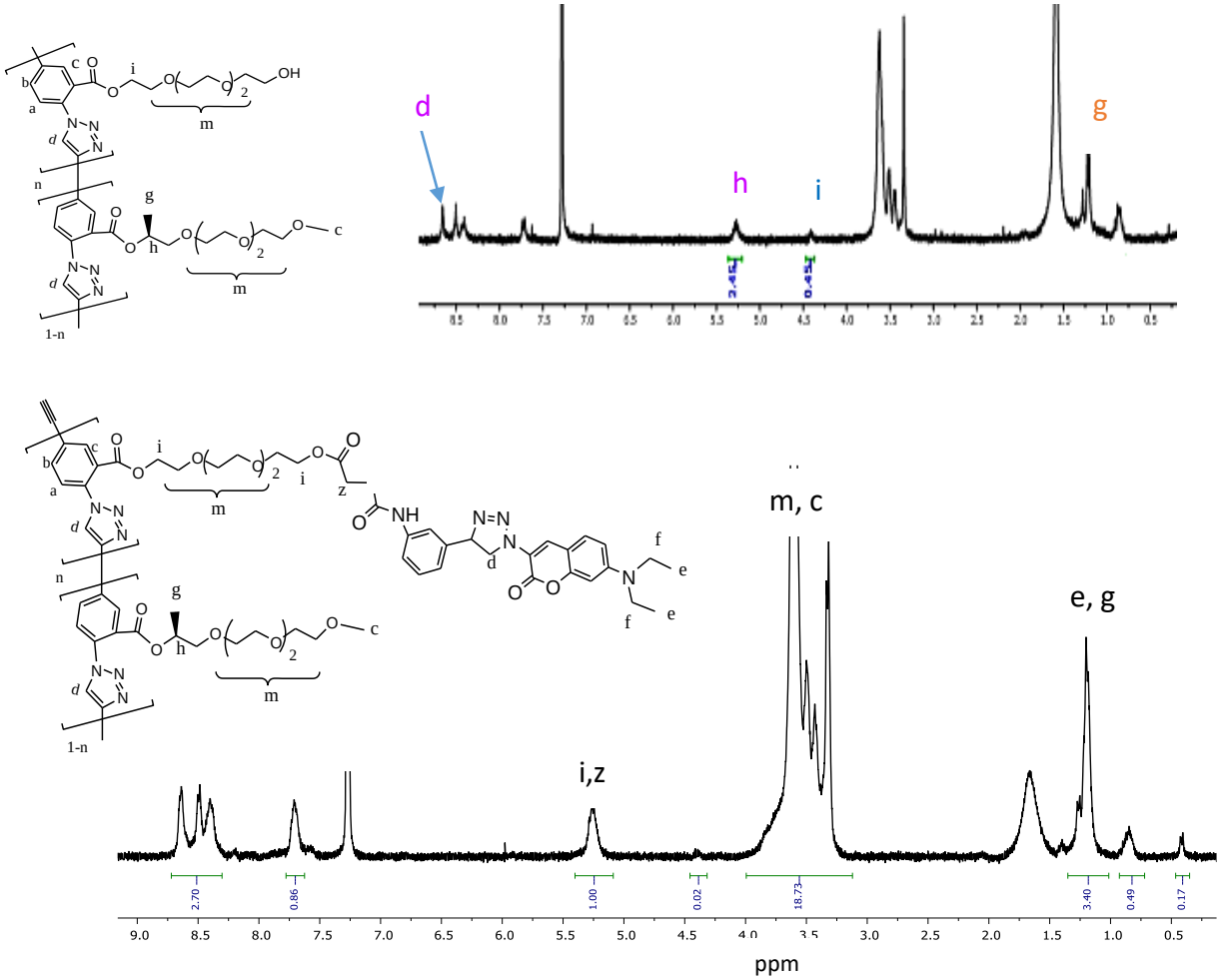

Figure A19: ^{1}H NMR spectrum for coumarin labelled pPAT **3** and corresponding pPAT **99** in $CDCl_3$

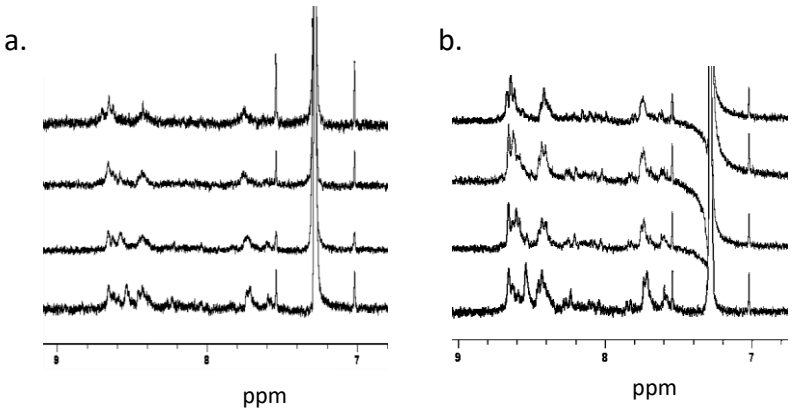

Figure A20: (a) Comparison of the ^{1}H NMR chemical shifts of the triazole proton of pPAT **2** upon titration of a) F^- and b) Cl^- ions

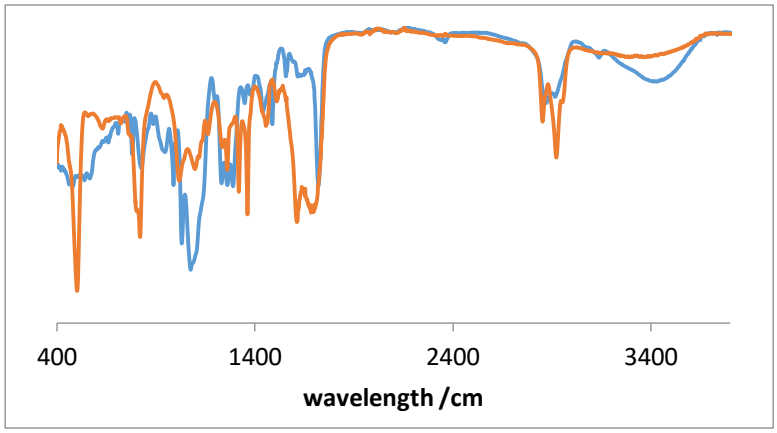

Figure A 21: FTIR overlay for the labelled pPAT **3** (blue) and pPAT **99** (pink)

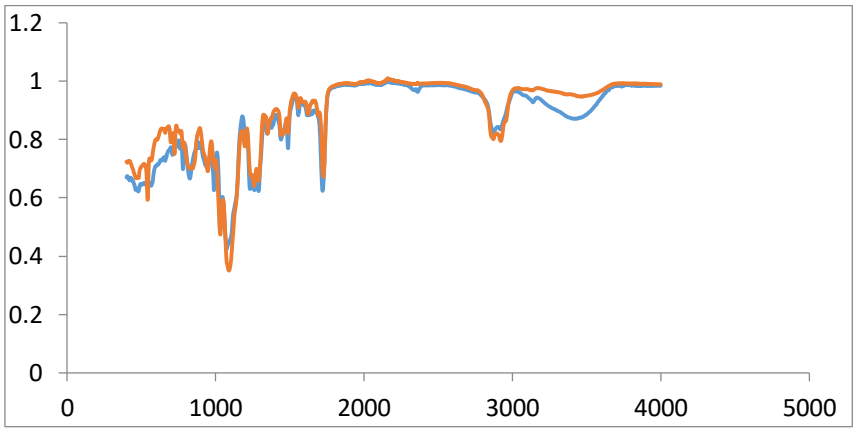

Figure A 22: FTIR overlay for the 18% (pink) and 1% (blue) chiral co-PATs

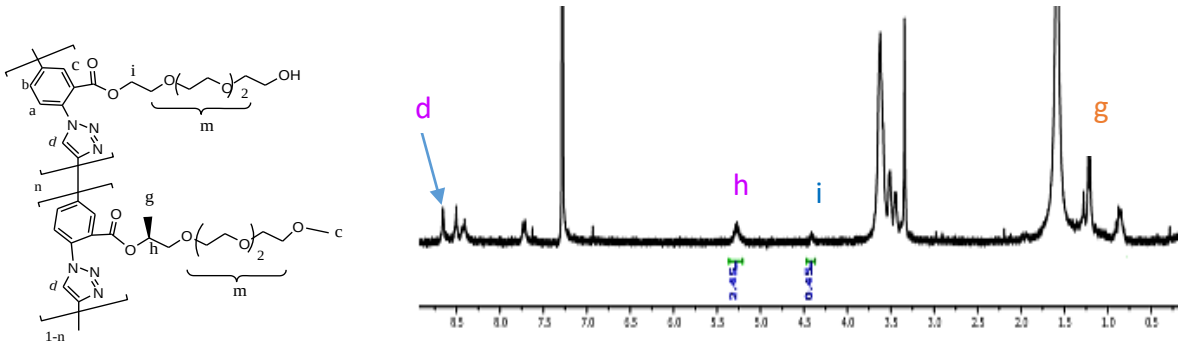

Figure A23: ^{1}H NMR spectrum of coumarin dye labeled pPAT.